YÜZÜNCÜ YIL ÜNİVERSİTESİ

Fen Bilimleri Enstitüsü Dergisi

YUZUNCU YIL UNIVERSITY

Journal of the Institute of Natural & Applied Sciences

www.dergipark.gov.tr

ISSN 1300 - 5413

Yıl / *Year* : 2021 Cilt / *Volume* : 26 Sayı / *Number* : 2

YÖNETİM YERİ VE YAZIŞMA ADRESİ (CORRESPONDENCE ADDRESS)

Van Yüzüncü Yıl Üniversitesi Rektörlüğü Fen Bilimleri Enstitüsü Zeve Yerleşkesi 65080
VAN

Telefon :0(432) 225 11 23

Belgegeçer (Faks): 0(432) 225 11 23

e-posta:dergifenbilimleri@yyu.edu.tr

Cilt (Volume): 26
Sayı (Number): 2
Web: https://dergipark.org.tr/tr/pub/yyufbed
Basıldığı Yer ve Tarih: VAN, 2020
ISSN:1300-5413

DERGİ BİLGİLERİ

Yüzüncü Yıl Üniversitesi Fen Bilimleri Enstitüsü Dergisi

ISSN 1300-5413 | **e-ISSN** 2667-467X | **Yayın Aralığı** Yılda 3 Sayı | **Başlangıç:** 1995

Yuzuncu Yil University Journal of the Institute of Natural & Applied Sciences

JINAS

İçindekiler / Contents

Araştırma Makaleleri / Research Articles

- Reaktör Yapı Materyallerinde Bulunan ^{45}Sc, ^{51}V, ^{52}Cr, ^{59}Co ve ^{63}Cu İzotoplarının (γ,n) Reaksiyon Tesir Kesitleri Hesaplamaları — 61-68
  Ömer Faruk ÖZDEMİR, Ali ARASOĞLU
- Comparison of Environment Noise Intensity Using Ios and Android Based Sound Measurement Applications and Commercial Sound Measurement Devices and Obtaining the Measurement Uncertainty — 69-79
  İsrafil ŞABİKOĞLU, Duygu AKBABA ŞABİKOĞLU
- Antimikrobiyal ve Antikanser Aktiviteye Sahip Cyclo(Trp-Trp) Dipeptidinin 3-Boyutlu Moleküler Yapısı — 80-87
  Sefa ÇELİK, Sevim AKYÜZ, Ayşen ERBÖLÜKBAŞ ÖZEL
- Modülüs Fonksiyon Yardımı ile Tanımlanan İnvaryant Yakınsak Dizi Uzaylarının Topolojik Özellikleri — 88-93
  Hasan KARA, Dinçer ATASOY
- A Bayesian Approach to Binary Logistic Regression Model with Application to OECD Data — 94-101
  Asuman YILMAZ, Eray ÇELİK
- Investigation of Some Physical Properties of CoAsS Crystal Under Pressure — 102-113
  Ferhat ARSLANBAŞ[1], Emel KİLİT DOĞAN

Yüzüncü Yıl Üniversitesi
Fen Bilimleri Enstitüsü Dergisi

http://dergipark.gov.tr/yyufbed

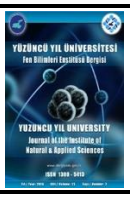

Araştırma Makalesi

Reaktör Yapı Materyallerinde Bulunan ^{45}Sc, ^{51}V, ^{52}Cr, ^{59}Co ve ^{63}Cu İzotoplarının (γ,n) Reaksiyon Tesir Kesitleri Hesaplamaları*

Ömer Faruk ÖZDEMİR*[1], Ali ARASOĞLU[2]

[1]Van Yüzüncü Yıl Üniversitesi, Fen Fakültesi, Fizik Bölümü, 65080, Van, Türkiye
[2]Van Yüzüncü Yıl Üniversitesi, Fen Fakültesi, Emekli Öğretim Üyesi, 65130, Van, Türkiye

Ömer Faruk ÖZDEMİR, ORCID No: 0000-0002-2389-1139, Ali ARASOĞLU, ORCID No: 0000-0001-7753-0016
*Sorumlu yazar e-posta: o.f.ozdemir@gmail.com

Makale Bilgileri

Geliş: 12.04.2021
Kabul: 11.05.2021
Yayınlanma Ağustos 2021
DOI: 10.53433/yyufbed.913870

Anahtar Kelimeler
Foto-nötron reaksiyonları,
Tesir kesiti,
Denge modelleri,
Denge öncesi modelleri

Öz: Bu çalışmada reaktör korunda veya zırhlama betonunda kullanılan yapı malzemelerin de bulunan ^{45}Sc, ^{51}V, ^{52}Cr, ^{59}Co ve ^{63}Cu izotoplarının, *10 - 50 MeV* enerji aralığında foto - nötron reaksiyonlarının tesir kesiti hesaplamaları yapıldı. Hesaplamalarda Weisskopf - Ewing Model için PCROSS, Hibrid Monte - Carlo Simülasyon Modeli için ALICE - 2011 ve Kaskad Eksiton Model için de CEM03.01 programları kullanıldı. Her model için yapılan tesir kesiti hesaplamaları birbirleriyle, EXFOR (Experimental Nuclear Reaction Data) veri tabanından alınan deneysel veriler ile ve literatürde yer alan JANIS (Java - based Nuclear Information Software) veri kütüphanesinden elde edilen değerlendirilmiş verilerle (JENDL/PD - 2004 ve TENDL - 2014) karşılaştırıldı.

(γ,n) Reaction Cross Section Calculations of ^{45}Sc, ^{51}V, ^{52}Cr, ^{59}Co and ^{63}Cu Isotopes in Reactor Building Materials

Article Info

Recieved: 12.04.2021
Accepted: 11.05.2021
Published August 2021
DOI: 10.53433/yyufbed.913870

Keywords
Photo-neutron reactions,
Cross section,
Equilibrium models,
Pre-equilibrium models

Abstract: In this study, the cross - section calculations of photo - neutron reactions of ^{45}Sc, ^{51}V, ^{52}Cr, ^{59}Co and ^{63}Cu isotopes which are used in building materials of reactor core or shielding concrete in the range of *10 - 50 MeV* were performed. PCROSS for the Weisskopf - Ewing Model, ALICE - 2011 for the Hybrid Monte - Carlo Simulation Model, and CEM03.01 for the Cascade Exciton Model were performed in the calculations. The findings obtained from cross - section calculations of each model were compared not only with each other, but also experimental and theratical data gattehred from EXFOR (Experimental Nuclear Reaction Data) database and JANIS (Java - based Nuclear Information Software) data library (JENDL / PD - 2004 and TENDL - 2014), respectively.

* Bu çalışma, Ömer Faruk ÖZDEMİR'in doktora tezinden üretilmiştir.

1. Giriş

Nükleer reaktörler için malzeme ve yakıt seçimi, fizik, kimya, malzeme bilimi ve mühendisliği, sistem analizi ve ekonomi dahil çok disiplinli bir yaklaşımı içerir. Uygun malzemeyi seçmek için, her bir malzemenin bakımı ve geri dönüşümü için kimyasal bileşimleri dikkate alınmalıdır. Ayrıca yapısal malzemelerin de yüksek radyasyona dayanıklı, yoğun nötron akısına karşı düşük aktivasyona sahip olması diğer zorunluluklardır (Simnad, 2003).

Nükleer reaktörlerde kullanılan yapısal malzemelerin gerçekleştirdikleri reaksiyonlar, reaktör ömrü ile reaktörün bakım ve onarım sürelerini etkiler (Clement, 2010). Yüksek radyasyona maruz kalan yapısal malzemenin transmutasyon sonucu radyoaktif izotoplara dönüşmesi istenmeyen bir sonuçtur. Bu nedenle söz konusu reaksiyonların türü ve reaksiyon tesir kesitlerinin öngörülebilir olması uygun malzeme seçimi için çok önemlidir (Simnad, 2003). Nükleer teknolojiyi verimli ve güvenli bir şekilde kullanmak için çok sayıda deneysel ve teorik veriye ihtiyaç duyulur. Deneysel verinin elde edilememesi veya deneysel araştırma yapılamaması durumunda teorik kesit hesaplamaları önemli bir rol üstlenir. Dolayısıyla tasarımda zırh geometrisi, kullanılan malzemenin bileşenleri ile yoğunlukları, elementlere ait tesir kesitleri ve termal özelliklerinin bilinmesi zorunludur (Shultis & Faw, 2012).

Tesir kesiti hesaplamaları için bileşik çekirdek modeli (Weisskopf & Ewing, 1940), denge öncesi bozunma için (eksiton model) (Griffin, 1966), denge öncesi reaksiyon modellerinin sentezi olarak kabul edilen hibrid model (Blann, 1971) ve yine denge öncesi parçacık yayınlama hesaplamaları için Kaskad - Eksiton Model (Gudima ve ark., 1983) önerilmiştir. Blann (1996) tarafından Monte Carlo simülasyon modeli kullanılarak yeni bir denge öncesi reaksiyon modeli sunulmuş ve Hibrid Monte - Carlo simülasyon modeli ile hesaplamalar için ALICE - 2011 bilgisayar programı yayınlanmıştır (Blann, 2011). Nükleer reaksiyon modelleri ile denge ve denge öncesi parçacık yayınlama ve foto nötron tesir kesiti hesaplamaları yapılmıştır (Uğur ve ark., 2013; Siddik, 2019; Özdoğan ve ark., 2020; Fynan ve ark., 2021).

Foto - nötron reaksiyonlarının, fisyon, füzyon ve hibrit reaktör korundaki nötron ekonomisine katkısı oldukça önemlidir. Ayrıca reaktör korundan yayınlanan yüksek enerjili gama ışınlarının menzil ve giriciliğinin büyük olması, reaktör zırhlamasında foto - nötron reaksiyonlarının önemini artırmaktadır. Radyasyonun personel güvenliğini tehdit etmesi ve elektronik ekipmanlarda tahribata sebep olması nedeniyle reaktörlerde zırhlama büyük öneme sahiptir (Gupta, 2001; Pearton ve ark., 2013). Bu nedenle yapısal malzemelerin seçiminde kullanılacağı yer ve oluşabilecek ikincil radyasyonlar göz önüne alınarak bir planlama yapılması zorunluluktur seçilen malzeme içindeki izotopların nükleer reaksiyon tesir kesitlerinin belirlenmesi ve öngörülebilmesi oldukça önemlidir.

Foto - nükleer reaksiyon tesir kesitleri için uygulamada en önemli uyarılma enerji aralığı, birçok laboratuvar ve hastanede bulunan küçük doğrusal hızlandırıcılar ile elde edilebilen *25 MeV*'e kadardır. Ayrıca, *30 MeV*'nin altındaki düşük enerjilerde, dev dipol rezonansı (GDR) baskın uyarma mekanizmasıdır. *50 MeV* enerjiye kadar olan foto nükleer veriler, geliştirilmekte olan yeni tıbbi hızlandırıcı teknolojileri için de yararlıdır (IAEA, 2000).

Nükleer reaktörlerde yapı malzemesi olarak yaygın bir kullanım alanına sahip olan betonun hidrojen içermesi *(%0.54-2.22*) nötron ve gama zırhlama için de uygun bir malzeme olmasını sağlar (Shultis, 2010). Reaktörlerde zırhlama amacıyla kullanılan beton içerisinde yer alan elementlerden bazılarının foto - nötron reaksiyonları ile yayınlanan ikincil radyasyon ve oluşan kararlı çekirdekler aşağıda verildiği gibidir.

$$
\begin{aligned}
^{45}Sc(\gamma,n)^{44}Sc \quad & (3.97\ saat) \xrightarrow{ec\ \beta^+} {}^{44}Ca \\
^{51}V(\gamma,n)^{50}V \quad & (2.65\ yıl) \xrightarrow{ec\ \beta^+} {}^{50}Ti \\
^{52}Cr(\gamma,n)^{51}Cr \quad & (27.7\ g\ddot{u}n) \xrightarrow{ec} {}^{51}V \\
^{59}Co(\gamma,n)^{58}Co \quad & (70.86\ g\ddot{u}n) \xrightarrow{ec\ \beta^+} {}^{58}Fe \\
^{63}Cu(\gamma,n)^{62}Cu \quad & (9.67\ dak.) \xrightarrow{ec\ \beta^+} {}^{62}Ni
\end{aligned}
\tag{1}
$$

^{45}Sc, ^{51}V, ^{52}Cr, ^{59}Co ve ^{63}Cu izotopları için verilen reaksiyonlarda görülen son ürünlerin kararlı izotoplar olmaları bir avantaj sağlamakta ancak oluşan ikincil parçacıklar (β^+) ortam içerisindeki elektronlarla annihilasyon gerçekleştirerek yeniden düşük enerjili bir gama yayınlanmasına neden olurlar. Yapısal malzeme içinde oluşan ikincil gamalar şayet zırhlama malzemesinin yüzeyinden yayınlanırsa personel ve ekipman güvenliği için dezavantaj oluşturabilir. Bu nedenle yapısal malzemelerin seçiminde kullanılacağı yer ve oluşabilecek ikincil radyasyonlar göz önüne alınarak bir planlama yapılması zorunluluktur. Bu amaçla malzeme içindeki seçilen izotopların nükleer reaksiyon tesir kesitlerinin belirlenmesi ve öngörülebilmesi oldukça önemlidir.

Bu çalışmada reaktör korunda veya zırhlama betonunda kullanılan yapı materyallerinde bulunan ^{45}Sc, ^{51}V, ^{52}Cr, ^{59}Co ve ^{63}Cu izotopların, *10-50 MeV* aralığında foto - nötron reaksiyonlarının tesir kesiti hesaplamaları yapıldı. Hesaplamalarda Weisskopf - Ewing Model için PCROSS, Hibrid Monte - Carlo Simülasyon Modeli için ALICE - 2011 ve Kaskad Eksiton Model için de CEM03.01 programları kullanıldı. Her model için yapılan tesir kesiti hesaplamaları birbirleriyle, EXFOR (Experimental Nuclear Reaction Data) veri tabanından alınan deneysel veriler ile ve literatürde yer alan JANIS (Java - based Nuclear Information Software) veri kütüphanesinden elde edilen değerlendirilmiş verilerle (JENDL/PD - 2004 ve TENDL - 2014) karşılaştırıldı.

2. Materyal ve Yöntem

Sıvı damlası modeli benzetiminin kullanıldığı Bileşik Çekirdek Modeli nükleer reaksiyonların iki bağımsız aşamada gerçekleştiğini varsayar. Bu aşamalardan ilki; çekirdeğin mermi tanecik ile istatistiksel dengeye ulaştığı bileşik çekirdeğin oluşumu, ikincisi ise; bileşik çekirdeğin bozunumudur.

Weisskopf - Ewing (WE) modele göre bileşik çekirdek reaksiyon tesir kesiti;

$$\sigma(a,b) = \sigma_a(\varepsilon)\,\eta_b(E) \tag{2}$$

şeklinde verilir (Weisskopf & Ewing, 1940). Burada $\sigma_a(\varepsilon)$; ε enerjili a parçacıkları ile bombardıman edilen hedef çekirdeğin bileşik çekirdek oluşturma tesir kesitidir. Kısmi parçacık yayınlama olasılığı η_b ise;

$$\eta_b = \frac{\Gamma_b}{\sum_{b'}\Gamma_{b'}} \tag{3}$$

olarak tanımlanır. Burada Γ_b bileşik çekirdeğin birim zamanda b parçacığı yayınlama olasılığıdır ve *E* uyarılma enerjisinin ölçülmesindeki belirsizliğin bir ölçüsüdür.

$$\Gamma_b = \frac{2s_b+1}{\pi^2\hbar^2}\mu_b\int d\varepsilon\,\sigma_b^{inv}(\varepsilon)\,\varepsilon\,\frac{\omega_1(U)}{\omega_1(E)} \tag{4}$$

Burada σ_b^{inv}, *U*, μ_b ve s_b sırasıyla ters reaksiyon tesir kesiti, ürün çekirdeğin uyarılmış durum enerjisi, indirgenmiş kütle ve spindir. *E* uyarılma enerjisine sahip bileşik çekirdeğin yoğunluk seviyesi

$$\omega_1(E) = \frac{1}{\sqrt{48}}\,\frac{\exp\left[2\sqrt{\alpha(E-D)}\right]}{E-D} \tag{5}$$

şeklinde verilir ve D çiftlenim enerjisidir. α, *g*, tek parçacık seviye yoğunluğu olmak üzere $\propto = 6g/\pi^2$ şeklinde verilir (Capote ve ark., 1991).

Hesaplamalarda kullanılan ikinci model, Kaskad Eksiton Modelde (CEM) nükleer reaksiyonların i. Intranükleer Kaskad (INC), ii. Denge öncesi (Pre-Equilibrium) ve iii. Denge (Bileşik Çekirdek) olmak üzere üç aşamada gerçekleştiği varsayılır:

İlk aşama olan INC Model; çekirdeğe giren mermi parçacığın enerjisi çekirdek tarafından soğurulana kadar çarpışmalarla saparak ikincil parçacıklar oluşturması sürecidir ve Monte Carlo hesaplama yöntemine dayanan bir istatistik modeldir. INC Model'e göre; enerjinin nükleonlar arasında paylaşımı ile çekirdek, istatistik anlamda dengeye ulaşır ve WE Modele benzer şekilde buharlaşma ile parçacık yayınlar (Mashnik ve ark., 2005).

CEM03.01 programında INC model hesaplamaları için Dubna kaskad modelinin standart (zamandan bağımsız) versiyonunu kullanılır ve tüm kaskad hesaplamaları üç-boyutlu olarak ele alınır. *10~40 MeV* aralığındaki enerjilerde foton tek bir nükleonla değil rezonans bölgesiyle bütün olarak etkileştiğinden INC model kullanılamaz (Mashnik ve ark., 2005). Gelme enerjisinin, GDR bölgesinin üzerinde olduğu reaksiyonlar için ortaya konulan, Dubna INC modelin fotonükleer versiyonu kullanılır. CEM, INC ile Denge arasında denge-öncesi parçacık yayınlanmasını öngörür. Eksiton durumu belirlenen çekirdek, denge durumuna ulaşana kadar, Eksiton Model'de verildiği gibi her adımda parçacık yayınlayabilir (Gudima ve ark., 1983).

CEM'de tesir kesiti hesaplamalarına her üç aşamanın da katkısı dahil edilir ve parçacık spektrumu

$$\sigma(p)dp = \sigma_{in}\left[N^{cas}(p) + N^{prq}(p) + N^{eq}(p)\right]dp \tag{6}$$

denklemi ile elde edilir. Burada p; momentum ve σ_{in}; inelastik tesir kesitidir. σ_{in} cascade model içinde hesaplanır (Mashnik ve ark., 2005).

Hibrid Monte - Carlo Simulasyon (HMS) modeli; denge - öncesi Hibrid model temel alınarak hazırlanmış, kinematik açıdan doğrulanan iki ya da üç eksiton durumlu, her bir çekirdeğin sınırsız sayıda denge öncesi parçacık yayınlama olasılığını göz önüne alan bir modeldir (Blann, 1996). Bu modelde, Monte Carlo seçimi için öncelikle, uyarılmış nükleonun çarpışacağı nükleon türü belirlenir. Saçılmaya uğrayan nükleonların ve boşluğun, Fermi seviyesi üzerindeki enerjileri belirlenerek parçacıkların saçılma ya da yayınlanma durumu seçilir. Bu süreç; çekirdek, denge durumuna yakın enerjilere ulaşana kadar devam eder.

HMS model de, ε_L kanal enerjili bir nükleonun sürekliliğe (continuum) yayınlanma olasılığı;

$$P_\nu(\varepsilon_L) = \frac{\lambda_c(\varepsilon_L)}{\lambda_c(\varepsilon_L) + \lambda_+\left[\varepsilon_L + BE(Z,A,\nu)\right]} \tag{7}$$

şeklinde verilir. Burada, $\lambda_c(\varepsilon_L)$; ε_L enerjili nükleonların sürekliliğe geçiş oranı, λ_+; iç geçiş oranıdır. Rölativistik kanal enerjisi ε_L;

$$\varepsilon_L = \varepsilon - BE(Z', A', \nu) \tag{8}$$

olarak tanımlanır. ε; Fermi enerjisi üzerindeki nükleon enerjisi, ν; proton ya da nötron, Z' ve A'; sırasıyla kaskad sürecindeki çekirdeğin atom ve kütle numaralarıdır (Blann, 2011).

3. Bulgular

Bu çalışmada $^{45}Sc(\gamma,n)^{44}Sc$, $^{51}V(\gamma,n)^{50}V$, $^{52}Cr(\gamma,n)^{51}Cr$, $^{59}Co(\gamma,n)^{58}Co$ ve $^{63}Cu(\gamma,n)^{62}Cu$ reaksiyonları için *10 - 50 MeV* aralığında foto - nötron reaksiyon tesir kesitleri hesaplamaları WE Model için PCROSS, HMS model için ALICE - 2011 ve Kaskad Eksiton Modeli için de CEM03.01 programları kullanılarak yapıldı. Her model için yapılan tesir kesiti hesaplamaları birbirleri ve EXFOR (Experimental Nuclear Reaction Data) veri tabanından alınan deneysel veriler ile karşılaştırıldı. Deneysel verilerin sınırlı olması nedeniyle yapılan karşılaştırmalarda; JANIS (Java - based Nuclear Information Software) üzerinden alınan ve literatürde yer alan JENDL - 4.0 (Japanese Evaluated Nuclear Data Library), TENDL - 2014 (TALYS - based Evaluated Nuclear Data Library) ve JEFF - 3.2 (Joint Evaluated Fission and Fusion File) değerlendirilmiş veri kütüphanelerinden yararlanılarak Şekil 1, 2, 3, 4 ve 5 teki grafikler çizildi.

$^{45}Sc(\gamma,n)^{44}Sc$ reaksiyonu tesir kesiti hesaplamalarından (Şekil ; WE model sonuçları *12 - 28 MeV* aralığında deneysel verilerle uyumludur. *28 MeV*'den itibaren diğer model sonuçlarından ve değerlendirilmiş verilerden daha büyük değerli ancak benzer yapıdadır. HMS model ve CEM hesaplamaları, deneysel *ve* TENDL - 2014 verileri iyi uyum içerisindedir.

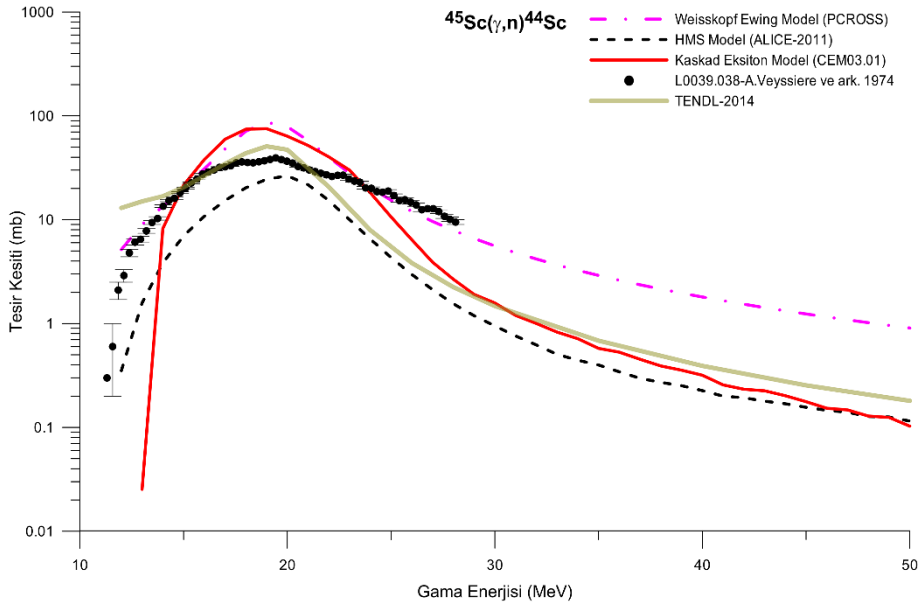

Şekil 1. $^{45}Sc(\gamma,n)^{44}Sc$ reaksiyonunun hesaplanan tesir kesitlerinin deneysel (EXFOR) ve değerlendirilmiş verilerle (TENDL - 2014) karşılaştırılması.

$^{51}V(\gamma,n)^{50}V$ reaksiyonu tesir kesiti hesaplamalarından (Şekil ; HMS model sonuçları *12-27 MeV* aralığında deneysel verilerle çok iyi uyumludur. Tüm enerji aralığında diğer model sonuçlarından daha düşük değerli ancak CEM hesaplamaları ile benzer yapıdadır. WE model ve CEM hesaplamaları, deneysel veriler ile iyi uyum içerisindedir. $^{51}V(\gamma,n)^{50}V$ reaksiyonu için JANIS veri tabanında değerlendirilmiş veri bulunmamaktadır.

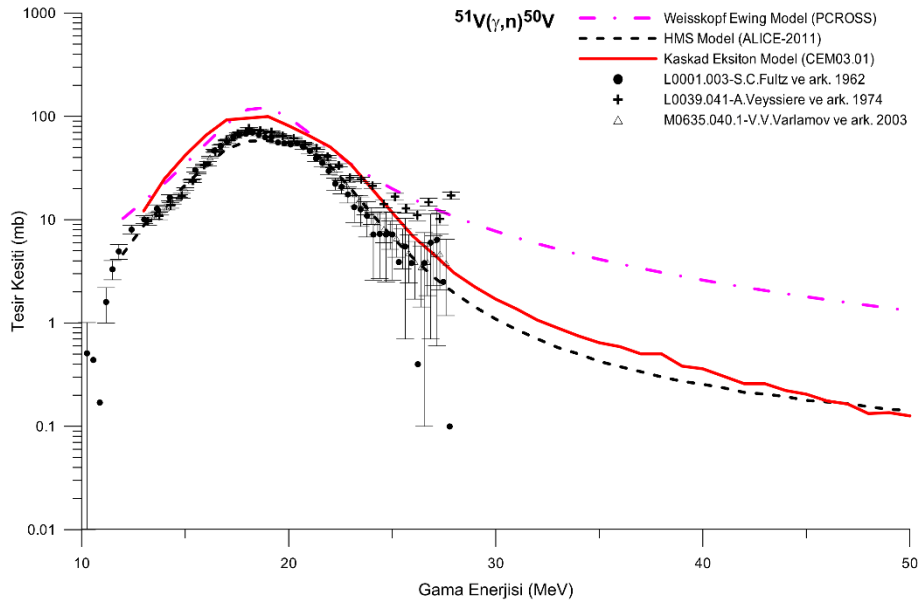

Şekil 2. $^{51}V(\gamma,n)^{50}V$ reaksiyonunun hesaplanan tesir kesitlerinin deneysel (EXFOR) ve değerlendirilmiş verilerle (JENDL/PD-2004, TENDL-2014) karşılaştırılması.

$^{52}Cr(\gamma,n)^{51}Cr$ reaksiyonu tesir kesiti hesaplamalarından (Şekil ; WE model sonuçları *18 - 25 MeV* aralığında deneysel verilerle çok iyi uyumludur. *25 MeV*'den itibaren diğer model sonuçlarından daha büyük değerlidir. HMS model ve CEM hesaplamaları, deneysel verilerle iyi uyum içerisindedir. $^{52}Cr(\gamma,n)^{51}Cr$ reaksiyonu için JANIS veri tabanında değerlendirilmiş veri bulunmamaktadır.

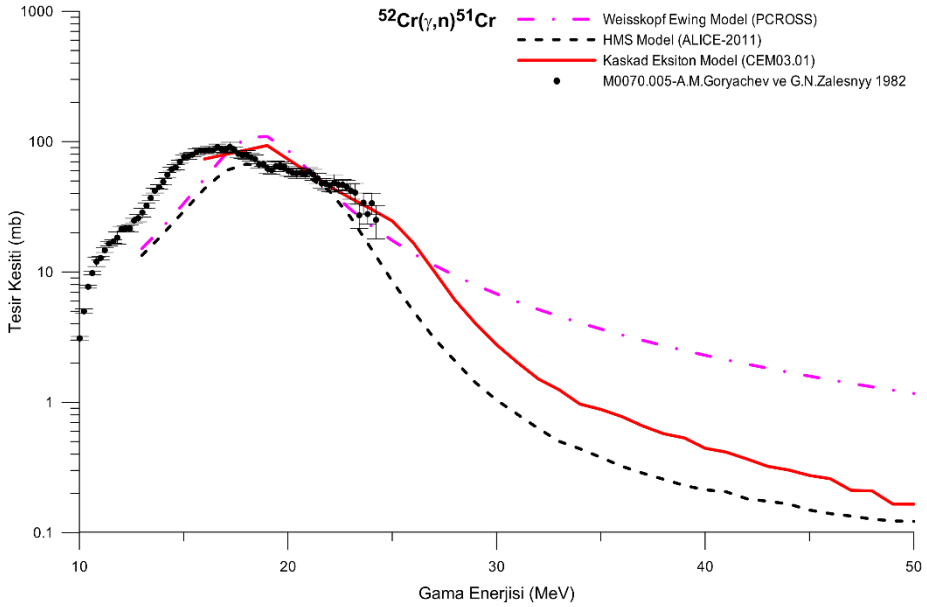

Şekil 3. $^{52}Cr(\gamma,n)^{51}Cr$ reaksiyonunun hesaplanan tesir kesitlerinin deneysel (EXFOR) verilerle karşılaştırılması.

$^{59}Co(\gamma,n)^{58}Co$ reaksiyonu tesir kesiti hesaplamalarından (Şekil ; WE model sonuçları *10 - 30 MeV* aralığında deneysel verilerle çok iyi uyumludur. *30 MeV*'den itibaren diğer model sonuçlarından ve değerlendirilmiş verilerden daha büyük değerli ancak benzer yapıdadır. HMS model ve CEM hesaplamaları, deneysel ve JENDL/PD - 2004 ile TENDL - 2014 verileri çok iyi uyum içerisindedir.

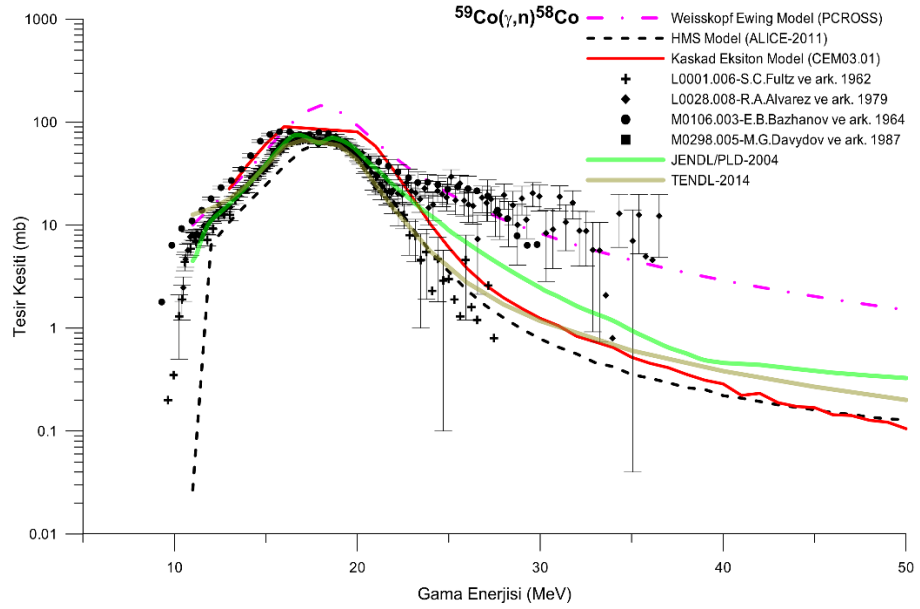

Şekil 4. $^{59}Co(\gamma,n)^{58}Co$ reaksiyonunun hesaplanan tesir kesitlerinin deneysel (EXFOR) ve değerlendirilmiş verilerle (JENDL/PD - 2004, TENDL - 2014) karşılaştırılması.

$^{63}Cu(\gamma,n)^{62}Cu$ reaksiyonu tesir kesiti hesaplamalarından (Şekil ; WE model sonuçları *12 - 22 MeV* aralığında deneysel verilerle çok iyi uyumludur. *22 MeV*'den itibaren diğer model sonuçlarından

ve değerlendirilmiş verilerden daha büyük ancak benzer yapıdadır. HMS model ve CEM hesaplamaları, deneysel *ve* JENDL/PD - 2004 ile TENDL - 2014 verileri çok iyi uyum içerisindedir.

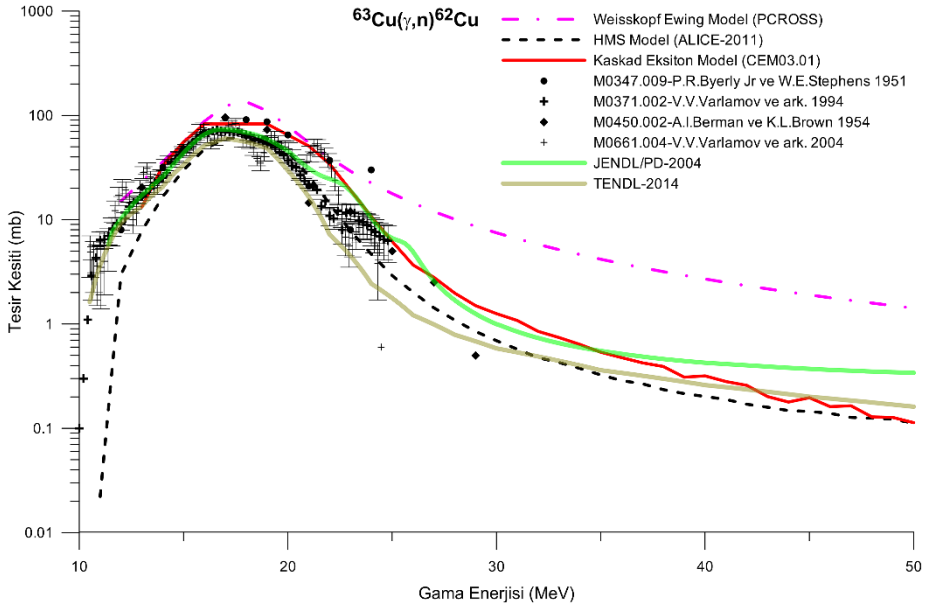

Şekil 5. $^{63}Cu(\gamma,n)^{62}Cu$ reaksiyonunun hesaplanan tesir kesitlerinin deneysel (EXFOR) ve değerlendirilmiş verilerle (JENDL/PD - 2004, TENDL - 2014) karşılaştırılması.

4. Tartışma ve Sonuç

Bu çalışmada nükleer reaktör yapı materyallerinde bulunan ^{45}Sc, ^{51}V, ^{52}Cr, ^{59}Co ve ^{63}Cu izotoplarının, *10 - 50 MeV* aralığında foto - nötron reaksiyon tesir kesiti hesaplamaları yapıldı.

Denge ve denge öncesi reaksiyon modellerinin kullanıldığı hesaplamalar, Weiskopf-Ewing Model için PCROSS, Hibrid Monte Carlo Simulasyon Modeli için Alice-2011 ve Kaskad Eksiton Model için de CEM03.01 bilgisayar programları ile yapıldı. Elde edilen sonuçlar birbirleri ve literatürde yer alan deneysel ve değerlendirilmiş verilerle karşılaştırıldı.

Sonuçlar ayrıntılı olarak incelendiğinde WE model sonuçlarının *10 - 28 MeV* enerji aralığında deneysel ve değerlendirilmiş verilerle uyumlu ancak yüksek enerji bölgesinde diğer model sonuçlarından ve değerlendirilmiş verilerden daha büyük sonuçlar verdiği görülür. ^{59}Co hesaplamalarında ise WE model yüksek enerji bölgesinde değerlendirilmiş verilerden daha başarılı sonuçlar vermekte ve deneysel verilerle çok iyi uyum göstermektedir.

HMS ve CEM ^{45}Sc hesaplamaları haricinde deneysel verilerle iyi uyum göstermekte, yüksek enerji bölgesinde de değerlendirilmiş verilerle uyumunu sürdürmektedir.

Elde edilen bulgular, düşük enerji bölgesinde her üç modelinde literatürde yer alan verilerle uyumlu olduğunu ve başarılı hesaplamalar yaptığını gösterir. Yüksek enerji bölgesinde ise HMS ve CEM model değerlendirilmiş verilerle uyumludur ve herhangi bir parametre düzeltmesine gerek olmadan kullanılabilecekleri şeklinde yorumlanabilir.

Teşekkür

Bu çalışma YYÜ Bilimsel Araştırma Projeleri Başkanlığı tarafından 2013-FBE-D005 No'lu proje olarak desteklenmiştir.

Kaynakça

Blann, M. (1971). Hybrid model for pre-equilibrium decay in nuclear reactions. *Physical Review Letters*, 27(6), 337–340. doi:10.1103/PhysRevLett.27.337

Blann, M. (1996). New precompound decay model. *Physical Review C - Nuclear Physics*, 54(3), 1341–

1349. doi:10.1103/PhysRevC.54.1341

Blann, M. (2011). Particle Spectra from HMS Precompound Nucleus Decay (ALICE2011). *Package ID USCD1238*, *5*.

Capote, R., Osorio, V., Lopez, R., Herrera, E., & Piris, M. *(1991). Analysis of Experimental Data on Neutron-Induced Reactions and Development of Code PCROSS for The Calculation of Differential Pre-equilibrium Emission Spectra With Modelling of Level Density Function*.

Clement Lemaignan (2010). Nuclear Materials and Irradiation Effects. Dan Gabriel Cacuci (Ed.), *Handbook of Nuclear Engineering* (545-631). Boston, MA, USA: Springer. doi:10.1007/978-0-387-98149-9

Fynan, D. A., Seo, Y., Kim, G., Barros, S., & Kim, M. J. (2021). Photoneutron production in heavy water reactor fuel lattice from accelerator-driven bremsstrahlung. *Annals of Nuclear Energy*, *155*, 108141. doi:10.1016/j.anucene.2021.108141

Griffin, J. J. (1966). Statistical model of intermediate structure. *Physical Review Letters*, *17*(9), 478–481.doi:10.1103/PhysRevLett.17.478

Gudima, K. K., Mashnik, S. G., & Toneev, V. D. (1983). Cascade-exciton model of nuclear reactions. *Nuclear Physics, Section A*, *401*(2), 329–361. doi:10.1016/0375-9474(83)90532-8

Gupta, C. K. (2001). Nuclear Reactor Materials. In K.H. J. Buschow, R. W. Cahn, M. C. Flemings, B. Ilschner, E. J. Kramer, S. Mahajan, P. Veyssière (Eds.), *Encyclopedia of Materials: Science and Technology* (pp. 6339–6349). Pergamon. doi:10.1016/B0-08-043152-6/01123-2

IAEA. (2000). *Handbook on Photonuclear Data for Applications Cross-sections and Spectra*. *7*, 284. http://www-pub.iaea.org/books/IAEABooks/6043/Handbook-on-Photonuclear-Data-for-Applications-Cross-sections-and-SpectraMashnik, S. G., Gudima, K. K., Sierk, A. J., Baznat, M. I., & Mokhov, N. V. (2005). CEM03. 01 user manual. *LANL Report LA UR*, *5*, 7321.

NEA (2015). JANIS 4.0 Java-based Nuclear Data Information System. https://www.oecd-nea.org/janis/. Erişim tarihi: 25.03.2021.

Özdoğan, H., Şekerci, M., & Kaplan, A. (2020). An Investigation on the Effects of Some Theoretical Models in the Cross-Section Calculations of ^{50,52,53,54}Cr(alpha,x) Reactions. *Physics of Atomic Nuclei*, *83*(6), 820–827. doi:10.1134/s1063778820660060

Pearton, S. J., Deist, R., Ren, F., Liu, L., Polyakov, A. Y., & Kim, J. (2013). Review of radiation damage in GaN-based materials and devices. *Journal of Vacuum Science & Technology A: Vacuum, Surfaces, and Films*, *31*(5), 050801. doi:10.1116/1.4799504

Shultis, J. K., & Faw, R. E. (2010). Radiation Shielding and Radiological Protection, v.2. In D. G. Cacuci (Eds.), *Handbook of Nuclear Enginering* (pp. 1313-1448). Boston, MA,USA: Springer. doi:10.1007/978-0-387-98149-9_11.

Shultis, J. K., & Faw, R. E. (2012). Radiation Shielding. In R. A. Meyers (Eds.), *Encyclopedia of Sustainability Science and Technology* (pp. 8536-8559). Newyork, USA: Springer-Verlag New York. doi:10.1007/978-1-4419-0851-3_25

Siddik, T. (2019). Theoretical cross-sectional calculation of some structural fusion material on (n, α)-induced reactions. *Indian Journal of Physics*, *93*(7), 921–925. doi:10.1007/s12648-018-1349-3

Simnad, M. T. (2003). Nuclear Reactor Materials and Fuels. In R. A. Meyers (Eds.), *Encyclopedia of Physical Science and Technology (Third Edition)* (pp. 775–815). USA: Academic Press. doi:10.1016/b0-12-227410-5/00498-1

Uğur, F. A., Tel, E., & Gökçe, A. A. (2013). A study on 19F(n,α) reaction cross section. *Journal of Fusion Energy*, *32*(3), 414–418. doi:10.1007/s10894-012-9587-4

Weisskopf, V. F., & Ewing, D. H. (1940). On the yield of nuclear reactions with heavy elements. *Physical Review*, *57*(6), 472–485. doi:10.1103/PhysRev.57.472

Yüzüncü Yıl Üniversitesi
Fen Bilimleri Enstitüsü Dergisi

http://dergipark.gov.tr/yyufbed

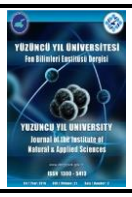

Research Article

Comparison of Environment Noise Intensity Using Ios and Android Based Sound Measurement Applications and Commercial Sound Measurement Devices and Obtaining the Measurement Uncertainty

İsrafil ŞABİKOĞLU*[1], Duygu AKBABA ŞABİKOĞLU[2]

[1] Manisa Celal Bayar University, Faculty of Science and Letters, Department of Physics, Manisa, Turkey
[2] Manisa Celal Bayar University, Institute of Natural and Applied Science, Manisa, Turkey

İsrafil ŞABİKOĞLU, ORCID No: 0000-0002-2260-3326, Duygu AKBABA ŞABİKOĞLU, ORCID No: 0000-0002-5608-2813
*Corresponding author e-mail: israfil.sabikoglu@cbu.edu.tr

Article Info

Recieved: 10.03.2021
Accepted: 11.05.2021
Published August 2021
DOI: 10.53433/yyufbed.894712

Keywords
Android,
Ios,
Commercial devices,
Mobile application,
Sound intensity,
Uncertainty

Abstract: In this study, sound measurement between ios and android operating system based mobile phones (Soundmeter, Decibel X) and commercial sound measurement devices (Cem dt8852, Svantek sv104) was tested. Sound measurement intensities and energies were determined, measurement uncertainties of ios and android devices according to the application were determined. Measurements were carried out at the same time in the indoor and outdoor environment. Iphone 7+ (Ios operation system) and Samsung note 8 (Andorid operation system) used. Significant sound measurement differences were obtained between the two different mobile phone applications. There was no significant difference between commercial measurement devices. Commercial measuring devices were calibrated and can be used as reference devices. Using these devices, it was observed that ios and android-based applications receive faulty measurements on average between 10-20%. As a result of the measurements taken with the applications, it was determined that the measurement uncertainty is in the range of approximately ±4-5dB.

Ortam Gürültü Şiddetinin, Ios ve Android Tabanlı Ses Ölçüm Uygulamaları ile Ticari Ses Ölçüm Cihazları Kullanılarak Karşılaştırılması ve Ölçüm Belirsizliğinin Elde Edilmesi

Makale Bilgileri

Geliş: 10.03.2021
Kabul: 11.05.2021
Yayınlanma Ağustos 2021
DOI: 10.53433/yyufbed.894712

Anahtar kelimeler
Android,
Ios,
Ticari cihazlar,
Mobil uygulama,
Ses şiddeti,
Belirsizlik

Öz: Bu çalışmada, ios ve android işletim sistemi tabanlı cep telefonlarındaki ses ölçüm uygulamaları ile (Soundmeter, Decibel X), ticari ses ölçüm cihazları (Cem dt8852, Svantek sv104) arasındaki ses ölçümü test edilmiştir. Ses ölçüm şiddetleri ve enerjileri belirlenmiş, ios ve android cihazların, uygulamaya göre ölçüm belirsizlikleri belirlenmiştir. Ölçümler iç ve dış ortamda aynı anda gerçekleştirilmiştir. Ios kullanan iphone 7+ ve android kullanan samsung note 8 cihazı kullanılmıştır. İki farklı cep telefonu uygulamaları arasında önemli ses ölçüm farkları elde edilmiştir. Ticari ölçüm cihazları arasında ise önemli bir fark bulunmamıştır. Ticari ölçüm cihazları kalibre edilmiş olduğundan, referans cihaz olarak kullanılabilir. Bu cihazlar kullanılarak, ios ve android tabanlı uygulamaların ortalama %10-20 arasında hatalı ölçüm aldığı gözlenmiştir. Uygulamalar ile alınan ölçümler sonucunda, ölçüm belirsizliği yaklaşık ±4-5dB aralığında olduğu tespit edilmiştir.

1. Introduction

Sound is periodic pressure changes in the atmosphere that can be perceived by our ears. Sound is a form of energy that spreads in waves. Any vibrating object pushes and compresses the air in front of it, and there is a sudden drop in pressure behind the object. At the same time, the air in the back fills this space. With this movement, neighboring molecules vibrate in the same way and vibrations are emitted as a result of the chain movement. This distribution is performed as a sine wave. Such pressure waves in the air reach the ear and vibrate the eardrum. Nerves turn these vibrations into electrical signals and transmit them to the brain, so that the sound in the environment is heard. Sound can be spread in any environment (Serway et.al. ,1999; Serway & Jewet, 2010).

Sound from a source has a certain wavelength, frequency, period, intensity and power. Sounds from different sources can interfere with each other and sound waves of very different frequency and intensity may occur. The measurable intensity of the sound is called decibels (dB). The intensity of the sound is the amount of power passing through the unit surface perpendicular to the separation direction of the wave (Young & Freedman, 2011).

The formula for sound intensity is as follows (Young et.al., 2013);

$$\beta = 10\mathrm{Log}_{10}\,(I/10^{-12}) \qquad (1)$$

where, I is sound intensity (watt/m^2). In the SI unit system, the unit of intensity of the sound is given in decibels (dB – watt/m^2).

Various sound/noise intensities heard around us are given in Figure 1.

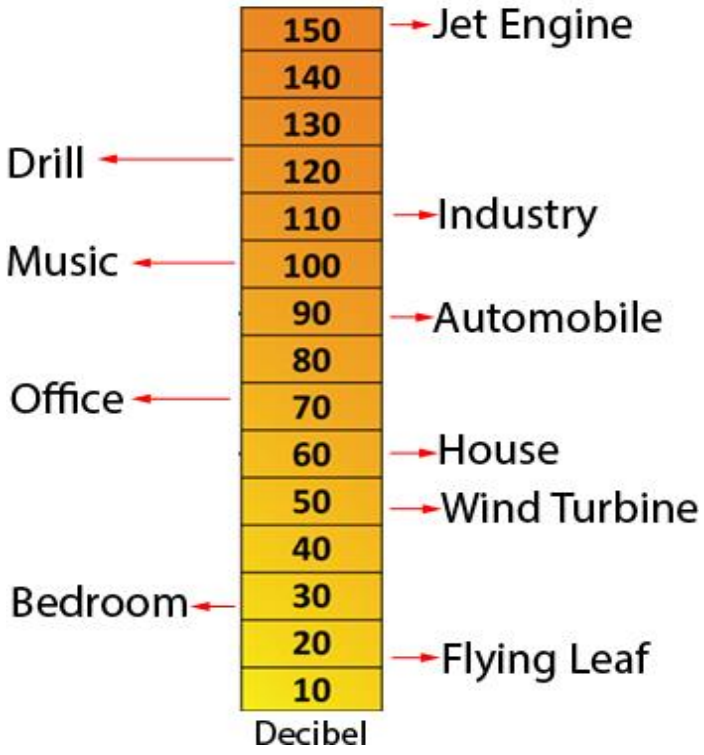

Figure 1. Various intensity of the noises/sounds.

Sound can move at different speeds according to separation medium. The speed of sound separation in a certain environment is calculated as follows (Mazda, 1993);

$$v = \sqrt{\frac{e}{\rho}} \qquad (2)$$

Where, e is elastic modulus of separation medium, and ρ is density. Sound spreads faster in solids and liquids than gases. Under normal conditions, the speed of sound in air is 343 m/s.

Since the intensity of a sound separation in the air is determined logarithmically, it is not possible to perform mathematical direct operations with the decibel unit intensity. Therefore, the decibel sound intensity must be converted into known sound intensity units. A set of semi-empirical formulas can be produced with the sound intensity that can be converted into watt/m^2 with formula (1). Thus, the power (P) and energy (E) of the sound in the environment can be calculated by the following equations;

$$P = I.\ s \tag{3}$$

$$E = P.\Delta t \tag{4}$$

In here, I is the intensity of the sound from (1) equation (watt/m^2), s is the surface cross-sectional area of the microphone on the sound recording device (m^2), and Δt is timekeeping of the sound measurement (s).

Also, the pressure change in the sound can be written as;

$$\Delta p = \sqrt{2\rho v I} \tag{5}$$

In here, ρ is density of the medium, and v is velocity of the sound.

Internationally, sound intensities are examined under 4 groups. Among these groups called A, B, C and D, the dB (A) group is used for the measurement of noise levels perceived by the human ear (TSE, 2014), dB (D) is used to determine the sound levels of jet engines, which are much louder. A sound level measuring device (Decibelmeter) is needed to measure the noise around us. These devices can determine the intensity of the sound in dB. On the other hand, mobile phones can function like sound meters. Environment sound can be recorded with microphones and applications on mobile phones (ANSI, 2007).

In our environment, sounds above 60 dB are called noise and can have significant side effects when exposed to it constantly. Noise is a problem that affects everyone. It has been determined by many researchers that people who stay in high-noise environments for a long time have permanent hearing losses (Sriwattanatamma & Breysse, 2000; Pienskowski et.al., 2013). According to some studies, high sound exposure can cause an average of 16% hearing loss. In addition, according to a study conducted in China, most of the youth working under the age of 16 are exposed to 92dB of loudness and causes serious hearing loss (O'malley et.al. 2009; Sheppard et.al., 2020; Sun et.al., 2021).

According to Occupational Safety and Health Administration (OSHA) and the National Institute for Occupational Safety and Health (NIOSH) organizations, the maximum sound intensity that people can be exposed to has been determined. The maximum sound intensity levels for 8 hours of working per day are specified as 85dB (NIOSH) and 90dB (OSHA) (NIOSH, 1998; May, 2000; OSHA, 2013).

In Turkey, the sound exposure values are determined in accordance with law no. 6331 occupational health and safety law. According to No. 6331 law, it is specified as a maximum of 85db for 8 hours of working per a day (TOG, 2012).

According to some researches, environment sound measurements can be taken with ios and android based applications. In these studies, A type and C type environment sound measurements were taken using different mobile applications and the differences between these applications were shown (Maisonneuve et.al., 2010; Kanhere, 2013; Anonymous, 2013b). It has been reported that there is an average of 2dB difference between mobile applications (Kardousb et.al., 2014). In another study, environment sound analysis was performed with 100 different mobile phones. It has been stated that Ios-based mobile applications are superior to android-based applications and it has been shown that there is an average of 1dB difference (Murphy et.al., 2016). In addition, in another study using both mobile phones and tablets, it has been stated that ios-based applications work more stably and there are average 2dB differences (Maisonnuve et.al., 2009; Kanio, 2010; D'Hondt et.al., 2013).

In present work, the sound levels in indoor and outdoor locations were determined in dB unit with two different sound measurement applications based on Ios and Android and two different

commercial sound measurement devices that calibrated (internationally traceable, accredited). Measurement uncertainties of ios and android based mobile phones were calculated. The energy, power and pressure change of the sound were calculated from the obtained sound intensity values.

2. Materials and Methods

Smart phones (Iphone 7+ for ios-based and Samsung Note8 for android-based) with two different operating systems used in the experimental study. Soundmeter (developed by Faber Acustical) and Decibel X (developed by SkyPaw Ltd.) used in both phones as sound measurement applications. Commercial sound meters Cem DT8852 and Svantek SV104 used. Commercial sound measuring devices were calibrated by an accredited organization and measurement uncertainties were given as 0.5dB and 1dB respectively. Thus, 4 different measurement methods were defined (iphone 7+, samsung note8, Cem, and Svantek).

In indoor and outdoor locations, 10 measurements were taken in 5 seconds ($\Delta t=5s$) at the same time. The mean and standard deviation of the measurements were calculated. In addition, using the relevant equations, measurement intensity, energy and pressure calculated. The measurement chart is given in Figure 2.

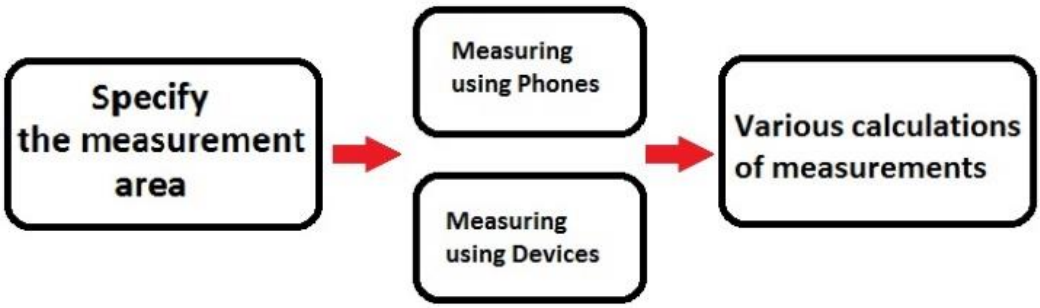

Figure 2. The measurement chart.

Measurements taken from various areas of a university. These areas are named as follows; "Entrance, Canteen/Dining Hall, Park/Resting Area, Classroom, Laboratory". In addition, a box covered with sound insulation material was designed and the muteness measurements of the devices were taken in this box. When there was almost no noise in the environment, the sound data measured by the devices were evaluated in this box.

Sound intensity measured in decibels was converted to I (sound intensity) using equation (1). Later, the P power of the sound intensities was calculated from the formula (3), and the E energies from the formula (4). In addition, the pressure variations of the sound were calculated using the formula (5). For experiments in air environment, ρ; the air density (1,2 kg/m^3) and v; the speed of sound in the air (343 m/s) were used. The measuring range (timekeeping) Δt was evaluated as 5s.

In addition, the surface cross-sectional areas, $s=0.45*10^{-6}m^2$ (for Apple iphone 7+), $s=6.5*10^{-7}m^2$ (for Samsung Note8), $s=9.499*10^{-5}m^2$ (for Cem DT8852), and $s=1.26*10^{-5}m^2$ (for Svantek SV104) were determined from the technical information of the related devices (for iphone and samsung, mic chip sizes are taken, for Cem and Svantek, device manufacturers declarations were taken).

Commercial sound measuring devices used in the study are shown in Figure 3.

Figure 3. Commercial sound measurement devices, (a) Svantek SV104, and (b) Cem DT8852.

3. Results and Discussion

The sound intensity spread in the environment is the sounds that arise from multiple different sources and have different frequencies. Therefore, the sound intensity from each sound source can also be different. Both ios, android-based phones and Cem and Svantek sound measuring devices convert the sound energy that they received from the environment into electronic voltage values. They all display their instantaneous sound values in dB unit. Using these data, the energy, power and pressure difference values of the sound are shown in Table 1.

According to Table 1; sound meter application measured the highest sound value in both ios and android based phones in the canteen and parking area. Values over 80dB were recorded in these areas as well as the sound intensities I in unit of (watt/m^2) were calculated at highest. Similar results were obtained with the Decibel X application. On the other hand, the lowest values were observed in the measurements inside the insulation box. However, the measurements inside the insulation box evaluated separately according to the measurements in other areas. Therefore, it can be said that the lowest sound measurement location is the laboratory according to both the sound meter and the decibel x application.

Commercial measuring devices also recorded the highest and lowest sound values in the canteen and laboratory, respectively. However, there was a measurement difference between commercial sound meters and mobile applications sound data, ranging from an average of 10-20%. Measurements taken with both ios and android-based phones recorded an average of 10-20% more than the measurements taken by commercial sound meters.

Measurements taken in an isolated box can be defined as electrical noises that can be measured when there is almost no sound in the environment. The point to note here is that there is an almost 50% difference between Cem and Svantek devices. Although the uncertainties of both devices are almost the same, there is a difference close to 50% in the measurement's unit in dB. It is thought that this situation may be electronic noise caused by different electronic circuit elements used in Cem and Svantek devices. Sound values (in dB units) recorded by mobile applications and devices in the isolation box are given in Figure 4.

Table 1. Calculated of the average sound intensity in dB and watt/m^2 unit, power (P), energy (E), and pressure difference (Δp).

Measurement Area	Device	Application	dB(A) (average)	I (watt/m^2) x10^{-6}	P (Watt) x10^{-13}	E(Joule) x10^{-11}	ΔP (N/m^2) x10^{-3}
Entrance	Iphone 7+	Sound meter	80.21	104.954	472.294	23.61	293.935
		Decibel X	61.72	1.485	6.687	0.334	34.975
	Samsung Note 8	Sound meter	77	50.118	325.772	16.288	203.119
		Decibel X	62.2	1.659	10.787	0.539	36.962
	Cem DT8852		58.35	0.683	650.0	32.482	23.728
	Svantek SV104		57.43	0.553	69.4	3.472	21.343
Canteen/Dining Hall	Iphone 7+	Sound meter	82.23	167.109	752.0	37.599	370.896
		Decibel X	71.12	12.942	58.2	2.911	103.217
	Samsung Note 8	Sound meter	81.16	130.617	849.0	42.45	327.908
		Decibel X	70.33	10.789	70.1	3.506	94.244
	Cem DT8852		65.3	3.388	3220	160.9	52.814
	Svantek SV104		64.73	2.971	373.0	18.64	49.459
Park/Resting Area	Iphone 7+	Sound meter	81.16	130.617	588.0	29.38	327.908
		Decibel X	74.69	29.444	132.0	6.624	155.687
	Samsung Note 8	Sound meter	82.39	173.38	1130	56.35	377.791
		Decibel X	72.36	17.218	112.0	5.596	119.056
	Cem DT8852		54.37	0.273	260.0	12.99	15.005
	Svantek SV104		54.41	0.276	34.6	1.732	15.075
Classroom	Iphone 7+	Sound meter	68.49	7.063	31.8	1.589	76.252
		Decibel X	54.21	0.263	1.19	0.059	14.731
	Samsung Note 8	Sound meter	68.03	6.353	41.3	2.065	72.319
		Decibel X	55.15	0.327	2.13	0.106	16.415
	Cem DT8852		44.73	0.029	28.2	1.411	4.945
	Svantek SV104		46.96	0.049	6.23	0.312	6.393
Laboratory	Iphone 7+	Sound meter	64.69	2.944	13.2	0.662	49.232
		Decibel X	50.51	0.112	0.506	0.025	9.621
	Samsung Note 8	Sound meter	66.1	4.073	26.5	1.323	57.909
		Decibel X	55.96	0.394	2.56	0.128	18.019
	Cem DT8852		36.22	0.004	3.98	0.198	1.856
	Svantek SV104		39.24	0.008	1.05	0.053	2.628
Isolation Box	Iphone 7+	Sound meter	15.03	$3.18*10^{-5}$	$14.3*10^{-5}$	$0.72*10^{-5}$	0.161
		Decibel X	8	$0.63*10^{-5}$	$2.84*10^{-5}$	$0.14*10^{-5}$	$7.2*10^{-2}$
	Samsung Note 8	Sound meter	15.53	$3.5*10^{-5}$	$23.2*10^{-5}$	$1.16*10^{-5}$	$17.1*10^{-2}$
		Decibel X	7.25	$0.5*10^{-5}$	$3.45*10^{-5}$	$0.17*10^{-5}$	$6.6*10^{-2}$
	Cem DT8852		5.57	$0.4*10^{-5}$	$343*10^{-5}$	$17.12*10^{-5}$	$5.4*10^{-2}$
	Svantek SV104		3.72	$0.2*10^{-5}$	$29.6*10^{-5}$	$1.47*10^{-5}$	$4.4*10^{-2}$

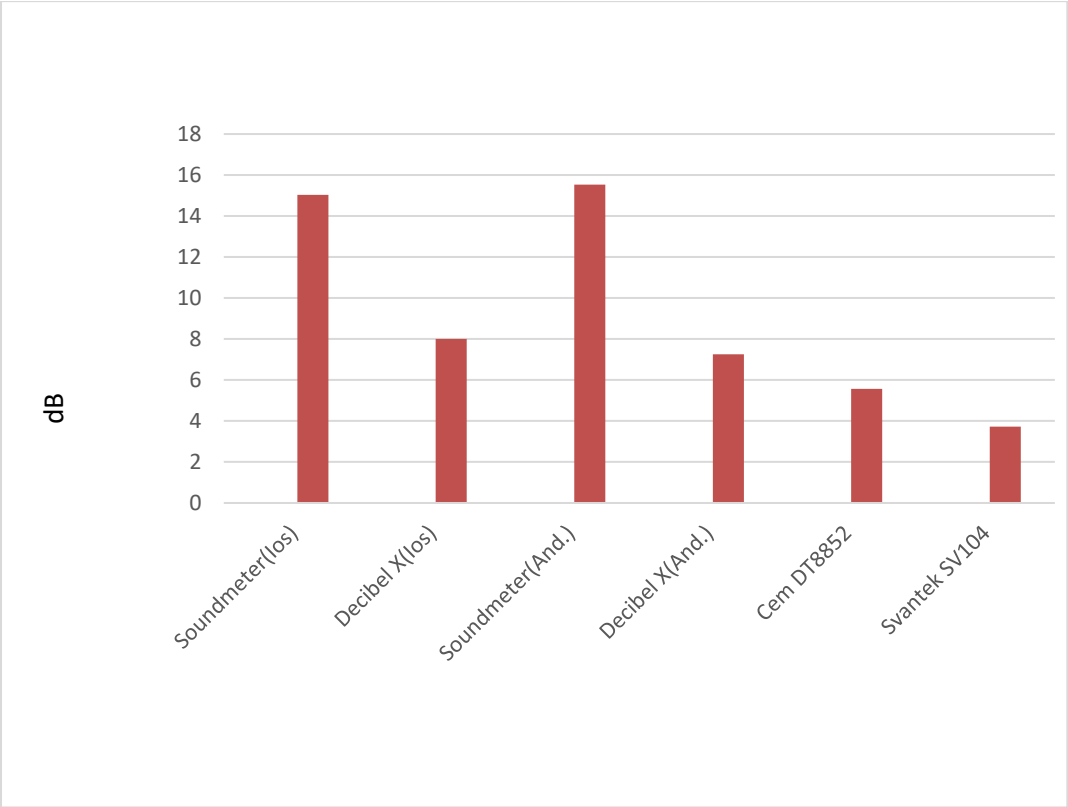

Figure 4. Sound measurement data inside the isolation box.

Looking at Figure 4, certain sound intensities observed in all measurement methods. The lowest sound value observed in Svantek SV104 and the highest sound value observed in android-based phone's applications. The sound values obtained from both ios and android based phones are quite different compared to commercial sound meters. This undermines the reliability of the measurements with the applications on the phone.

The conventional measurement uncertainties of ios and android based mobile phones were obtained. In accordance with the international standards, the metrological measurement uncertainty of a measure/instrument can be examined in two parts as total uncertainty U_T (equation 6) and general uncertainty U_G (equation 7) (Anonymous, 2013a; Damasceno & Couto, 2018).

$$U_T = \mp\sqrt{U_0^2 + U_R^2 + U_{ref}^2} \tag{6}$$

$$U_G = \mp k.U_T \;\; (Coverage\ factor;\ k = 2, for\ 95\%\ reliability) \tag{7}$$

Where, U_0; uncertainty due to the scale of the measuring device, U_R; uncertainty due to repeatability due to device / observer, U_{ref}; uncertainty of the device used as reference.

Also, the U_0 value is calculated as follows (Bell, 2001);

$$U_0 = \frac{1}{\sqrt{3}}.S\ (S; smallest\ scale\ value) \tag{8}$$

In this study, The U_R values are given as the standard deviation of measurements taken at different locations.

In measurement uncertainty calculations, S=1 (smallest scale value of the measurement), coverage factor k=2 (%95), and reference device uncertainty ±0.5dB (Cem DT8852 device's uncertainty) were used. Measurement uncertainties of ios and android based phones calculated according to different regions are given in Table 2.

The average general uncertainties of the ios-based and android-based phones were calculated as ±4.5dB and ±5dB, respectively (Table 2). These values can be considered higher than commercial sound measurement devices.

The correlations between measurement areas and measurement devices (Iphone 7+, Samsung Note8, Cem DT8852, Svantek SV104) are given in Table 3.

A negative correlation was observed with respect to s values in all measurement areas (Table 3). Therefore, it can be said that there is an inverse relationship between I and s. In addition, the relationship between the sound intensities measured by the devices in different measurement areas is shown in Figure 5.

Since there are huge differences in I values, logarithmic scale is used for I values in this graph (Figure 5). It is observed that there is a bigger difference between iphone and Samsung results, if a normal scale graphic is drawn. However, Cem and Svantek values are like each other.

Table 2. U_T and U_G uncertainty values of ios and android based mobile phones.

U_T (Total measurement uncertainty, ±dB)						
		Entrance	Canteen/Dining Hall	Park/Resting Area	Classroom	Laboratory
Ios (Iphone 7+)	Soundmeter	2.1	1.7	2.4	2.3	2.4
	Decibel X	1.6	1.9	3.0	2.5	2.1
Android (Samsung Note8)	Soundmeter	3.1	1.5	1.4	2.4	2.9
	Decibel X	2.0	1.9	1.9	2.5	2.2
U_G (General measurement uncertainty, ±dB)						
		Entrance	Canteen/Dining Hall	Park/Resting Area	Classroom	Laboratory
Ios (Iphone 7+)	Soundmeter	4.3	3.4	4.9	4.6	4.9
	Decibel X	3.2	3.9	6.0	5.1	4.3
Android (Samsung Note8)	Soundmeter	6.1	3.1	2.7	4.7	5.9
	Decibel X	4.0	3.8	3.8	4.9	4.5

Table 3. Correlation values between measurement area sound intensities (I) and measurement devices cross sectional surface areas (s).

	Entrance	Canteen/Dining Hall	Park/Resting Area	Classroom	Laboratory	Isolation Box
Correlation value	-0.59488	-0.63939	-0.632	-0.70277	-0.53053	-0.41199

In Table 4, ANOVA (analysis of variance) values of all measurement method performance according to the areas are given.

P value is less than 0.001, therefore, it can be said that there is a very high significant difference between the measurement areas and the measurement device performance.

Table 4. Anova values of all measurement method according to areas.

Source of Variance	SS	df	MS	F	P-value	F ratio
Between groups	2646.503	5	529.3007	6.08629	0.000895	2.620654
Inside groups	2087.185	24	86.96606			
Total	4733.689	29				

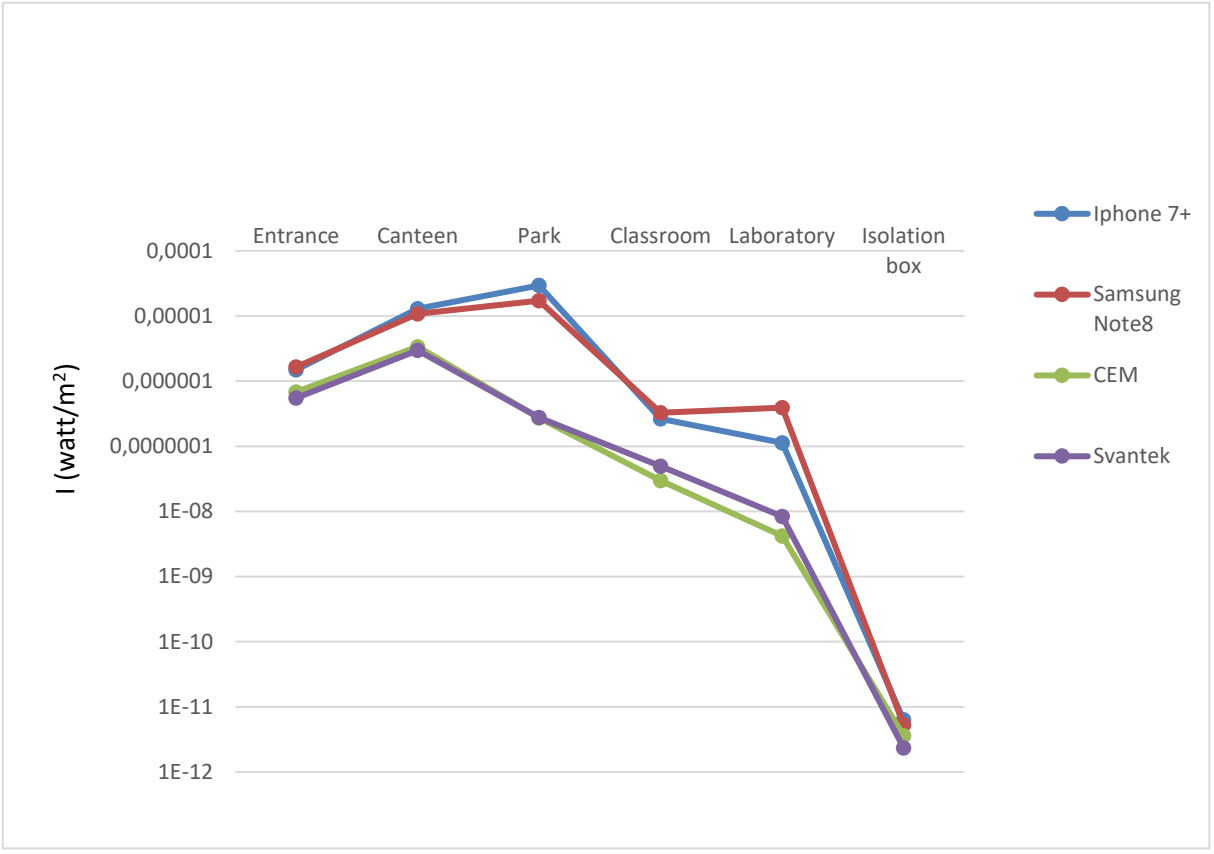

Figure 5. Relationship between I and measurement devices in log scale.

4. Conclusion

In this study, ios and android based sound measurement applications and commercial sound measurement devices were compared. Sound measurements were taken from indoor and outdoor locations. All measurements taken instantaneously. Ios based iphone 7+ device, and android based samsung note8 smart mobile phones were used. Soundmeter and Decibel X mobile applications were selected to measure environment sound with phones. In addition, environment sound measurements were obtained with commercially available devices that named Cem DT8852 and Svantek SV104. These commercial devices were calibrated, and their measurements are internationally traceable.

Sound intensity measurements were calculated using relevant equations for both phone applications and commercial devices. In addition to this, for each measurement area, the sound energy, power, and sound pressure variation calculated. The relationship between telephone applications and commercial sound measuring devices discussed, also the relationships between sound intensity and measurement environments evaluated.

According to the obtained results, the following determinations can be written;

The environment noise/sound was obtained in dB unit using all measurement methods. Since sound intensity obtained instantaneously, all measurement methods could be compared.

In the environment sound measurements, the highest sound intensity was obtained in the park/resting area. All measurement methods showed the same result. However, sound measurement values recorded with cell phones were obtained higher than others.

Commercial devices recorded almost identical results in environment sound measurements. Since these devices calibrated, they can be defined as reference devices for environment sound measurements and can be used anywhere for all sound measurements.

A sound-isolated box was designed to evaluate the difference in recording sound in a quiet environment for each measurement method. Soundmeter application, which is a mobile phone

application, showed the highest value in sound measurements performed in the box. However, the other mobile application, Decibel X, recorded a sound intensity value of almost half. Sound measurements recorded with mobile phone applications in a solation box can be called whisper-level audio data. On the other hand, almost no sound was recorded with commercial sound measurement devices. In this case, it can be said that there is electronic noise in a quiet environment for mobile phone applications. These electronic noises are about 13dB, and 7dB for soundmeter and decibel x, respectively.

Since the sound recorded with different measurement methods in the same measurement areas, the correlations between these measurement areas and the measurement methods were evaluated and it was calculated to be negative. Therefore, it can be said that there is an inverse relationship between the measurement environment and measurement methods.

The relationship between the measured sound intensity and the measurement cross-section surface area used in each measurement method was examined. The highest sound intensity was achieved with the iphone 7+ in the park location. On the other hand, commercial devices measured the same level of sound intensity as each other.

In addition, Anova analysis was carried out with measurement methods in the measurement areas. It can be said that there is a highly significant difference between measurement methods and measurement areas.

In general, it can be said that there is an average of 5% difference between the soundmeter application and the Decibel X application in sound measurements recorded by mobile phones. Soundmeter application measured higher sound intensity values in the same environment. On the other hand, commercial devices recorded almost the same sound intensity values in the same environment. Compared to these commercial devices, mobile phone applications showed an average of 10-20% difference measurement of sound intensity. Both ios and android based applications measured higher volume values between 10-20%. The general uncertainty values of mobile phones are found as ±4,5dB, and ±5dB, for iphone7+ and samsung note8, respectively. These values can be considered higher than commercial sound meters.

In this study, sound intensity data were obtained in indoor and outdoor environments with different mobile phone applications and commercial sound measuring devices. It is concluded that mobile phone applications are not reliable enough. In addition, it was observed that common areas (such as park and canteen) are very close to the maximum sound intensity limit according to the international standard.

By means of the developing technology, only an idea can be obtained with mobile phone sound measurement applications that can be accessed by almost everyone, however, it is thought that these devices cannot be used for a scientific measurement.

References

ANSI. (2007). ANSI S1.4-1983, S*pecification for Sound Level Meters, American National Standards Institute,* New York.

Anonymous, (2013a). Expression of the Uncertainty of Measurement in Calibration. EA-European Co-operation for Accreditation, EA-4/0. https://european-accreditation.org/wp-content/uploads/2018/10/ea-4-02-m-rev01-september-2013.pdf Accessed time 25.01.2021.

Anonymous, (2013b). European environment agency report. Environmental indicator report. http://www.eea.europa.eu/publications#c7=en&c11=5&c14=&c12=&b_start=0 Accessed time 25.01.2021.

Bell, S. (2001). *A Beginner's Guide to Uncertainty of Measurement*, issue2, (pp.13-15), Crown, UK, HMSO.

Damasceno , J.C. & Couto, P.R.G. (2018). *Methods for Evaluation of Measurement Uncertainty*, (C2), IntechOpen, Open Access Books. doi:10.5772/intechopen.74873

D'Hondt, E., Stevens, M., & Jacobs, A. (2013). Participatory noise mapping works! An evaluation of participatory sensing as an alternative to standard techniques for environmental monitoring. *Pervasive Mobile Computing*, 9, 681–94. doi:10.1016/j.pmcj.2012.09.002

Kanhere, S.S. (2013). *Participatory sensing: Crowdsourcing data from mobile smartphones in urban space. Distributed computing and internet technology*. ICDCIT 2013. Lecture Notes in

Computer Science, (pp.19-26). Berlin, Germany: Springer. doi:10.1007/978-3-642-36071-8_2Springer.

Kanjo, E. (2010). NoiseSPY: A Real-time mobile phone platform for urban noise monitoring and mapping. *Mobile Networks and Applications*, 15, 562–574. doi:10.1007/s11036-009-0217-y

Kardousb, C.A., & Shaw P.B., (2014). Evaluation of smartphone sound measurement applications. *The Journal of the Acoustical Society of America*, 135 (4), ELI186. doi:10.1121/1.4865269

Maisonneuve, N., Mathias, N., & Ochab, B. (2010). Participatory noise pollution monitoring using mobile phones. *Information Polity*, 15, 51-71. doi:10.3233/IP-2010-0200

Maisonnuve, N., Stevens, M., Niessen, M.E., Haneppe, P., & Steels, L. (2009). Citizen noise pollution monitoring. Proceedings of the 10th annual international conference on digital government research: social networks. *Digital Government Society of North America*, 96-103.

May, J.J. (2000). Occupational hearing loss. *American Journal of Industrial Medicine* , 37(1), 112-20. doi:10.1002/(SICI)1097-0274(200001)37:1<112::AID-AJIM9>3.0.CO;2-%23

Mazda, F. (1993). *Telecommuniciations Engineer's Reference Book*, (S8.4). USA, Butterworth-Heinemann.

Murphy, E., & King, A. (2016). Testing the accuracy of smartphones and sound level meter applications for measuring environmental noise. *Applied Acoustics*, 106, 16–22. doi:10.1016/j.apacoust.2015.12.012

NIOSH. (1998). *Criteria for a Recommended Standard, Occupational Noise Exposure*. Public no.98-126. Ohio.

O'malley, V., King, E., Kenny, L., & Dilworth, C. (2009). Assessing methodologies for calculating road traffic noise levels in Ireland – Converting CRTN indicators to the EU indicators (L_{den}, L_{night}). *Applied Acoustics*, 70, 284–296. doi:10.1016/j.apacoust.2008.04.003

OSHA. (2013). OSHA 1683 standard. http://www.osha.gov/dts/osta/otm/new_noise Accessed time 25.01.2021.

Pienkowski, M., Munguia, R., & Eggermont, J.J. (2013). Effects of passive, moderate-level sound exposure on the mature auditory cortex: Spectral edges, spectrotemporal density, and real-world noise. *Hearing Research*, 296, 121–130. doi:10.1016/j.heares.2012.11.006

Serway, R., Beichner, R., & Jewett, J. (1999). *Physics for Scientists and Engineers, 5th edition*, (pp. 520-535). Boston, USA: Brooks cole.

Serway, R., & Jewett, J., (2010). *Physics for Scientists and Engineers with Modern Physics, 10th edition*, (pp. 507-522). Boston, USA: Brook cole.

Sheppard, A., Ralli, M., Gilardi, A., & Salvi, R. (2020). Occupational Noise: Auditory and Non-Auditory Consequences. *International Journal of Environmental Research and Public Health* , 17(23), 8963. doi:10.3390/ijerph17238963

Sriwattanatamma, P., & Breysse, P. (2000). Comparison of NIOSH noise criteria and OSHA hearing conservation criteria. *American Journal of Industrial Medicine*, 37,334–338. doi:10.1002/(SICI)1097-0274(200004)37:4<334::AID-AJIM2>3.0.CO;2-Z

Sun, D.W., Wang, B., Guo, H., Wang, N., Gao, D., & Zhu, B. (2021). Single nucleotide polymorphisms in JNK1 are associated with susceptibility to noise-induced hearing loss in a Chinese population. *International Archives of Occupational and Environmental Health*, Accepted paper. doi:10.1007/s00420-020-01644-0

TSE. (2014). Turkish Standards Institution TSE 61672-1 standard. http://intweb.tse.org.tr/Standard/Standard/Standard.aspx?081118051115108051104119110104055047105102120088111043113104073083065084050121081083112073117103 Accessed time 27.01.2021.

TOG. (2012). Turkish 6331 no, Occupational health and safety law. *Turkish Official Gazette*. http://www.mevzuat.gov.tr/mevzuat?MevzuatNo=6331&MevzuatTur=1&MevzuatTertip=5 Accessed time 25.01.2021.

Young, H., & Freedman, R. (2011). *Sears&Zemansky University Physics, V1, 10th edition*, (pp. 521-540). Melbourne, USA: Addison Wesley.

Young, H, Freedman, R., & Ford, L. (2013). *Sears&Zemansky University Physics with Modern Physics, 13th edition*, (pp. 488-510). Melbourne, USA: Addison Wesley.

Yüzüncü Yıl Üniversitesi
Fen Bilimleri Enstitüsü Dergisi

http://dergipark.gov.tr/yyufbed

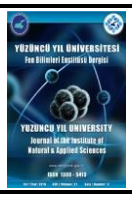

Araştırma Makalesi

Antimikrobiyal ve Antikanser Aktiviteye Sahip Cyclo(Trp-Trp) Dipeptidinin 3-Boyutlu Moleküler Yapısı

Sefa ÇELİK [*1], Sevim AKYÜZ[2], Ayşen ERBÖLÜKBAŞ ÖZEL[1]

[1] İstanbul Üniversitesi, Fen Fakültesi, Fizik Bölümü, 34134, İstanbul, Türkiye
[2] İstanbul Kültür Üniversitesi, Fen-Edebiyat Fakültesi, Fizik Bölümü, 34156, İstanbul, Türkiye

Sefa ÇELİK, ORCID No: 0000-0001-6216-1297, Sevim AKYÜZ, ORCID No: 0000-0003-3313-6927,
Ayşen ERBÖLÜKBAŞ, ÖZEL ORCID No: 0000-0002-8680-8830
*Sorumlu yazar e-posta:scelik@istanbul.edu.tr

Makale Bilgileri

Geliş: 02.04.2021
Kabul: 24.05.2021
Yayınlanma Ağustos 2021
DOI: 10.53433/yyufbed.908710

Anahtar Kelimeler
Cyclo(Trp-Trp),
Triptofan,
Konformasyon Analizi,
Moleküler Modelleme

Öz: Antimikrobiyal ve antikanser gibi önemli biyolojik aktivitelere sahip olan Cyclo(Trp-Trp) dipeptidinin ($C_{22}H_{20}N_4O_2$) en düşük enerjili moleküler geometrisi, teorik konformasyon analizi hesabını takiben yapılan Yoğunluk Fonksiyoneli Teorisi hesaplamalarıyla belirlenmiştir. İlk olarak Ramachandran haritaları ve yan zincir dihedral açıları (χ) katkısıyla yapılan konformasyon analizi ile dipeptide ait en olası moleküler geometriler belirlenmiş, bunlar içerisinden en düşük enerjili sekiz konformasyona ait dihedral açılar konformasyon analizi öncesi ve sonrası olmak üzere karşılaştırmalı olarak verilmiştir. Bu konformasyonlara ait toplam enerji ve toplam enerjiye katkı veren van der Waals, elektrostatik, hidrojen ve torsiyon enerjileri hesaplanmıştır. Bu sekiz konformasyon içerisinden en düşük enerjili konformer, Gaussian03 programına başlangıç verisi olarak tanıtılmış ve DFT/B3LYP/6-31++G(d,p) teori seviyesinde optimize edilmiştir. Ayrıca teorik konformasyon analizi sonucunda bulunan en düşük enerjili konformer ile optimize moleküler geometri karşılaştırmalı olarak verilerek dihedral açılardaki değişimler belirlenmiştir.

3-Dimensional Molecular Structure of Cyclo (Trp-Trp) Dipeptide with Antimicrobial and Anticancer Activity

Article Info

Recieved: 02.04.2021
Accepted: 24.05.2021
Published August 2021
DOI: 10.53433/yyufbed.908710

Keywords
Cyclo(Trp-Trp),
Tryptophan,
Conformational analysis,
Molecular modeling

Abstract: The lowest energy molecular geometry of the Cyclo(Trp-Trp) dipeptide ($C_{22}H_{20}N_4O_2$), which has important biological activities such as antimicrobial and anticancer, was determined by Density Functional Theory calculations made following theoretical conformation analysis calculation. First, the most probable molecular geometries of the dipeptide were determined with the contribution of Ramachandran maps and sidechain dihedral angles (χ), and the dihedral angles belonging to the eight conformations with the lowest energy were tabulated in comparison with before and after conformation analysis. The total energy of these conformation and van der Waals, electrostatic, hydrogen and torsion energy values contributing to this total energy were calculated. Among these eight conformations, the lowest energy conformer was introduced as the starting data to the Gaussian03 program and optimized at DFT/B3LYP/ 6-31++G(d,p) level of theory. In addition, the changes in dihedral angles were determined by comparing the lowest energy conformer found as a result of theoretical conformation analysis and optimized molecular geometry.

1. Giriş

2,5-Diketopiperazinler (DKP), iki amino asitten oluşan halka dipeptitlerdir. Son yıllarda DKP'ler, katı yapıları ve yan zincirleri nedeniyle ilaç keşfi alanında dikkat çekmektedir (Wang, 2013). DKP'lerin yapıları, reaksiyonları, tıbbi kimyasal özellikleri ve potansiyel terapötik uygulamaları ile ilgili çalışmalar literatürde mevcuttur (Borthwick, 2012; Huang ve ark., 2014). Ayrıca, DKP'ler, gelecekte potansiyel tıbbi kullanım için büyük bir umut vaat eden keşfedilmemiş bir biyoaktif halka peptittir (Huang ve ark., 2014). İnsan kolon kanseri hücre hatlarından biri olan HT-29 hücre hatlarının, histidin aminoasiti içeren cyclo(Gly-His) ve cyclo(Ala-His) gibi siklik (cyclo) dipeptitlerle önemli ölçüde inhibe edildiği gözlenmiştir (Kilian ve ark., 2013). Cyclo(Gly-Leu) dipeptidi başta rahim ağzı, kolon ve meme kanserleri olmak üzere önemli biyolojik aktivitelere sahiptir (Van der Merwe ve ark., 2008). Cyclo(Gly-Arg-Gly-Asp-Ser-Pro-Ala) (GRGDSPA) heptapeptidi kanser hücrelerinin metastazını etkili bir şekilde inhibe edebilmektedir (Zhu ve ark., 2009). 2020 yılında doğrusal ve halka peptitler üzerine yapılan çalışmada incelenen halka peptitlerin daha yüksek antienflamatuar aktivite sergilediği ve bu sayede bu bileşiklerin enflamatuar bozuklukların tedavisinde daha iyi aktivite gösterdiği bulunmuştur (Kaur ve ark., 2020). Cyclo (-Pro-Tyr) dipeptidinin antikanser molekül olarak kullanılabileceği ve karaciğer kanserini, normal hücreleri etkilemeden, tedavi etmek için bu dipeptidin yeni bir strateji oluşturabileceği bulunmuştur (Karanem ve ark., 2020).

2000 yılında halka dipeptitler üzerine yapılan çalışmada cyclo(trp-trp) dipeptidinin kanser terapisinde kullanılabilecek bir ajan olduğu bulunmuştur (Graz ve ark., 2000). Halka dipeptitler üzerine yapılan çalışmalarda cyclo(trp-trp) dipeptidinin antibakteriyel ve antifungal aktiviteye sahip olduğu gözlenmiştir (Milne ve ark., 1998; Mander & Liu, 2010). 2010 yılında yapılan çalışmada da bu dipeptidin bazı bakteri türlerine karşı antimikrobiyal aktiviteye sahip olduğu bulunmuştur (Lee ve ark., 2010).

Yapı-aktivite ilişkisi, benzer yapılara sahip kimyasalların benzer biyolojik aktiviteler sergilediğini belirten "benzer özellik" ilkesine dayanmaktadır (Tong ve ark., 2003; Johnson & Maggiora, 1990).

Bu ilişki kapsamında cyclo(trp-trp) dipeptidinin aktivite gösterdiği en kararlı yapının, yani konformerin, belirlenmesi bu aktivitenin açıklanmasında anahtar bir role sahiptir. Bu çalışmada olası konformasyonların belirlenebilmesi için, aminoasitlerin φ, ψ ve χ dihedral açılarının tanımlandığı Ramachandran haritaları (Ramachandhan ve ark., 1963; Ramachandhan, 1968) kullanılarak moleküler mekanik yaklaşıma dayalı hesaplama yapan teorik konformasyon analizi (TKA) programı kullanılmıştır (Maksumov ve ark., 1983).

Hesaplama sonrası bulunan konformasyonlar arasından en düşük enerjili sekiz konformasyon ayrıntılı olarak incelenmiştir. Bu kapsamda en kararlı 8 konformasyona ait toplam enerji ve bu enerjiye olan katkılar, triptofan aminoasidinin konformasyon analizi öncesi ve sonrasındaki yan zincirine ait dihedral açıdaki değişimler Maksumov vd. tarafından yazılan TKA programı kullanılarak hesaplanmıştır (Maksumov ve ark., 1983). Son olarak bu sekiz konformasyon arasından da en düşük enerjili konformer Gaussian programına giriş verisi olarak tanıtılarak yoğunluk fonksiyoneli teorisi ile optimize edilmiştir. TKA hesabı ile bulunan en düşük enerjili konformer ile optimize geometri karşılaştırılarak yan ve ana zincirdeki değişimler belirlenmiştir.

2. Materyal ve Yöntem

TKA hesabında konformasyonlar, toplam enerjileri ve bu enerjiye katkı sağlayan van der Waals etkileşimleri, elektrostatik etkileşimler, hidrojen bağları ve dönü enerjisi ile birlikte hesaplanmaktadır.

Van der Waals enerjisi 1966 yılında Scott ve Scheraga tarafından belirlenen Slater-Kirkwood denkleminden yararlanılarak Lennard-Jones 6-12 potansiyel fonksiyonu ile hesaplanmıştır (Scott & Scheraga, 1966).

Elektrostatik enerji, bir moleküldeki atomlar üzerinde lokalize edilmiş net yüklere bağlı olarak monopol yaklaşımı ile Coulomb yasası temelinde hesaplanır (Mlynek ve ark., 1980).

Tekli bağlar etrafında rotasyona engelden (torsiyon bariyeri) sorumlu olan temel enerji bileşenlerini belirleyebilmek için uygulanan teorik modellemelere rağmen, bu engelin kaynağı tam olarak anlaşılmamıştır. Bu nedenle, bunların elektrostatik, van der Waals ve hidrojen bağ katkılarıyla yeterince temsil edilmediği durumlarda, torsiyon bariyerlerini kalibre etmek için deneysel veriler

kullanılmıştır. Torsiyon potansiyellerinin bariyer yükseklikleri ilgili deneysel verilerin mevcut olmadığı durumlarda ise teorik hesaplama sonuçları kullanılmıştır (Momany ve ark., 1975; Mills ve ark., 1988).

Hidrojen bağ enerjisi, sulu çözeltiler için r = 1.8 Å bağ uzunluğuna karşılık gelen 1.5 kcal / mol hidrojen bağı ayrışma enerjisi değerine sahip Morse potansiyeli kullanılarak belirlenmektedir (Akverdieva & Godjayev, 2017).

Maksumov vd. tarafından yazılan TKA programında (Maksumov ve ark., 1983), giriş verisi olarak tanıtılan dihedral açılar IUPAC-IUB'a göre belirlenmiştir (Mills ve ark., 1988). Hesaplanan tüm konformasyonlar arasından en düşük enerjili sekiz konformer belirlenmiştir. Bunlar arasından en düşük enerjili konformer (I) Gaussian03 programına (Frisch ve ark., 2003) başlangıç verisi olarak tanıtılarak Yoğunluk Fonksiyoneli Teorisi (Becke, 1993), B3LYP fonksiyoneli ve 6-31++G(d,p) baz seti ile optimize edilmiş ve Mulliken yükleri hesaplanmıştır.

3. Bulgular

TKA hesabında Cyclo(Trp-Trp) dipeptidinin giriş verisi olarak DKP halkası düzlemsel olarak tanıtılmıştır ve olası konformasyonlar yan zincir dihedral açılarına bağlı olarak belirlenmiştir (Degeilh & Marsh, 1959; Dorset, 2010).

TKA hesabı öncesi ve sonrasına ait yan zincir dihedral açılardaki değişim ve konformasyonlara ait enerjiler Çizelge 1 ve Çizelge 2' de gösterilmiştir. Bu konformasyonlar Şekil 1' de verilmiştir.

Yoğunluk Fonksiyoneli Teorisi ile hesaplanan optimize geometri ile yük dağılımı Şekil 2 ve Şekil 3'de gösterilmiştir. Konformasyon analizi ve Yoğunluk Fonksiyoneli Teorisi hesabı sonrası moleküler geometriye ait dihedral açılardaki değişim Çizelge 3' de verilmiştir.

TKA hesabı sonrasında en kararlı sekiz konformere ait enerjiler sırasıyla -9.28, -8.29, -7.77, -7.74, -7.51, -7.34, -6.49 ve -5.98 kcal/mol olarak hesaplanmıştır ve toplam enerjiye en fazla katkının van der Waals enerjisinden olduğu belirlenmiştir. Bu katkı sırasıyla -9.79, -8.78, -8.56, -8.30, -8.03, -8.17, -7.14 ve -6.80 kcal/mol'dür. Demir & Godjaev (2002) tarafından Pol-Rfamide II heptapeptidi üzerine yapılan çalışma da olası konformasyonlar için molekülün kararlılığında van der Waals etkileşmesinin en önemli katkıyı sağladığı, diğer önemli katkıların ise sırasıyla elektrostatik ve torsiyon etkileşmeleri olduğu bulunmuştur. Alieva ve ark. (2006) tarafından tirozin hidroksilazın N-terminal dizisi Met1-Val60 üzerine yapılan konformasyon analizi hesabında olası kararlı konformasyonlarda -212.0 ile -236.3 kcal/mol aralığında van der Waals etkileşiminin en yüksek katkıyı sağladığı bulunmuştur. Celik & Kecel-Gunduz (2017) tarafından Cyclo(Tyr-Cys) ve Cyclo(Phe-Cys) dipeptitleri üzerine yapılan konformasyon analizinde van der Waals etkileşiminin yüksek katkı sağladığı bulunmuştur.

Konformasyon analizi ve Yoğunluk Fonksiyoneli Teorisi optimizasyonu sonrasında bulunan en kararlı konformasyonlar incelendiğinde (Şekil 4), triptofan aminoasitine ait yan zincirin DKP halkası üzerine doğru büküldüğü ve bu iki aminoaside ait yan zincirlerin birbirlerine yaklaştığı bulunmuştur. Ayrıca TKA hesabında düzlemsel kabul edilen DKP halkasının, Yoğunluk Fonksiyoneli Teorisi optimizasyonu sonucunda düzlemsele yakın olduğu bulunmuştur (Şekil 4). Yoğunluk Fonksiyoneli Teorisi optimizasyonu sonucunda DKP halkası üzerindeki w1(N1-C47), w2(C23-N25), φ1(N1-C3), φ2(N25-C27), Ψ1(C3-C23) ve Ψ2(C27-C47) dihedral açıları sırasıyla -2.6˚, -11.9˚, 6.8˚, 15.7˚, 0.2˚, -7.7˚ hesaplanmıştır. Celik ve ark. (2012) tarafından Cyclo(His-Phe) dipeptidi üzerine DFT/B3LYP/ 6-31++G(d,p) teori seviyesinde yapılan hesaplamalarda DKP halkası üzerindeki dihedral açılar sırasıyla -4.31˚, -9.86˚, 12.40˚, 7.05˚, -4.82˚ ve -0.11˚ hesaplanmıştır. Mendham ve ark. (2009) tarafından cyclo(L-Ser-L-Ser) dipeptidi üzerine yapılan X ışını kristalografisinde bu dihedral açılar 4.5˚, 5.4˚,-4.1˚, -3.2˚, -1.0˚ ve -1.7˚ bulunmuştur.

TKA hesabının, Yoğunluk Fonksiyoneli Teorisi optimizasyonu ile benzer sonuç vermesi, TKA hesabının Yoğunluk Fonksiyoneli Teorisi optimizasyonu için başlangıç parametresi olarak kullanılabileceğini ve bu sayede de daha kısa sürede doğru sonuçlar alınabileceğini göstermektedir.

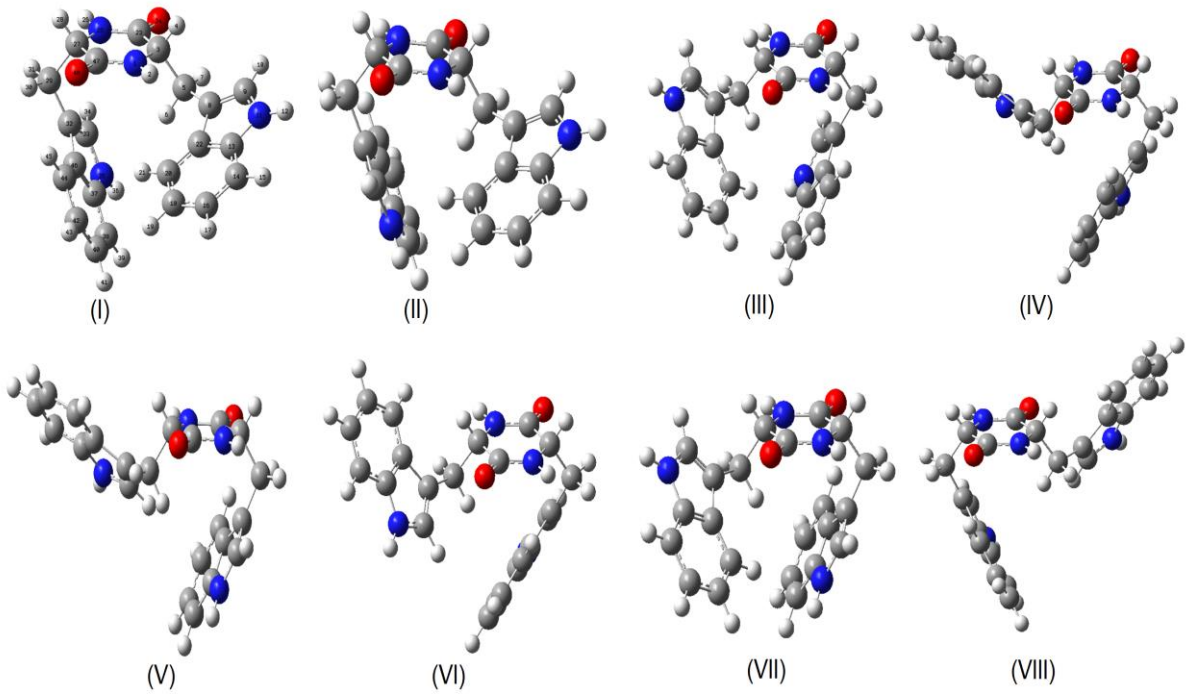

Şekil 1. Cyclo(Trp-Trp) dipeptidine ait en kararlı sekiz konformer

Çizelge 1. Cyclo(Trp-Trp) dipeptidinin en düşük enerjili sekiz konformerinin TKA hesabı öncesi (giriş) ve sonrasına ait (çıkış) yan zincir dihedral açılardaki değişim (°) ve konformasyonlara ait enerjiler

Konformer	$E_{bağıl}$ (kcal/mol)	E_{toplam} (kcal/mol)		χ 11	χ 12	χ 21	χ 22
(I)	0	-9.28	GİRİŞ	-60.0	-90.0	60.0	-90.0
			ÇIKIŞ	-56.4	-88.9	66.5	-81.1
(II)	0.99	-8.29	GİRİŞ	-60.0	-90.0	60.0	90.0
			ÇIKIŞ	-57.9	-89.3	65.3	94.3
(III)	1.51	-7.77	GİRİŞ	60.0	90.0	180.0	90.0
			ÇIKIŞ	62.9	93.6	196.0	66.8
(IV)	1.54	-7.74	GİRİŞ	60.0	90.0	-60.0	90.0
			ÇIKIŞ	70.9	107.3	-53.9	101.5
(V)	1.77	-7.51	GİRİŞ	60.0	-90.0	-60.0	90.0
			ÇIKIŞ	58.2	-92.8	-52.7	94.2
(VI)	1.94	-7.34	GİRİŞ	60.0	90.0	180.0	-90.0
			ÇIKIŞ	70.7	108.5	195.9	-119.6
(VII)	2.79	-6.49	GİRİŞ	60.0	-90.0	180.0	90.0
			ÇIKIŞ	56.6	-90.6	193.7	65.1
(VIII)	3.3	-5.98	GİRİŞ	180.0	-90.0	60.0	-90.0
			ÇIKIŞ	197.2	-122.2	59.6	-88.6

Çizelge 2. Cyclo(Trp-Trp) dipeptidinin en kararlı konformerlerine ait enerji katkıları

Konformer	$E_{bağıl}$ (kcal/mol)	E_{toplam} (kcal/mol)	$E_{van\ der\ Walls}$ (kcal/mol)	$E_{elektrostatik}$ (kcal/mol)	$E_{torsiyon}$ (kcal/mol)
(I)	0	-9.28	-9.79	0.04	0.47
(II)	0.99	-8.29	-8.78	0.03	0.46
(III)	1.51	-7.77	-8.56	0.06	0.73
(IV)	1.54	-7.74	-8.30	0.03	0.53
(V)	1.77	-7.51	-8.03	0.02	0.50
(VI)	1.94	-7.34	-8.17	0.05	0.78
(VII)	2.79	-6.49	-7.14	0.05	0.60
(VIII)	3.3	-5.98	-6.80	0.05	0.77

Çizelge 3. Cyclo(Trp-Trp) dipeptidinin yan zincir torsiyon açılarındaki (°) değişim

Cyclo(Trp-Trp)	χ11	χ12	χ21	χ22
TKA	-56.4	-88.9	66.5	-81.1
DFT-B3LYP/6-31++G(d,p)	-65.9	-90.3	64.2	-86.4

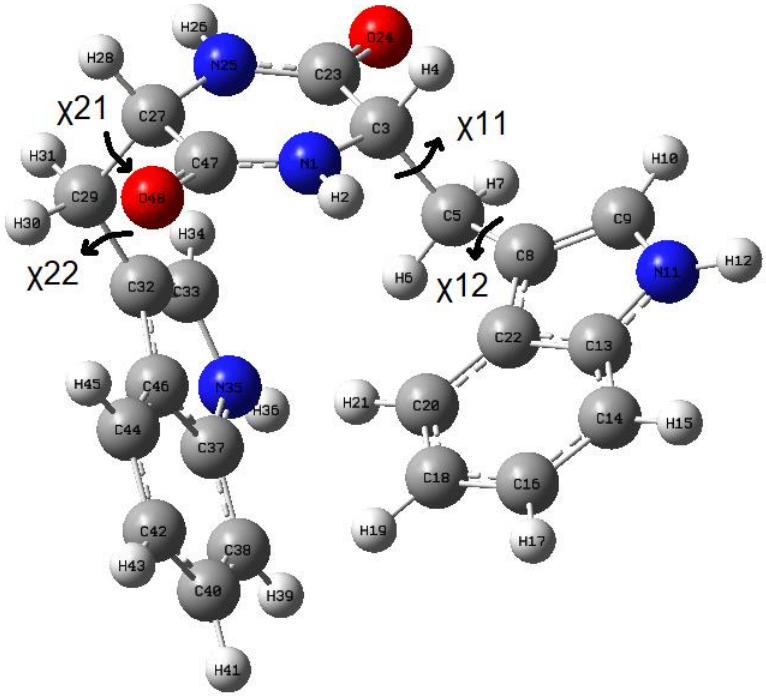

Şekil 2. Cyclo(Trp-Trp) dipeptidinin DFT/B3LYP/6-31++G(d,p) teori seviyesinde optimize yapısı

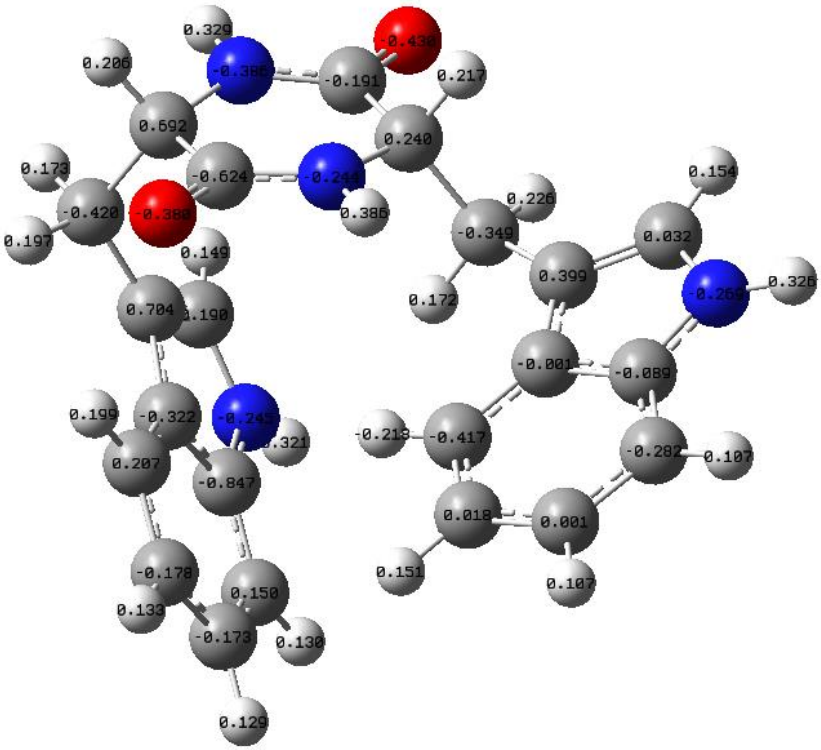

Şekil 3. Dipeptidin optimize yapısına ait yük dağılımı

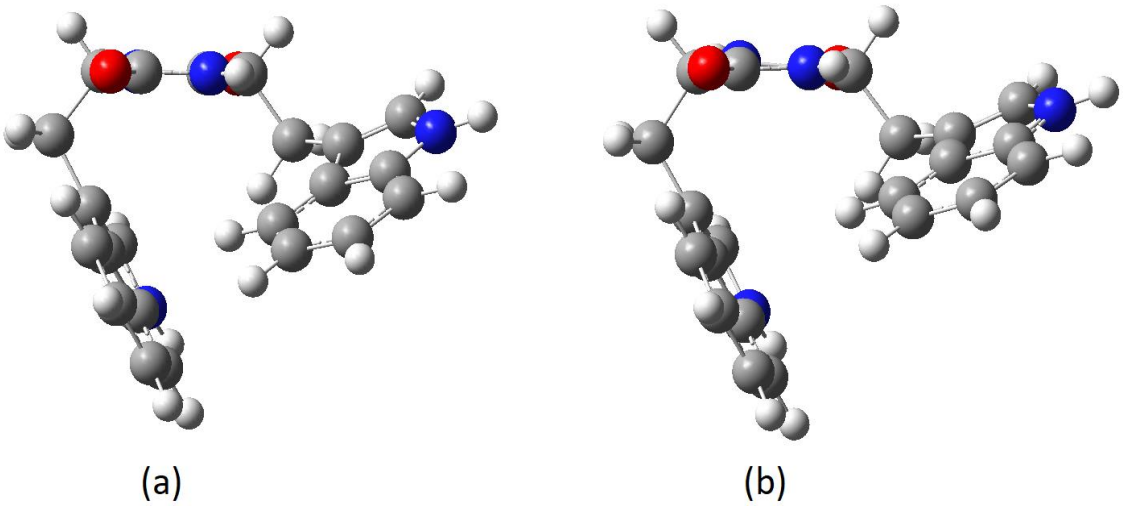

Şekil 4. Cyclo(Trp-Trp) dipeptidinin TKA (a) ve DFT/B3LYP/6-31++G(d,p) teori seviyesi optimizasyonu (b) sonrası moleküler geometri karşılaştırması

4. Tartışma ve Sonuç

Bu çalışmada, Cyclo(Trp-Trp) dipeptidinin teorik konformasyon analizi sonrası belirlenen en kararlı konformeri Yoğunluk Fonksiyoneli Teorisi, B3LYP fonksiyoneli ve 6-31++G(d,p) baz seti kullanılarak incelenmiştir. Hesaplama sonrası dipeptide ait optimize geometride DKP halkasının düzlemsele yakın olduğu ve yan zincire ait yönelimin teorik konformasyon analizi ile belirlenen en düşük enerjili konformasyon ile son derece uyumlu olduğu gözlenmiştir. Cyclo(Trp-Trp) dipeptidinin konformasyon olasılıklarının belirlenmesi, bir ilaç olarak fonksiyonlarının anlaşılabilmesi bakımından

oldukça önemlidir. Diketopiperazin türevi moleküllerin sentezinde belirlenen bu konformasyonlar referans olarak kullanılabilir.

Teşekkür

Bu çalışma, İstanbul Üniversitesi Bilimsel Araştırma Projeleri Yürütücü Sekreterliğinin ÖNAP-2423 numaralı projesi ile desteklenmiştir.

Kaynakça

Akverdieva, G., & Godjayev, N.M. (2017). Improvement of program of calculation of molecular conformation. *Journal of Modern Technology and Engineering*, 2(2), 140-145.

Alieva, I. N., Mustafayeva, N. N., & Gojayev, N. M. (2006). Conformational analysis of the N-terminal sequence Met1–Val60 of the tyrosine hydroxylase. *Journal of Molecular Structure*, 785(1-3), 76-84. doi: 10.1016/j.molstruc.2005.09.026

Becke, A.D. (1993). Density-functional thermochemistry, III. The role ofexact Exchange. *The Journal of chemical Physics*, 98(7), 5648–5652. doi: 10.1063/1.464913

Borthwick, A.D. (2012). 2,5-Diketopiperazines: synthesis, reactions, medicinal chemistry, and bioactive natural products. *Chemical reviews*, *112*(7), 3641-3716. doi: 10.1021/cr200398y

Celik, S., Ozel, A. E., Kecel, S., & Akyuz, S. (2012). Structural and IR and Raman spectral analysis of cyclo (His-Phe) dipeptide. *Vibrational Spectroscopy*, 61, 54-65. doi:10.1016/j.vibspec.2012.01.014

Celik, S., & Kecel-Gunduz, S. (2017). Conformational Analysis of Cyclo (Tyr-Cys) and Cyclo (Phe-Cys) Dipeptides. *Süleyman Demirel Üniversitesi Fen Bilimleri Enstitüsü Dergisi*, 21(2), 306-310.

Degeilh, R., & Marsh, R.E. (1959). A refinement of the crystal structure of diketopiperazine (2, 5-piperazinedione). *Acta Crystallographica*, 12(12), 1007-1014. doi: 10.1107/S0365110X59002845

Demir, L., & Godjaev, N. M. (2002). Conformational Analysis of Pol-Rfamide II (Glu^1-Trp^2-Leu^3-Lys^4-Gly^5-Arg^6-Phe^7-NH_2) Heptapeptide. *Turkish Journal of Chemistry*, 26(6), 825-832.

Dorset, D.L. (2010). Direct methods and refinement in electron and X-ray crystallography–diketopiperazine revisited. *Zeitschrift für Kristallographie International journal for structural, physical, and chemical aspects of crystalline materials*, 225(2-3), 86-93. doi: 10.1524/zkri.2010.1198

Frisch, M. J., Trucks, G. W., Schlegel, H. B., Scuseria, G. E., Robb, M. A., Cheeseman, J. R., Montgomery Jr., J. A., Vreven, T., Kudin, K. N., Burant, J. C., Millam, J. M., Iyengar, S. S., Tomasi, J., Barone, V., Mennucci, B., Cossi, M., Scalmani, G., Rega, N., Petersson, G.A., Nakatsuji, H., Hada, M., Ehara, M., Toyota, K., Fukuda, R., Hasegawa, J., Ishida, M., Nakajima, T., Honda, Y., Kitao, O., Nakai, H., Klene, M., Li, X., Knox, J.E., Hratchian, H.P., Cross, J.B., Bakken, V., Adamo, C., Jaramillo, J., Gomperts, R., Stratmann, R.E., Yazyev, O., Austin, A.J., Cammi, R., Pomelli, C., Ochterski, J.W., Ayala, P.Y., Morokuma, K., Voth, G.A., Salvador, P., Dannenberg, J.J., Zakrzewski, V.G., Dapprich, S., Daniels, A. D., Strain, M. C., Farkas, O., Malick, D. K., Rabuck, A. D., Raghavachari, K., Foresman, J. B., Ortiz, J. V., Cui, Q., Baboul, A. G., Clifford, S., Cioslowski, J., Stefanov, B. B., Liu, G., Liashenko, A., Piskorz, P., Komaromi, I., Martin, R.L., Fox, D. J., Keith, T., Al-Laham, M. A., Peng, C. Y., Nanayakkara, A., Challacombe, M., Gill, P. M. W., Johnson, B., Chen, W., Wong, M. W., Gonzalez, C., & Pople, J. A. (2004) .Gaussian 03, Revision C. 02, Gaussian, Inc., Wallingford CT.

Graz, C.J.M., Grant, G.D., Brauns, S.C., Hunt, A., Jamie, H., & Milne, P.J. (2000). Cyclic dipeptides in the induction of maturation for cancer therapy. *Journal of pharmacy and pharmacology*, 52(1), 75-82. doi: 10.1211/0022357001773535

Huang, R.M., Yi, X.X., Zhou, Y., Su, X., Peng, Y., & Gao, C.H. (2014). An update on 2, 5-diketopiperazines from marine organisms. *Marine Drugs*, 12(12), 6213-6235. doi: 10.3390/md12126213

Johnson, M., & Maggiora, G.M. (1990). *Concepts and Applications of Molecular Similarity*. New York, USA: John Wiley.

Karanam, G., Arumugam, M. K., & Natesh, N. S. (2020). Anticancer effect of marine sponge-associated Bacillus pumilus AMK1 derived dipeptide Cyclo (-Pro-Tyr) in human liver cancer cell line through apoptosis and G2/M phase arrest. *International Journal of Peptide Research and Therapeutics*, 26(1), 445-457. doi: 10.1007/s10989-019-09850-2

Kaur, K., Kaur, S., & Kapoor, V. K. (2020). Chemical synthesis and anti-inflammatory investigations of some cyclic peptide derivatives. *Plant Archives*, 20(2), 3531-3540.

Kilian, G., Davids, H., & Milne, P. J. (2013). Anticancer activity of the liposome-encapsulated cyclic dipeptides, cyclo (His-Gly) and cyclo (His-Ala). *Die Pharmazie-An International Journal of Pharmaceutical Sciences*, 68(3), 207-211. doi: 10.1691/ph.2013.2131

Lee, K.H., Kim, G.W., & Rhee, K.H. (2010). Identification of Streptomyces sp. KH29, which produces an antibiotic substance processing an inhibitory activity against multidrug-resistant Acinetobacter baumannii. *Journal of Microbiology and Biotechnology*, 20(12), 1672-1676. doi: 10.4014/jmb.1007.07035

Maksumov, I.S., Ismailova, L.I., & Godjaev, N.M. (1983). The program for semiempirical calculation of conformations of the molecular complexes. *Journal of Structural Chemistry (in Russian)*, 24, 147.

Mander, L., & Liu, H.W. (2010). *Comprehensive Natural Products* II: Chemistry and Biology. Oxford, UK: Elsevier.

Mendham, A. P., Dines, T. J., Snowden, M. J., Withnall, R., & Chowdhry, B. Z. (2009). IR/Raman spectroscopy and DFT calculations of cyclic di-amino acid peptides. Part III: Comparison of solid state and solution structures of cyclo (L-Ser-L-Ser). *Journal of Raman Spectroscopy*, 40(11), 1508-1520. doi: 10.1002/jrs.2306

Mills, I., Cvitas, T., Homann, K., Kallay, N., & Kuchitsu, K. (1988*). IUPAC-IUB Quantity. Units and Symbols in Physical Chemistry*. Oxford, UK: Blackwell Scientific Publications.

Milne, P.J., Hunt, A.L., Rostoll, K., Van Der Walt, J.J., & Graz, C.J.M. (1998). Medicinal chemistry: The biological activity of selected cyclic dipeptides. *Journal of Pharmacy and Pharmacology*, 50(12), 1331-1337. Doi: 10.1111/j.2042-7158.1998.tb03355.x

Mlynek, J., Bleha, T., & Tvaroska, I. (1980). Calculation of electrostatic interactions in torsional potential of the internucleotide phosphodiesteric unit. *Chemical Papers*, 34(1), 3-17.

Momany, F.A., McGuire, R.F., Burgess, A.W., & Scheraga, H.A. (1975). Energy parameters in polypeptides. VII. Geometric parameters, partial atomic charges, nonbonded interactions, hydrogen bond interactions, and intrinsic torsional potentials for the naturally occurring amino acids. *The Journal of Physical Chemistry*, 79(22), 2361-2381. doi: 10.1021/j100589a006

Ramachandran, G.N. (1968). Need for nonplanar peptide units in polypeptide chains. *Biopolymers: Original Research on Biomolecules*, 6(10), 1494-1496. doi: 10.1002/bip.1968.360061013

Ramachandran, G.N., Ramakrishnan, C., & Sasisekharan, V. (1963). Stereochemistry of polypeptide chain configurations. *Journal of Molecular Biology* 7, 95. doi: 10.1016/s0022-2836(63)80023-6.

Scott, R.A., & Scheraga, H.A. (1966). Conformational analysis of macromolecules. II. The rotational isomeric states of the normal hydrocarbons. *The Journal of Chemical Physics*, 44(8), 3054-3069. doi: 10.1063/1.1727180

Tong, W., Welsh, W.J., Shi, L., Fang, H., & Perkins, R. (2003). Structure-activity relationship approaches and applications. *Environmental Toxicology and Chemistry: An International Journal*, 22(8), 1680-1695. doi: 10.1897/01-198

Van der Merwe, E., Huang, D., Peterson, D., Kilian, G., Milne, P. J., Van de Venter, M., & Frost, C. (2008). The synthesis and anticancer activity of selected diketopiperazines. *Peptides*, 29(8), 1305-1311. doi: 10.1016/j.peptides.2008.03.010

Wang, Y., Wang, P., Ma, H., & Zhu, W. (2013). Developments around the bioactive diketopiperazines: a patent review. *Expert Opinion on Therapeutic Patents*, 23(11), 1415-1433. doi: 10.1517/13543776.2013.828036

Zhu, F., Liu, Z., & Chi, X. (2009). Anti-metastatic effect of repeated cyclic-GRGDSPA peptide produced by intein protein trans-spicing on murine B16 melanoma cell. *Chinese Journal of Lung Cancer*, 12, 665-667.

Yüzüncü Yıl Üniversitesi
Fen Bilimleri Enstitüsü Dergisi

http://dergipark.gov.tr/yyufbed

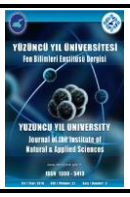

Araştırma Makalesi

Modülüs Fonksiyon Yardımı ile Tanımlanan İnvaryant Yakınsak Dizi Uzaylarının Topolojik Özellikleri

Hasan KARA[1], Dinçer ATASOY*[2]

[1]Iğdır Üniversitesi, Fen-Edebiyat Fakültesi, Matematik Bölümü, Iğdır, Türkiye
[2]Iğdır Üniversitesi, Iğdır Meslek Yüksekokulu, Finans-Bankacılık ve Sigortacılık Bölümü, Iğdır, Türkiye

Hasan KARA, ORCID No: 0000-0001-9828-9006, Dinçer ATASOY, ORCID No: 0000-0003-0389-1059
*Sorumlu yazar e-posta: dincer.atasoy@igdir.edu.tr

Makale Bilgileri

Geliş: 31.05.2021
Kabul: 28.06.2021
Yayınlanma Ağustos 2021
DOI: 10.53433/yyufbed.945323

Anahtar Kelimeler
Dizi uzaylarının topolojik özellikleri,
İnvaryant yakınsak dizi,
Modülüs fonsiyonu

Öz: Bu çalışmada Modülüs fonksiyon yardımı ile tanımlanan invaryant yakınsak dizi uzayları tanımlanarak aralarında bazı kapsam bağıntıları kuruldu. $[\omega_\sigma(f)], \overline{\omega}_\sigma(f)$ ve $\overline{\overline{\omega}}_\sigma(f)$ uzayları $[\omega_\sigma(f)(p)], \overline{\omega}_\sigma(f)(p)$ ve $\overline{\overline{\omega}}_\sigma(f)(p)$ uzaylarına genişletildi. Genelleştirilen bu dizi uzaylarının topolojik özellikleri incelendi.

Topological Properties of Invariant Convergent Sequences Defined with the Help of a Modulus Function

Article Info

Recieved: 31.05.2021
Accepted: 28.06.2021
Published August 2021
DOI: 10.53433/yyufbed.945323

Keywords
Topological properties of sequence spaces,
Invariant convergent sequence,
Modulus function

Abstract: In this study, invariant convergent sequence spaces defined with the help of the Modulus function were defined and some scope relations were established beyween them. Spaces of $[\omega_\sigma(f)], \overline{\omega}_\sigma(f)$ and $\overline{\overline{\omega}}_\sigma(f)$ is extended to $[\omega_\sigma(f)(p)], \overline{\omega}_\sigma(f)(p)$ and $\overline{\overline{\omega}}_\sigma(f)(p)$spaces. Topological properties of generalized sequence spaces are studied.

1. Giriş

Bu çalışmada modülüs fonksiyon yardımı ile tanımlanan invaryant yakınsak dizi uzayları tanımlanmıştır. $[\omega_\sigma(f)], \overline{\omega}_\sigma(f)$ ve $\overline{\overline{\omega}}_\sigma(f)$ uzayları $[\omega_\sigma(f)(p)], \overline{\omega}_\sigma(f)(p)$ ve $\overline{\overline{\omega}}_\sigma(f)(p)$ dizi uzaylarına genişletilmişir. Lorentz (1948), Savaş (2018), Rafeiro ve ark. (2018) ve Oğur (2020) tarafından çeşitli yönleri ile çalışmalar yapılmıştır. Bu çalışmalar kapsamında daha genel dizi uzaylarının bazı topolojik özellikleri incelenmiştir.

Tanım 1.

X bir lineer uzayı üzerinde bir $g: X \to \mathbb{R}$ bir fonksiyonu aşağıdaki özellikleri sağlıyorsa g fonksiyonuna X üzerinde bir paranorm ve $(X.g)'$ye de bir paranormlu uzay denir (Lorentz, 1948).

P1. $g(\theta) = 0$

P2. $g(x) = g(-x)$

P3. $g(x+y) \leq g(x) + g(y)$

P4. $\lambda \to \lambda_0,\ x \to x_0$ olması , $\lambda x \to \lambda_0 x_0$ olmasını gerektirir.

Tanım 2.

$P = (P_m)\ her\ m\ için\ P_m > 0$ ve $Sup\ P_m = H < \infty$ olacak şekilde reel sayılar dizisi olsun. Bu takdirde

$[\omega_\sigma(f)(p)] = \{x: \lim_k \frac{1}{k+1}\sum_{m=0}^{k} f|(t_{mn}(X-L)|^{P_m} = 0,\ n'ye\ göre\ düzgün\}$

$\overline{\omega}_\sigma(f)(p) = \{x: \sum_{n=0}^{\infty} f\left(\left|\Psi_{mn}(x) - t_{m-1,n}(x)\right|\right)^{P_m}),\ n'ye\ göre\ düzgün\ yakınsak\}$

$\overline{\overline{\omega}}_\sigma(f)(p) = \{x: \sup_n \sum_{m=0}^{\infty} f\left(\left|\Psi_{mn}(x) - \Psi_{m-1,n}(x)\right|^{P_m}\right) < \infty\}$ dur.

$\forall\ m\ için\ (P_m) = P$ olduğunda $\left[\omega_{\sigma p}(f)\right], \overline{\omega}_{\sigma p}(f)$ ve $\overline{\overline{\omega}}_{\sigma p}(f)$ uzaylarına eşit olur.

Ayrıca $\sigma_{(n)} = n+1$ olduğunda, bu uzaylar $[\omega_\sigma(f)], \overline{\omega}_\sigma(f)$ ve $\overline{\overline{\omega}}_\sigma(f)$ dizi uzaylarına indirgenir. (Sahoo, 1992).

Şimdi tanımlanan bu uzaylar ile ilgili özellikleri verelim.

Teorem 1.

$[\omega_\sigma(f)(p)], \overline{\omega}_\sigma(f)(p)$ ve $\overline{\overline{\omega}}_\sigma(f)(p)$ kümeleri $\mathbb{C}$ üzerinde lineer uzaylardır.

İspat.

$[\omega_\sigma(f)(p)], \overline{\omega}_\sigma(f)(p)$ ve $\overline{\overline{\omega}}_\sigma(f)(p)$ kümeleri $\mathbb{C}$ kümesinin alt kümeleridir.

$[\omega_\sigma(f)(p)]$ kümesinin $\mathbb{C}$ üzerinde lineer uzay olduğunu göstereceğiz. $\overline{\omega}_\sigma(f)(p)$ and $\overline{\overline{\omega}}_\sigma(f)(p)$ kümeleri de benzer şekilde lineer uzay oldukları gösterilebilir.

$x, y \in [\omega_\sigma(f)(p)]$ ve $\lambda, \mu \in \mathbb{C}$ için $|\lambda|^{P_m} \leq k_1 = \max(1, |\lambda|^H)$ ve $|\mu|^{P_m} = k_2 = \max(1, |\mu|^H)$ olmak üzere

$\left|X_{\sigma(n)} + Y_{\sigma(n)}\right|^{P_m} \leq k\ (\left|X_{\sigma(n)}\right|^{P_m} + \left|Y_{\sigma(n)}\right|^{P_m})$ olduğundan

$\frac{1}{k+1}\sum_{m=0}^{k} f|(t_{mn}(\lambda.x + \mu y)|^{P_m}) \leq k.k_1 \frac{1}{k+1} \sum_{m=0}^{k} f|(t_{mn}(x)|^{P_m}) + k.k_2 \frac{1}{k+1}\sum_{m=0}^{k} f|(t_{mn}(y)|^{P_m})$

elde edilir (Maddox, 1979).

$[\omega_\sigma(\mathrm{f})(\mathrm{p})] - lim = 0$ ve $x, y \in [\omega_\sigma(\mathrm{f})(\mathrm{p})]$ olduğundan $\lambda.x + \mu y \in [\omega_\sigma(\mathrm{f})(\mathrm{p})]$ sonucu elde edilir. Bu da $[\omega_\sigma(\mathrm{f})(\mathrm{p})]$ nin skaler çarpımla vektörel toplamlı bir lineer uzay olduğunu verir (Kara, 1994).

2. Materyal ve Yöntem

Teorem 2.

$P = (P_m)$ dizisi her m için $P_m > 0$, $SupP_m < \infty$ olsun. Bu takdirde

$[\omega_\sigma(\mathrm{f})(\mathrm{p})], M = \max(1, SupP_m)$ olmak üzere

$$g(f(x) = \operatorname*{Sup}_{\mathrm{k,\ n}}\left(\frac{1}{k+1}\sum_{\mathrm{m}=1}^{k}(|\mathrm{t_{mn}}f(\mathrm{x})|^{P_m})\right)^{\frac{1}{m}} \quad (1)$$

Fonksiyonu ile tam paranorumlu bir lineer topolojik uzaydır.

İspat.

Teoremin ispatı için g: $[\omega_\sigma(\mathrm{f})(\mathrm{p})] \to \mathbb{C}$ ye bir fonksiyon ve $\boldsymbol{x} \in [\omega_\sigma(\mathrm{f})(\mathrm{p})]$ için

$\operatorname*{Sup}_{\mathrm{k,n}}\left(\frac{1}{k+1}\sum_{\mathrm{m}=0}^{k}(|\mathrm{t_{mn}}f(\mathrm{x})|^{P_k})\right) < \infty$ olduğundan $g(f(x), \mathbb{C}$ de tanımlıdır. Şimdi paranorm şartlarını sağlatalım.

i) $g(f(0) = \operatorname*{Sup}_{\mathrm{k,n}}\left(\frac{1}{k+1}\sum_{\mathrm{m}=0}^{k}(|\mathrm{t_{mn}}f(0)|^{P_m})\right)^{\frac{1}{m}} = 0$ olur

ii) $g(f(-x) = \operatorname*{Sup}_{\mathrm{k,\ n}}\left(\frac{1}{k+1}\sum_{\mathrm{m}=0}^{k}(|\mathrm{t_{mn}}f(-\mathrm{x})|^{P_m})\right)^{\frac{1}{m}}$

$$= \operatorname*{Sup}_{\mathrm{k,n}}\left(\frac{1}{k+1}\sum_{\mathrm{m}=0}^{k}(|\mathrm{t_{mn}}f(-1.\mathrm{x})|^{P_m})\right)^{\frac{1}{m}}$$

$$= \operatorname*{Sup}_{\mathrm{k,\ n}}\left(\frac{1}{k+1}\sum_{\mathrm{m}=1}^{k}(|\mathrm{t_{mn}}f(|-1||\mathrm{x}|)|^{P_m})\right)^{\frac{1}{m}}$$

$$= \operatorname*{Sup}_{\mathrm{k,n}}\left(\frac{1}{k+1}\sum_{\mathrm{m}=1}^{k}(|\mathrm{t_{mn}}f(\mathrm{x})|^{P_m})\right)^{\frac{1}{m}}$$

$$= g(f(x)$$

olur (Mursaleen, 1983).

iii) $m \geq 1\ ve\ \forall\ m\ için\ \frac{P_m}{M} \leq 1$ olduğundan

$$g(f(x+y) = \operatorname*{Sup}_{\mathrm{k,n}}\left(\sum_{\mathrm{m}=0}^{k}(|\mathrm{t_{mn}}f(\mathrm{x}+\mathrm{y})|^{P_m})\right)^{\frac{1}{m}}$$

$$\leq \operatorname*{Sup}_{\mathrm{k,\ n}}\left(\frac{1}{k+1}\sum_{\mathrm{m}=0}^{k}\left(|\mathrm{t_{mn}}f(\mathrm{x}) + \mathrm{t_{mn}}f(\mathrm{y})\ |^{\frac{P_m}{M}})^m\right)\right)^{\frac{1}{m}}$$

$$\leq \operatorname{Sup}_{k,n}\left(\frac{1}{k+1}\sum_{m=0}^{k}\left(|t_{mn}f(x)|^{\frac{P_m}{M}}\right)^m\right)^{\frac{1}{m}} + \operatorname{Sup}_{k,\ n}\left(\frac{1}{k+1}\sum_{m=0}^{k}\left(|t_{mn}f(y)\ |^{\frac{P_m}{M}}\right)^m\right)^{\frac{1}{m}} \quad (2)$$

$$\leq \operatorname{Sup}_{k,n}\left(\frac{1}{k+1}\sum_{m=0}^{k}(|t_{mn}f(x)|^{P_k})\right)^{\frac{1}{m}} + \operatorname{Sup}_{k,\ n}\left(\frac{1}{k+1}\sum_{m=0}^{k}(|t_{mn}f(y)|^{P_k})\right)^{\frac{1}{m}}$$

$$= g(f(x) + g(f(y)$$

olur (Oğur, 2020).

Şimdi $[\omega_\sigma(f)(p)]$ deki skaler çarpımın sürekliliğini gösterelim. $P = (P_m)$ dizisi için $SupP_m < \infty$ olduğundan $P_m > \delta$ olacak şekilde bir $\delta > 0$ sayısı vardır.
Şimdi $|\lambda| \leq 1\ için\ |\lambda|^{P_m} \leq |\lambda|^{\delta}$ olduğundan

$$g(f(x) = \operatorname{Sup}_{k,n}\left(\frac{1}{k+1}\sum_{m=0}^{k}(|t_{mn}f(\lambda.x)|^{P_m})\right)^{\frac{1}{m}}$$

$$\leq |\lambda|^{\frac{\delta}{m}}.g(f(x)$$

olur. Böylece $\lambda \to 0,\ \ x \to 0\ \ ise\ \lambda x \to 0$ ve eğer $\lambda\ sabit\ ve\ \ x \to 0\ \ ise\ \lambda x \to 0$ dir.

$x\ \in [\omega_\sigma(f)(p)]$ sabit ve verilen $\varepsilon > 0\ \ için\ \exists\ k_0$ sayısı vardır ki $\forall\ n\ için$

$$\operatorname{Sup}_{k\geq k_0}\left(\frac{1}{k+1}\sum_{m=0}^{k}(|t_{mn}f(\lambda.x)|^{P_m})\right)^{\frac{1}{m}} < \frac{\varepsilon}{2} \quad (3)$$

ve $|\lambda| < \delta$ olacak şekilde $\delta > 0$ sayısı bulabiliriz (Nakano, 1953).

dolayısıyla $\forall\ n\ için$

$$\operatorname{Sup}_{k\leq k_0}\left(\frac{1}{k+1}\sum_{m=0}^{k}(|t_{mn}f(\lambda.x)|^{P_m})\right)^{\frac{1}{m}} < \frac{\varepsilon}{2} \quad (4)$$

olur. Böylece (3) ve (4) ifadelerinden $|\lambda| < \delta$ oldukça $g\big(f(\lambda.x)\big) < \varepsilon$ elde ederiz ki bu da ispatı tamamlar (Savaş, 2018).

3. Bulgular

$[\omega_\sigma(f)(p)]$ uzayının $g\ paranormuna$ göre tam olduğu görülecektir.

$(x^s)\ nin\ [\omega_\sigma(f)(p)]\ de$ bir Cauchy dizisi olsun. Yani

$s,t \to \infty\ iken\ g(f(x^s - x^t) \to 0$ olsun.

$$g(f(x^s - x^t) = \operatorname{Sup}_{k,n}\left(\frac{1}{k+1}\sum_{m=0}^{k}(|t_{mn}f(x^s - x^t)|^{P_m})\right)^{\frac{1}{m}}$$

ve

$$g(f(x^s - x^t) \geq \operatorname{Sup}_{k,n}\left(\frac{1}{k+1}\sum_{m=0}^{k}(|t_{mn}f(x^s - x^t)|^{P_m})\right)^{\frac{1}{m}} \quad (5)$$

olduğundan $\forall\ m\ ve\ n\ için$

$$\lim_{s,t\to\infty} |t_{mn}f(x^s - x^t)|^{P_m} = 0$$

elde edilir. Özel olarak m=0 olmak üzere herhangi n için $s,t \to \infty\ iken$

$|\mathrm{t}_{\mathrm{mn}} f(x^s - x^t)| = f(|x^s - x^t|) = |x^s - x^t| \to 0$ dır. Böylece $(x^s), \mathbb{C}$ de bir Cauchy dizisidir.

$\mathbb{C}$ tam olduğundan dolayı $s \to \infty \, iken \, x^s \to x$ olacak şekilde $x \in \mathbb{C}$ vardır. (5) numaralı ifadeden $\varepsilon > 0 \;\; ve \; \exists \, \mathbb{N}$ öyleki $s, t > \mathbb{N}$ için

$$\left(\frac{1}{k+1}\sum_{\mathrm{m}=0}^{k}(|\mathrm{t}_{\mathrm{mn}} f(x^s - x^t)|^{P_m})\right)^{\frac{1}{m}} < \varepsilon \qquad (6)$$

olur.

Şimdi $s > \mathbb{N}$ ve $t \to \infty$ olsun. Bu takdirde (6) numaralı ifadeden

$\left(\frac{1}{k+1}\sum_{\mathrm{m}=0}^{k}(|\mathrm{t}_{\mathrm{mn}} f(x^s - x^t)|^{P_m})\right)^{\frac{1}{m}} < \varepsilon$ elde edilir. Buradan da

$\delta \to \infty \, iken \, g(f(x^s - x^t) \to \infty$ olur.

Bu da $x^s \to x' \, e$ yakınsaması demektir (Mursaleen, 1983).
(6) numaralı ifadeden ve her bir s için $x^s \in [\omega_\sigma(\mathrm{f})(\mathrm{p})] \; ve \; [\omega_\sigma(\mathrm{f})(\mathrm{p})]$ nin lineer olduğundan $g\big(f(x)\big) = g(f(x^s - x^t + x) \leq g(f(x^s - x) + g(f(x)) \to 0$ elde edilir. Buradan $x \in [\omega_\sigma(\mathrm{f})(\mathrm{p})]$ olduğu elde edilir. Böylece $[\omega_\sigma(\mathrm{f})(\mathrm{p})]$ nin tam olduğu görülür (Rafeiro ve ark, 2018).
Bu teoremde $p \, sabit \, ve \, p \geq 1 \, ise \; [\omega_\sigma(\mathrm{f})(\mathrm{p})]$ uzayı Banach uzayı $0 < p < 1$ ise p- normlu uzaya indirgenir (Sahoo, 1992).

4. Tartışma ve Sonuç

Teorem 3.

$P = (P_m)$ dizisi her m için $P_m > 0, \; SupP_m < \infty$ olsun. Bu takdirde

$\bar{\omega}_\sigma(\mathrm{f})(\mathrm{p}) \; ve \; \bar{\bar{\omega}}_\sigma(\mathrm{f})(\mathrm{p})$ uzayları $M = \max(1, \;\; SupP_m)$ olmak üzere

$g(f(x) = \underset{\mathrm{n}}{\mathrm{Sup}}\left(\sum_{\mathrm{m}=0}^{\infty} f\left(\left|\Psi_{\mathrm{mn}} - \Psi_{\mathrm{m}-1,\mathrm{n}}\right|^{P_m}\right)\right)^{\frac{1}{m}}$ fonksiyonu altında bir tam paranormlu lineer topolojik uzaydır.

Teoremin ispatı teorem 2'nin ispatının benzeri olduğundan tekrar vermeyeceğiz.

Teorem 4.

a) Eğer $\forall \, m \, için \, p_m \leq q_m \;\; ise \; \bar{\omega}_\sigma(\mathrm{f})(\mathrm{p}) \subset \bar{\omega}_\sigma(\mathrm{f})(\mathrm{q})$ ve $\bar{\bar{\omega}}_\sigma(\mathrm{f})(\mathrm{p}) \subset \bar{\bar{\omega}}_\sigma(\mathrm{f})(\mathrm{q})$ dur.
b) Eğer $p \, sabit \, ve \, p \geq 1 \, ise$

$l_p^\sigma(f)_p \subset \bar{\omega}_\sigma(\mathrm{f})_p \; ve \;\; l_\sigma^{\sigma\sigma}(f)_p \subset \bar{\bar{\omega}}_\sigma(\mathrm{f})_p$ dir.

İspat.

a) $\bar{\omega}_\sigma(\mathrm{f})(\mathrm{p}) \subset \bar{\omega}_\sigma(\mathrm{f})(\mathrm{q})$ göstereceğiz $\bar{\bar{\omega}}_\sigma(\mathrm{f})(\mathrm{p}) \subset \bar{\bar{\omega}}_\sigma(\mathrm{f})(\mathrm{q})$ olduğu benzer şekilde gösterilir.

$x \in \bar{\omega}_\sigma(\mathrm{f})(\mathrm{p})$ olsun. Bu takdirde

$\sum_{\mathrm{m}=\mathrm{M}}^{\infty} f\left(\left|\Psi_{\mathrm{mn}}(x) - \Psi_{\mathrm{m}-1,\mathrm{n}}(x)\right|^{P_m}\right) < 1$

olacak şekilde M tamsayısı vardır. Böylece $\forall \, n \; ve \;\; m \geq M$ için $f\left(\left|\Psi_{\mathrm{mn}}(x) - \Psi_{\mathrm{m}-1,\mathrm{n}}(x)\right|^{P_m}\right) < 1$ olup $p_m \leq q_m$ olduğundan da $f\left(\left|\Psi_{\mathrm{mn}}(x) - \Psi_{\mathrm{m}-1,\mathrm{n}}(x)\right|^{q_m}\right) < f\left(\left|\Psi_{\mathrm{mn}}(x) - \Psi_{\mathrm{m}-1,\mathrm{n}}(x)\right|^{P_m}\right)$

yazılır. Bu eşitliğin her iki tarafının m üzerinden toplamı alınırsa

$\sum_{m=M}^{\infty} f\left(\left|\Psi_{mn}(x)-\Psi_{m-1,n}(x)\right|^{q_m}\right) \leq \sum_{m=M}^{\infty} f\left(\left|\Psi_{mn}(x)-\Psi_{m-1,n}(x)\right|^{P_m}\right)$ elde edilir. Sağdaki seri n ye göre düzgün yakınsak olduğundan, soldaki seri de n ye göre düzgün yakınsak olur. O halde

$\bar{\omega}_{\sigma}(f)(p) \subset \bar{\omega}_{\sigma}(f)(q)$ dur.

b) $l_p^{\sigma}(f)_p \subset \bar{\omega}_{\sigma}(f)_p$ ispatını yapacağız. $l_{\sigma}^{\sigma\sigma}(p) \subset \bar{\bar{\omega}}_{\sigma}(f)_p$ olduğu da benzer şekilde gösterilir.b)

$x \in l_p^{\sigma}(f)_p \; olsun \; p=1$ iken ifade açıktır. $p>1$ için

$$f\left(\left|\Psi_{kn}(x)-\Psi_{k-1,n}(x)\right|^{p}\right) \leq \frac{1}{k(k+1)^p}\sum_{m=1}^{\infty} m^p f\left(\left|t_{mn}(x)-t_{m-1,n}(x)\right|^{p}\right)$$

$$\leq \sum_{m=1}^{\infty} m^p f\left(\left|t_{mn}(x)-t_{m-1,n}(x)\right|^{p}\right)\sum_{k=m}^{\infty}\frac{1}{k(k+1)^p}$$

$$\leq \sum_{k=m}^{\infty} m^p f\left(\left|t_{mn}(x)-t_{m-1,n}(x)\right|^{p}\right) \qquad (7)$$

elde edilir. (II) yakınsak olduğundan $\sum_{m=1}^{\infty} f\left(\left|\Psi_{mn}(x)-\Psi_{m-1,n}(x)\right|^{p}\right)$ düzgün yakınsaktır. O halde $l_p^{\sigma}(f)_p \subset \bar{\omega}_{\sigma}(f)_p$ olur (Savaş, 2018).

Sonuç olarak modülüs fonksiyon yardımı ile tanımlanan invaryant yakınsak dizi uzayları tanımlanarak bazı kapsamlar kurulmuştur.

$[\omega_{\sigma}(f)], \bar{\omega}_{\sigma}(f)$ ve $\bar{\bar{\omega}}_{\sigma}(f)$ uzayları $[\omega_{\sigma}(f)(p)], \bar{\omega}_{\sigma}(f)(p)$ ve $\bar{\bar{\omega}}_{\sigma}(f)(p)$ uzaylarına genişletilerek genel dizi uzaylarının topolojik özellikleri incelenmiştir.

Kaynakça

Kara, H. (1994). *İnvaryant yakınsaklık yardımıyla tanımlanan dizi uzayları*. (Doktora Tezi), Yüzüncü Yıl Üniversitesi, Fen Bilimleri Enstitüsü, Van, Türkiye.

Lorentz, G. (1948). A contribution to the theory of divergent secunces. *Acta Mathematica.* 80, 167-190. doi: 10.1007/BF02393644.

Maddox, I. J. (1979). On strong alost convergence. *Mathematical Proceedings of the Cambridge Philosophical Society*. 85, 345-350. doi:10. 1017/S0305004100054281.

Mursaleen, M. (1983). On some new invariant matrix methods of summability. *Quarterly Journal of Mathematics*, 34, 77. doi:10.1093/qmath/34.1.77.

Nakano, H. (1953). Concave modulars. *Journal of the Mathematical Society of Japan*, S:29-49. doi:10.2969/jmsj/00510029.

Oğur, O. (2020). Modülüs fonksiyonu ile tanımlanmış genelleştirilmiş büyük lebesgue dizi uzaylarının topolojik bazı özellikleri. *Gümüşhane Üniversitesi Fen Bilimleri Enstitüsü Dergisi 10 (4),* 1148-1149. doı: 10.17714/gumusfenbil.732116.

Rafeiro, H., Samkho, S. & Umarkhadzhiev, S. (2018). Grand lebesgue sequence spaces. *Georgian Mathematical Journal*, 19(2), 235-246. doi:org/10.1515/gmj-2018-0017.

Sahoo, G. D. (1992). On some squence spaces. *Journal of Mathematical Analysis and Aplications 164, 381-398.* doi:10.1016/0022-247X(92)90122-T.

Savaş, E. (2018). On some new sequence spaces. J*ournal of the Institute of Science and Technology of Balıkesir University*. *Special Issue, 20(3)*. 155-156. doi: 10.25092/baunfbed.487747.

Yüzüncü Yıl Üniversitesi
Fen Bilimleri Enstitüsü Dergisi

http://dergipark.gov.tr/yyufbed

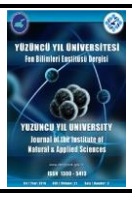

Research Article

A Bayesian Approach to Binary Logistic Regression Model with Application to OECD Data

Asuman YILMAZ*[1], Eray ÇELİK[1]

[1]Van Yüzüncü Yıl University, Faculty of Economics and Administrative Sciences, Department of Econometrics, 65080, Van, TURKEY

Asuman YILMAZ, ORCID No:000-0002-8653-6900, Eray ÇELİK, ORCID No0000-0001-7490-8124,
*Sorumlu yazar e-posta: asumanduva@yyu.edu.tr

Article Info

Recieved: 08.12.2020
Accepted: 07.07.2021
Published August 2021
DOI:10.53433/yyufbed.837533

Keywords
Binary-Logistic regression,
Maximum likelihood,
Bayesian method

Abstract: In spite of being a common method for estimating the model parameters, Maximum Likelihood (ML) method may give bias results for small sample sizes. To overcome this problem, Bayesian method is usually utilized to obtain the estimates of the model parameters as an alternative to the ML method. In this study, a real data set was analyzed by using the binary logistic regression model. Parameters of the binary logistic regression model were estimated by using ML and Bayesian methods. Modeling performance of the binary logistics regression model based on the Bayesian estimates was compared with the model based on the ML estimates. Well-known information criteria such as AIC and BIC were used in this comparison.

İki Durumlu Lojistik Regresyon Modeline Bayesci Bir Yaklaşım: OECD Örneği

Makale Bilgileri

Geliş: 08.12.2020
Kabul: 07.07.2021
Yayınlanma Ağustos 2021
DOI:10.53433/yyufbed.837533

AnahtarKelimeler
İki durumlu lojistik regresyon,
En çok olabilirlik yöntemi,
Bayesci Metot

Öz: En çok olabilirlik metodu model parametrelerini tahmin etmek için yaygın bir yöntem olmasına rağmen, küçük örneklem büyüklükleri için yanlı sonuçlar verebilir. Bu problemin üstesinden gelmek için, en çok olabilirlik yöntemine alternatif olarak model parametrelerinin tahmininde genellikle Bayes yöntemi kullanılmaktadır. Bu çalışmada, iki durumlu lojistik regresyon modeli kullanılarak gerçek bir veri seti analiz edilmiştir. İki durumlu lojistik regresyon modelinin parametreleri, en çok olabilirlik ve Bayesci yöntemler kullanılarak tahmin edilmiş, elde edilen sonuçlar Akaike bilgi kriteri (AIC) ve Bayesci bilgi kriteri (BIC) gibi kriterler kullanılarak karşılaştırılmıştır.

1. Introduction

Generalized linear models (GLM) are widely-used to define relationship between dependent and independent variables. The GLM is differed basing on the utilized function in defining the relationship between dependent and independent variables. For example, GLM becomes binary logistic regression model when dependent variable is binary and logarithmic function is utilized in defining the relationship between dependent and independent variables (Hair et al.,2006; Agresti & Hitchcock, 2005). In spite of being a common method for estimating the model parameters, Maximum Likelihood (ML) method may give bias results for small sample sizes. To overcome this problem, Bayesian method

usually considered in obtaining the estimates of the model parameters as an alternative to the ML method (Griffiths, 1973; Tektaş & Günay, 2008).

There exist many studies considering the Bayesian method in estimation procedure of the model parameters. For example, Albert & Chib, 1993 proposed a new algorithm by using the latent variables. Groenewald & Mokgatlhe, 2005 used a method suggested by Albert & Chib, 1993 to obtain a sample by using coefficients of posterior distribution through Gibbs sampling. Zelner & Rossi, 1984 considered numeric integration method and Monte Carlo integration method to obtain the posterior distribution of the model parameters in small and large sample sizes, respectively. Rashwan & El Dereny, 2012 used logistic regression model in analyzing the prostate cancer data in which Bayesian methods were used for obtaining the estimates of the model parameters. Ghosh &Mitra, 2017 investigated Bayesian logistic regression under different Cauchy prior distributions. Huggins et al., 2017 developed an efficient coreset construction algorithm for Bayesian logistic regression models. Spyroglou, et al., 2018 used Bayesian logistic regression method in analyzing the asthma persistence prediction. Dagliati, et al., 2017 proposed hierarchical Bayesian logistic regression to forecast metabolic control in type 2 DM patients. Lukman et al., 2021 used Bayesian logistic regression to analyze the hypothyroid prediction in post-radiation nasopharyngeal cancer patients. Suleiman et al., 2019 used Bayesian logistic regression approaches to predict incorrect DRG assignment.

In this study, Organization for Economic Cooperation and Development (OECD) data were analyzed via binary logistic regression model. Estimates of the model parameters were obtained using ML and Bayesian methods. Modeling performance of the model based on the Bayesian estimates was compared with the model based on the ML estimates. In this comparison, well-known information criteria Akaike Information Criterion (AIC) and Bayesian Information Criterion (BIC) were used.

The rest of the paper as follows: in section 2, binary logistic regression model is briefly introduced. ML method and Bayesian method are given in section 3. In the application part, a real data set from OECD is analyzed by using the binary logistic regression model. Here, estimates of the model parameters are obtained via the ML and the Bayesian methods. Finally, section 5 is reserved for the conclusion.

2. Materials and Methods

In this section, information for the binary logistic regression, model the ML and the Bayesian methods are given briefly.

2.1. Binary logistic regression model

In binary logistic regression, dependent variable y follows a Bernoulli distribution since assumed that it takes only values 0 and 1. Here, the probability of occurrence of an event is denotes by $P\left(y_i=1\right)=\pi_i$ and probability of non-occurrence of an event is denotes by $P\left(y_i=0\right)=1-\pi_i$. If n observations are obtained for the dependent variable, i.e. $y_i\left(i=1,2,...n\right)$ binary logistic regression model can be expressed as follows:

$$\begin{aligned} & y_i \mid \pi_i: \ \ Bernoulli\left(\pi_i\right), \\ & \pi_i=P\left(y_i=1\right)=\frac{\exp(x_i^{'}\beta)}{1+\exp(x_i^{'}\beta)}, \ \ i=1,2,...,n, \end{aligned} \tag{1}$$

where $y_i=1$ if the interest response is observed for the *i-th* individual and $y_i=0$ otherwise. $\beta=\left[\beta_0\ \beta_1\ \beta_2...\beta_j\right]^{'}$ is the vector of an unknown model parameters and $x=\left[1\,x_{i1}...x_{ij}\right]^{'}$ is the vector of measurements of the *i-th* individual for the *j-th* independent variable.

2.2. ML method

The likelihood function (L) in binary logistic regression can be expressed as follows:

$$L\left(\underset{\vdots}{\beta}; \underset{\vdots}{y}, \underset{\vdots}{x}\right) = \prod_{i=1}^{n}\left[\frac{\exp\left(x_i'\beta\right)}{1+\exp\left(x_i'\beta\right)}\right]^{y_i}\left[\frac{1}{1+\exp\left(x_i'\beta\right)}\right]^{1-y_i}. \quad (2)$$

The log-likelihood equations are the first derivation of the logarithm of the likelihood function (log L) with the parameter of the interest as given below.

$$\frac{\partial \log L}{\partial \beta_j} = \sum_{i=1}^{n} x_{ij}\left(y_i - \frac{\exp\left(\sum_{k=0}^{K} x_{ik}\beta_k\right)}{1+\exp\left(\sum_{k=0}^{K} x_{ik}\beta_k\right)}\right) = 0, \quad j = 1,2,...,p. \quad (3)$$

The ML estimates of the model parameters are the simultaneous solutions of the log L equations given in Equation (3). Here, Newton-Raphson method is utilized to obtain the simultaneous solutions of these equations.

2.3. Bayesian method

ML methodology usually needs large sample size to obtain accurate estimates of the parameters. However, in some science fields such as medicine and agriculture small sample size is commonly encountered. Unlike the ML methodology, the Bayesian methodology does not need large sample size, i.e. it has not limitations regarding the size of sample. This is why the Bayesian methodology is an alternative for the ML methodology (Acquah, 2013; Tektaş & Günay 2008; Santos, 2009).
In the Bayesian methodology, there are three key parts in estimation procedure. These are (i) the prior distribution, (ii) the likelihood function, and (iii) posterior distribution. The posterior distribution is written as follows:

$$posterior\ \ distribution = \left(\ prior\ \ distribution\ \right)\left(likelihood\ \ \ function\right). \quad (4)$$

Here, prior distribution summarizes the information obtained from other sources. There are two types of prior distribution, namely, informative and non-informative prior distribution, (Acquah, 2013). In this study, we assume a normal prior on β_k.

$$\beta_k \sim N\left(0,10000\right),\ k = 1,2,...j. \quad (5)$$

The above expression is equivalent to non-informative priors of these parameters.

The likelihood function involves the information about the sample. The posterior distribution contains all the available knowledge for the model parameters. From (4), the posterior distribution is obtained by multiplying the prior distribution in (5) by the likelihood function in (3) as given below:

$$p\left(\beta; y, x\right) = \prod_{i=1}^{n}\left[\frac{\exp\left(x_i'\beta\right)}{1+\exp\left(x_i'\beta\right)}\right]^{y_i}\left[\frac{1}{1+\exp\left(x_i'\beta\right)}\right]^{1-y_i}\prod_{i=1}^{n}\frac{1}{\sigma_k\sqrt{2\pi}}\exp\left[-\frac{1}{2}\left(\frac{\beta_k-\mu_k}{\sigma_k}\right)^2\right]. \quad (6)$$

Equation (6) represents the posterior probability density function of the model parameters, and analytical solution for it cannot be obtained explicitly. The computational difficulties in obtaining the posterior distribution are disadvantage of the Bayesian method; however this problem can be solved by using the Markov Chain Monte Carlo (MCMC) simulation technique. The aim of the MCMC is to create a stationary Markov process to obtain the statistical inference for the posterior distribution. Therefore, the Markov Chain Monte Carlo (MCMC) simulation method is widely-used for getting statistical inference about the posterior distribution (Acquah, 2013).

Using the MCMC in complicated statistical problems brings some problems such as not converge to the desirable posterior distribution and determination of iteration size to obtain the stationary Markov process. The convergence to posterior distribution is necessary in the Bayesian methodology to obtain the accurate estimates of the model parameters. See (Geyer, 1992) for detailed information for the methods provides convergence in this context.

3. Results

In this section a real data set was analyzed using the binary logistic regression model. The estimates of the model parameters were obtained via the ML and the Bayesian methods. The data set includes various demographic and economic data from 34 countries which were member of the OECD. The data set was obtained from the official website of the OECD.
Following binary logistic regression model given in Equation (7) is used to analyze the data set:

$$\log\left(\frac{\pi_i}{1-\pi_i}\right) = \beta_0 + \beta_1 x_1 + \beta_2 x_2 + \beta_3 x_3 + \beta_4 x_4 + \beta_5 x_5 + \beta_6 x_6 + \beta_7 x_7 + \beta_8 x_8 + \varepsilon,\ i = 1, 2, \ldots 34 \qquad (7)$$

Here, dependent variable is European Union (EU) membership (member:1, not member:0) and independent variables $(x_1, x_2, ..., x_8)$ are total number of people living, ratio of female parliamentarians, participation level of women between the ages 15 and 64 to labor force, ratio of imports, ratio of exports, life satisfaction or satisfaction with life, share allocated for health expenditure from the gross domestic product, average number of children per women between the ages 15 and 49 in each OECD country in 2013, respectively.

The estimates of the model parameters, given in Equation (7), were obtained by using the ML and the Bayesian methods and the analyses are conducted through R 3.0.3 software program. The ML estimates of the model parameters, standard errors (SEs), test statistics (z), and significant values (*p)* with corresponding to parameter estimates are given in Table 1.

Table 1. The statistics obtained with ML estimators

Variables	$\hat{\beta}_{ML}$	Exp($\hat{\beta}_{ML}$)	SE	z	*p*
Intercept	10.0493	23.139	7.57530	1.327	0.088
x_1	0.38593	1.470	0.23629	1.633	0.066
x_2	-0.06910	0.933	0.15646	-0.442	0.687
x_3	0.08177	1.085	0.08394	0.974	0.413
x_4	0.20735	1.230	0.16268	1.275	0.290
x_5	-5.69552	0.003	3.24655	-1.754	0.031
x_6	1.55750	4.746	1.05062	1.482	0.405
x_7	0.04387	1.044	0.02705	1.622	0.140
x_8	-0.80534	0.446	2.87410	-0.280	0.644

It can be seen from Table 1 that all parameter estimates for the independent variables, except x_5, are not statistically significant, since p values are greater than 0.05.

The Bayesian estimates of the model parameters along with the standard deviations (SDs), Monte Carlo simulation errors (MC Error), and confidence interval (CI) between (%2.5-%97.5) of the parameter estimates are given in Table 2.

Table 2. The statistics obtained with Bayesian estimators

Variables	Mean	Exp(Mean)	SD	MC Error	CI
Intercept	11.90223	147.72	0.72646	0.02462	(-3.11615, 29.9593)
x_1	0.05229	1.053	0.00162	0.00067	(0.01377, 0.09980)
x_2	0.41872	1.520	0.15591	0.00421	(0.11763,0.78240)
x_3	0.05399	1.055	0.16803	0.00517	(-0.25042, 0.41285)
x_4	0.15183	1.163	0.09890	0.00257	(-0.00556, 0.37750)
x_5	0.16783	1.182	0.09245	0.00220	(-0.01837, 0.33160)
x_6	-6.84683	0.001	2.60164	0.06542	(-12.94350, -2.45507)
x_7	1.42337	4.151	0.03344	0.01588	(0.09428, 2.68094)
x_8	0.42022	1.522	3.54912	0.09246	(-0.89632, 5.20511)

It can be seen from Table 2 that parameter estimates for the independent x_1, x_2, x_6 and x_7 are statistically significant at 0.05 significance level, i.e. CI between (%2.5-%97.5) of these parameter estimates not include the value 0.

According to Table 2, the ratio of the population of the OECD countries which are the member of EU to the non-member countries is 1.05. The ratio of women's participation in parliament in the OECD countries which are the member of EU to the non-member countries is 1.52. The ratio of life satisfaction of those who live in the OECD countries which are the member of EU to the non-member countries is 0.001. The ratio of health expenditures of the OECD countries which are member of EU to non-member countries is 4.52.

Burn-in procedure is applied to the first 1000 iterations in the Markov Chain for providing convergence to the posterior distribution. Autocorrelation plots, trace plots and Geweke convergence test results are also utilized to guaranteed convergence for the posterior distribution; see, Figure 1, Figure 2 and Table 3, respectively.

Autocorrelations given in Figure 1 measure the dependence between each sample value in the Markov Chain. Low correlation means that the convergence has been achieved; see (Cowles & Carlin, 1996).

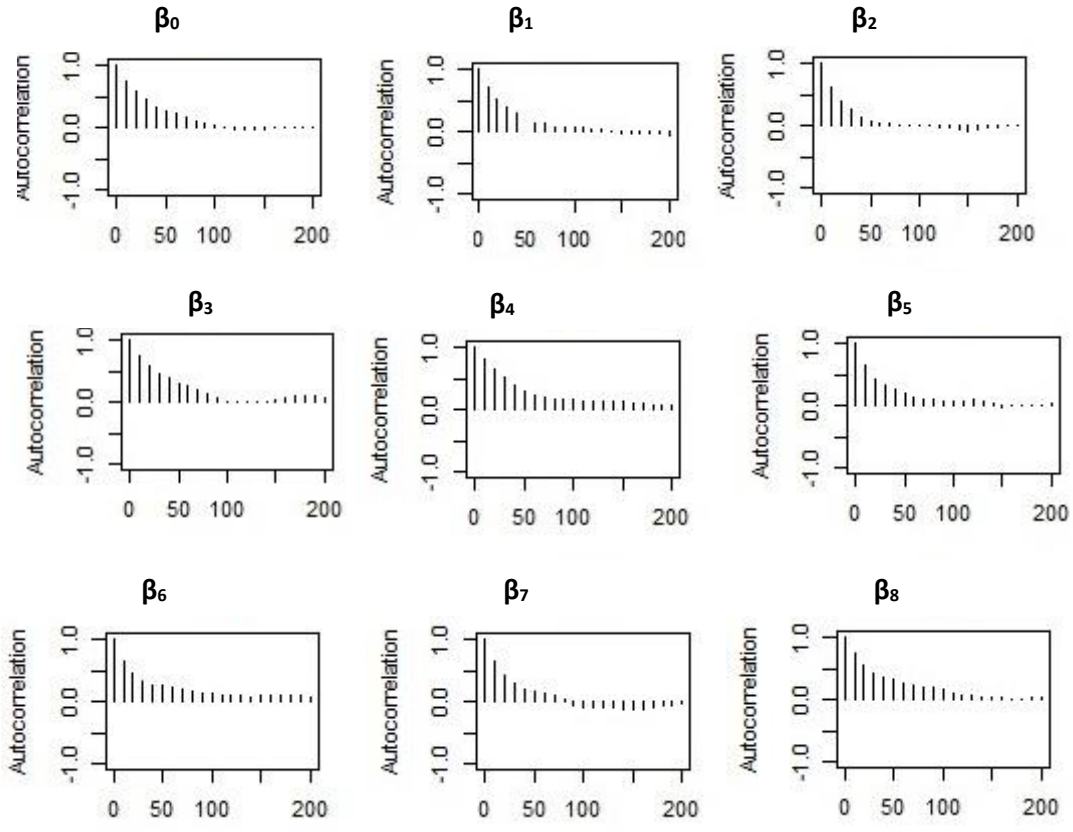

Figure 1. Autocorrelation plots within each parameter logit model

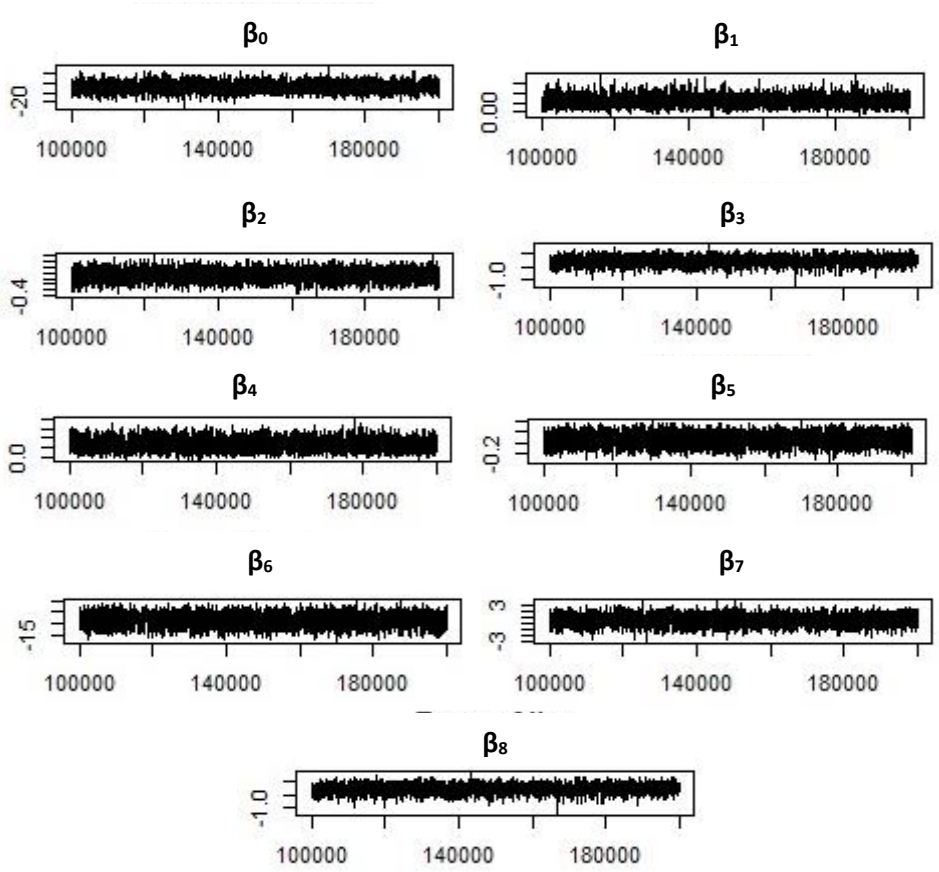

Figure 2. The traceplots within each parameter logit model

From Figure 2, it also can be said that convergence has been achieved for each parameter of the corresponding variables.

Table 3. Geweke convergence test results

Variables:	Intercept	x_1	x_2	x_3	x_4	x_5	x_6	x_7	x_8
z statistics:	0.693	-1.340	1.019	-1.755	0.317	0.362	0.019	-0.071	-0.990

In this study all tests were conducted under %95 confident intervals that mean critical values of test statistics is ± 1.96. It can be seen from Table 3 that Geweke test statistics for all parameters with corresponding variable is between ± 1.96 which shows the convergence has been achieved for each parameter.

4. Discussion and Conclusion

In this study, a short literature review for Bayesian logistic regression is presented. Also, the estimates of the model parameters are derived by using maximum likelihood estimation and Bayesian estimation methods. Moreover, the real data set is analyzed at for better understanding of the methods presented. This data set taken from the OECD is modeled by using the binary logistic regression model. In the estimation procedure of the model parameters, the ML and the Bayesian methods are used. In Bayesian methods, burn-in procedure is applied to the first 1000 iterations in the Markov Chain for providing convergence to the posterior distribution. Also, autocorrelation plots, trace plots and Geweke convergence test results are utilized to guaranteed convergence for the posterior distribution. It can be seen from all convergence tests that convergence was provided for each parameter. Then, the modeling performances of these two models are compared by using the well-known information criteria such as AIC and BIC given in Table (4). Also, Mc Fadden R^2 and correct classification ratio values for each model are given in Table (4). It should be noticed that smaller values of the Mc Fadden R^2, AIC and BIC are mean better fitting.

Table 4. Goodness of fit results

Criteria	Correct Classification Ratio	Mc Fadden R^2	AIC	BIC
Model based on ML estimates	89.70	0.66	38.44	51.91
Model based on Bayes estimates	94.20	0.53	32.74	46.21

According to Table (4), it can be concluded that binary logistic regression model based on the Bayesian estimates has higher correct classification ratio and smaller Mc Fadden R^2, AIC, and BIC values than the based on the ML estimates. The differences between ML and Bayesian estimates are occurred by the small sample size. Results show that for small sample size, as similar in application of this study, the Bayesian method shows better performance than the ML method based on the goodness of fit statistics given in Table (4). In this regard, it is seen that the Bayesian method is more preferable than the ML method for this data set.

References

Acquah, H. D. (2013). Bayesian logistic regression modelling via Markov chain Monte Carlo algorithm. *Journal of Social and Development Sciences*, 4, 193-197. doi: 10.22610/jsds.v4i4.751

Agresti, A., & Hitchcock, D. B. (2005). Bayesian inference for categorical data analysis. *Statistical Methodsand Applications*, *14*(3), 297-330. doi:10.1007/s10260-005-0121-y

Albert, J. H., & Chib. S. (1993). Bayesian analysis of binary and polychotomous response data. *Journal of the American Statistical Association*, 88, 669-679. doi:10.2307/2290350

Cowles, M. K., & Carlin, B. P. (1996). Markov chain Monte Carlo convergence diagnostics: a comparative review. *Journal of the American Statistical Association*, *91*, 883-904.

Dagliati, A., Malovini, A., Decata, P., Cogni, G., Teliti, M., Sacchi, L., & Bellazzi, R. (2016). Hierarchical Bayesian Logistic Regression to forecast metabolic control in type 2 DM patients. In *AMIA Annual Symposium Proceedings*,2016, 470-479.

Dos Santos, M. A., Moala, F. A., & Tachibana, V. M. (2009). Approximate Bayesian methods for logistic regression model. *Revista Brasileira de Biometria*, 27, 288-300.

Geyer, C. J. (1992). Practical markov chain montecarlo. *Statistical Science*, 10, 473-483.

Ghosh, J., Li, Y., & Mitra, R. (2018). On the use of Cauchy prior distributions for Bayesian logistic regression. *Bayesian Analysis*, *13*, 359-383. doi:10.1214/17-BA1051

Griffiths, D. A. (1973). Maximum likelihood estimation for the beta-binomial distribution and an application to the household distribution of the total number of cases of a disease, *Biometrics, 7*,637-648.

Groenewald, P. C., & Mokgatlhe, L. (2005). Bayesian computation for logistic regression. *Computational Statistics & Data Analysis*, 48, 857-868. doi:10.1016/j.csda.2004.04.009

Hair, F. T., William, C. B., Babin, B. T., & Anderson E. R. (2006). *Overview of Multivariate Methods*. Oxford, UK: Wiley & Sons.

Huggins, J. H., Campbell, T., & Broderick, T. (2016). Coresets for scalable bayesian logistic regression. *arXiv preprint arXiv:1605.06423*.

Lukman, P. A., Abdullah, S., & Rachman, A. (2021). Bayesian logistic regression and its application for hypothyroid prediction in post-radiation nasopharyngeal cancer patients. *In Journal of Physics: Conference Series*, 1725(1), 012010. doi:10.1088/1742-6596/1725/1/012010

Rashwan, N. I., & El Dereny, M. (2012). The comparison between result of application Bayesian and maximum likelihood approaches on logistic regression model for prostate cancer data. *Applied Mathematical Scienses*, 6, 1143-1158.

Suleiman, M., Demirhan, H., Boyd, L., Girosi, F., & Aksakalli, V. (2019). Bayesian logistic regression approaches to predict incorrect DRG assignment. *Health care management science*, *22*(2), 364-375. doi: 10.1007/s10729-018-9444-8.

Spyroglou, I. I., Spöck, G., Chatzimichail, E. A., Rigas, A., & Paraskakis, E. (2018). A Bayesian logistic regression approach in asthma persistence prediction. *Epidemiology, Biostatistics and Public Health*, *15*(1). doi:10.2427/12777.

Tektaş, D., & Günay, S. (2008). Bayesian approach to parameter estimation in binary logit models. *Hacettepe Journal of Mathematics and Statistics*, 37, 167-176.

Zellner, A., & Rossi, P.E. (1984). Bayesian analysis of dichotomous quantal response models. *Journal of Econometrics*, 25, 365-393.

Yüzüncü Yıl Üniversitesi
Fen Bilimleri Enstitüsü Dergisi

http://dergipark.gov.tr/yyufbed

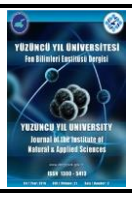

Research Article

Investigation of Some Physical Properties of CoAsS Crystal Under Pressure

Ferhat ARSLANBAŞ[1], Emel KİLİT DOĞAN*[1]

[1]Van Yüzüncü Yıl Üniversitesi, Fen Fakültesi, Fizik Bölümü, 65080, Van, Türkiye
Ferhat ARSLANBAŞ, ORCID No: 0000-0002-9835-9745, Emel KİLİT DOĞAN, ORCID No: 0000-0001-7609-7206
*Corresponding author e-mail: ekilit@yyu.edu.tr

Article Info

Received: 17.03.2020
Accepted: 24.08.2020
Published: August 2021
DOI: 10.53433/yyufbed.898639

Keywords
CoAsS,
Elastic properties,
Optical properties,
Thermodynamical properties

Abstract: Density functional theory (DFT) within the generalized gradient approximation (GGA) was used to inquire the structural, electronic, optical, elastic and thermodynamic properties of CoAsS crystal for the ground state (P=0 GPa) and for some pressure values such as 10, 20, 30, 40 and 50 GPa. CoAsS crystal has a semiconductor character with 1.06 eV indirect band gap. By increasing the pressure on CoAsS crystal band gap values were increasing as expected but by 40 GPa band gap value intented to decrease because of the structural deformation caused by the high pressure. The graphs of electronic band structure, density of states, and the all graphs for optic and thermodynamic properties were plotted with all pressure values and given in one figure to provide an easy comparison. Elastic properties were also given to show the effect of pressure on CoAsS crystal. It was noticed that cubic CoAsS mineral was fragile.

CoAsS Kristalinin Bazı Fiziksel Özelliklerinin Basınç Altında İncelenmesi

Makale Bilgileri

Geliş: 17.03.2020
Kabul: 24.08.2020
Yayınlanma: Ağustos 2021
DOI: 10.53433/yyufbed.898639

Anahtar Kelimeler
CoAsS,
Elastik özellikler,
Optik özellikler,
Termodinamik özellikler

Öz: CoAsS kristalinin temel durumdaki (P=0 GPa) ve 10, 20, 30 ve 40 GPa basınçları altındaki yapısal, elektronik, optik, elastik ve termodinamik özellikleri Yoğunluk Fonksiyoneli Teorisi ile Genelleştirilmiş Gradyent Yaklaşımı altında incelenmiştir. CoAsS kristali 1.06 eV luk doğrusal olmayan band aralığı ile yarıiletken bir karaktere sahiptir. CoAsS üzerindeki basınç artırıldığında kristal bant aralığı beklendiği gibi artmakta ancak yüksek basıncın neden olduğu yapısal deformasyon nedeniyle 40 GPa değerinden itibaren bant aralığı düşme eğilimindedir. Elektronik bant yapısının grafikleri, durum yoğunluğu, optik ve termodinamik özellikler için tüm grafikler, tüm basınç değerleri ile çizilip, kolay bir karşılaştırma sağlamak için tek bir figürde verilmiştir. Basıncın CoAsS kristali üzerindeki etkisini göstermek için elastik özellikler de verilmiştir. Kübik CoAsS mineralinin kırılgan olduğu bulunmuştur.

1. Introduction

Cobaltite (sulfarsenide of cobalt) is a mineral, composed of cobalt (Co), arsenic (As) and sulfur (S) with the chemical formula CoAsS. It is found in a variety of ore deposits especially in high temperature veins or in metamorphosed rocks. These minerals constitute with a major part of technologically important cobalt deposits especially in Morocco, Canada, US, and Russia (Ertseva, 2002). This mineral is strategically important because of containing cobalt element.

There are different types of cobaltites with different space groups, such as $Pca2_1$, $P2_13$ and $Pca2_1$ with different crystal structures as orthorhombic, cubic and monoclinic, respectively (Bayliss, 1982). CoAsS in general has a pyrite type structure (Mosselmans, 1995) such as NiAsS (gersdorffite), NiSbS (ullmannite), CoPS, and large number of others (Pielnhofer, 2015; Gao, 2017).

CoAsS has an forceful spin-orbit coupling and because of that it shows magnetocrystalline anisotropy energy (Liu, 2019). CoAsS is an isoelectronic compound (Pielnhofer, 2015) and exhibits ferromagnetism and piezoelectricity. Materials with both ferromagnetism and piezoelectricity are quite beneficial for magnetoelectric memory devices (Liu, 2019). At higher temperatures as 850 ^{0}C, arsenic and sulfur become completely disordered (Weihrich, 2004), because of its functional and adjustable properties, CoAsS is used in a large application fields such as photovoltaics, electrocatalysis and energy storage (Gao, 2017).

Ertseva and Tsymbulov (Ertseva, 2002) studied phase transformations with respect to thermal influences. Many cobaltite specimens from localities in North America, Australia, and Sweden were analyzed with experimental techniques by Bayliss (Bayliss, 1982) in order to investigate the structural properties. Mosselmans et al. (1995) presented metal K- and L3-, sulfur K- and arsenic K- and L3-edge X-ray absorption spectra of a series of metal disulfides, such as FeS_2, CoS_2, NiS_2, and CuS_2, and their isomorphs, FeAsS and CoAsS. Liu and Zhuang have studied the magnetic and phonon properties of single layer ferromagnetic and piezoelectric CoAsS crystal (Liu, 2019). Fleet and Burns (Fleet, 1990) have studied twin boundaries that are incoherent and coherent toward X-ray diffraction in cobaltite. Kaur and Bera (Kaura, 2017) theoretically investigated the effect of alloying on the thermal conductivity and the thermoelectric properties of cobaltite, CoAsS. Here, we studied on cubic CoAsS in order to understand the effect of pressure on structural, electronic, optical, elastic and thermodynamic properties. First, we investigated these properties for the ground state (P=0GPa). Then we examined the effect of pressure for the values of 10, 20, 30, 40 and 50 GPa theoretically on those physical properties, using the Density Functional Theory (DFT) within the Generalized Gradient Approximation (GGA) by ABINIT (Gonze, 2002) computer programme. The motivation of this study is to show the effect of the pressure on the electronic band structure, density of states, real and imaginary parts of dielectric constants, reflectivity, refractive index, extinction coefficients, absorption coefficients, energy-loss function for volume, effective number of valence electrons per unit cell, Helmholtz free energy, internal energy, entropy and constant-volume specific heat for cubic CoAsS compound. The objective of this paper was studying of the optical, elastic and thermodynamic properties of CoAsS for the ground state and the pressure effect on the physical properties for the first time.

2. Materials and Methods

In order to understand the physical properties of CoAsS in the ground state and under pressure we performed a first-principle calculations using ABINIT (Gonze, 2002) code under GGA. There are some types of CoAsS with different crystal structures, however, in this study we investigated the cubic structure with $P2_13$ space group (No:198) which has 12 atoms in its unit cell. To perform the calculations under the DFT, the Kohn–Sham (Kohn, 1965) equations were solved using the conjugate gradient minimization method (Payne, 1992). The exchange correlation energy was evaluated by the GGA within the Perdew–Burke–Enzerhof (PBE) (Perdew, 1992) parameterization. The self-consistent FHI (Fritz Haber Institute)-type (Fuch, 1999) norm-conserving pseudopotentials were used with the Troullier-Martins scheme (Troullier, 1991) for the GGA pseudo-potentials of Co, As and S elements. To perform the electronic wave functions, the plane waves were used as the basis set. Co ($3s^2\ 3p^6\ 4s^2\ 3d^7$), As ($4s^2\ 3d^{10}\ 4p^3$) and S ($3s^2\ 3p^4$) states were considered as the true valence states. We performed the optimization of the cut-off energy and the number of k-points and computed the cut-off energy as 30 Hartree and the number of k-points as 45 within the 8 x 8 x 8 Monkhorst-Pack mesh grid (MP) (Monkhorst, 1976) for cubic CoAsS compound.

3. Reults

3.1. Structural properties

Cobaltite, CoAsS, in cubic phase with space group of $P2_13$ (No: 198) was investigated in this research. First, the structural properties were examined in the ground state and under pressure values of P=0, 10, 20, 30, 40 and 50 GPa. The internal atomic coordinates for each pressure were relaxed. All physical properties of a material are directly related with the total energy. For the ground state (for P=0 GPa) the total energy of CoAsS was -172.4521 Hartree. At this total energy value, CoAsS was stable for the ground state, and its volume was 1152.65 $(Bohr)^3$ (=609 $(Å)^3$). The lattice parameters were calculated for all pressure values and the ground state (Table 1). For the ground state the lattice parameter was calculated as 10.4849 Bohr (=5.5482 Å) which is very close to the value in the literature, 5.584 Å (Jain, 2013) for the ground state. The lattice parameter values for the P=10, 20, 30, 40 and 50 GPa pressure values could not compared with the literature since there is no any theoretical or experimental data for those pressure values.

Table 1. The volume and lattice parameters of CoAsS with respect to the pressure values

Pressure (GPa)	Volume $(Bohr)^3$	Lattice Parameter (Bohr)
P=0 (Ground State)	1152.65	10.4849
P=10	1089.47	10.2897
P=20	1042.46	10.1395
P=30	1002.78	10.0092
P=40	970.06	9.8991
P=50	944.86	9.8127

As noticed from Table 1, with the increasing of the applied pressure, the volume and the lattice parameters were decreased as expected.

3.2. Electronic properties

To investigate the electronic properties of CoAsS compound, we computed and calculated the electronic band structure and the density of states graphs of cobaltite for ground state and for other all pressure values mentioned before. The electronic band structure graph is obtained for the $\Gamma - X - M - R - \Gamma - M$ high symmetry points and given in Figure 2, with the density of states graph attached (Figure 1(a)), and the detailed part of the electronic band graph between the 0 and 6.5 eV energy interval (Figure 1(b)). The density of states (DOS) values are given in arbitrary units. The Fermi level is adjusted to 0 eV. So the energy levels under the 0 eV (Fermi level) are valence energy levels and the energy levels above the 0 eV are conduction bands. Also from Figure 1 (a), core electron energy levels can be seen. The obtained result for the indirect band gap is 1.0583 eV for ground state, so cubic CoAsS has a semiconducting structure. The band gap values found in the literature are 0.75 eV (Kaura, 2017) and 0.849 eV (Jain, 2013). Figure 1 (a) shows that the main contribution for the density of states comes from the valence bands. After these, we calculated the electronic band structures for different pressure values such as P=10, 20, 30, 40 and 50 GPa. We gave the highest valence and the lowest conduction levels of all pressure values in order to compare the band gaps of CoAsS in all pressure values (Figure 2). The band gap values of the applied pressure values were given in Table 2. In Table 2, it was noticed that the band gap values were increasing with the increasing of the applied pressure values such as 10, 20 and 30 GPa. It is known that when pressure increases, value of band gap also increases (Erdinc, 2015), or when pressure increases the band gap decreases (Okoye, 2004), in other words there is a linear relationship between pressure and band gap. For CoAsS from 0 to 30 GPa, the band gap was increasing with the increasing of the pressure while the band gap was decreasing as the pressure was increasing for 40 and 50 GPa. We noticed that around 40 GPa pressure value the structural deformation occured for cubic CoAsS because of high pressure effect. CoAsS deformed around 40 GPa. Because of that for 40 and 50 GPa pressure values some physical properties such as elastic properties were corrupted. In the following parts we discussed this circumstance in the elastical properties point of view. Also the elastic properties were deformed with the 40 and 50 GPa values.

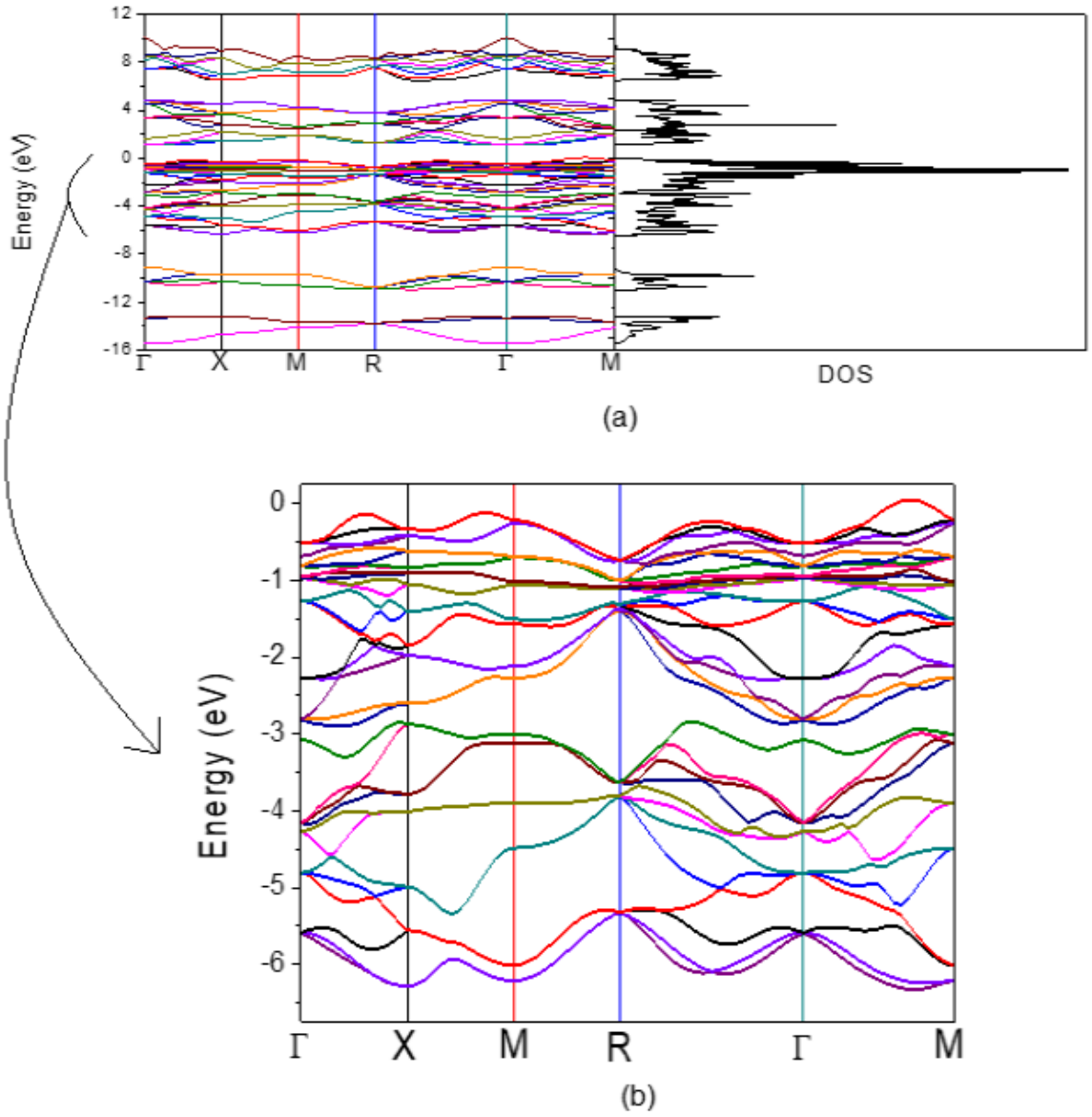

Figure 1. (a) The electronic band structure attached with the total density of states, (b) the detailed part of the valence bands with the 0-6.5 eV energy interval.

Table 2. The band gap values of CoAsS with respect to the pressure values

Pressure (GPa)	Energy Band Gaps (eV)
P=0	1.0583
P=10	1.1637
P=20	1.2084
P=30	1.2367
P=40	1.2317
P=50	1.1577

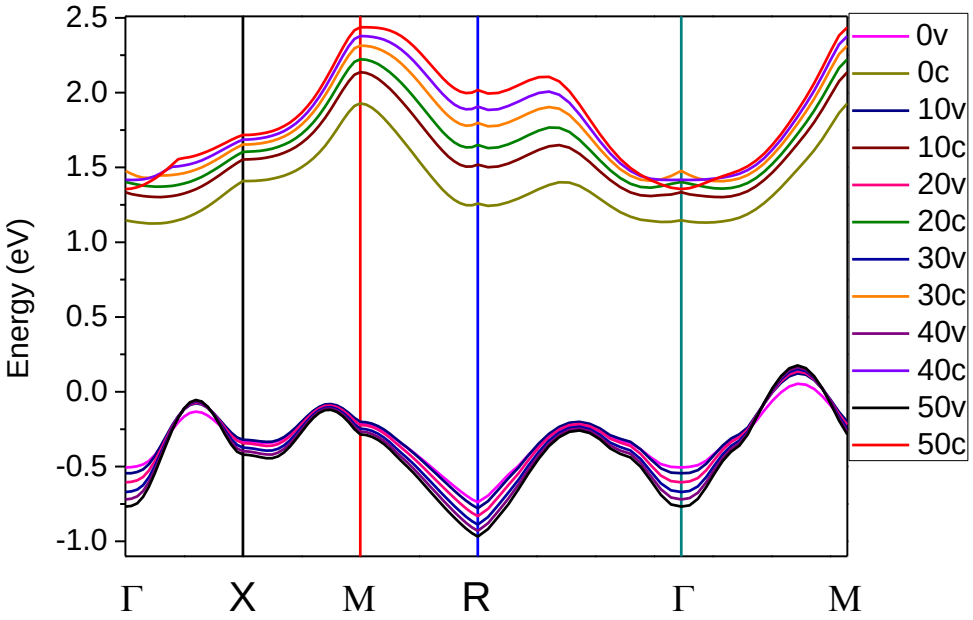

Figure 2. The highest valence and the lowest conduction bands of CoAsS with respect to all applied pressure values.

Table 3. Energy dispersion of the highest valence band and the lowest conduction band of CoAsS at various pressures. Energy values are given in eV units

0 GPa	10 GPa	20 GPa	30 GPa	40 GPa	50 GPa	0 GPa
$E_{\Gamma-\Gamma}$	1.6452	1.8683	2.0000	2.1258	2.147	2.1217
E_{X-X}	1.7334	1.8673	1.9476	2.0295	2.0822	2.1338
E_{M-M}	2.1267	2.3417	2.4461	2.5576	2.6468	2.7178
E_{R-R}	1.9899	2.293	2.4694	2.6651	2.8354	2.9854
$E_{\Gamma-X}$	1.4739	1.6443	1.7395	1.8338	1.8216	1.779
$E_{\Gamma-M}$	1.3563	1.5277	1.6209	1.7091	1.6918	1.6361
$E_{\Gamma-R}$	1.8764	2.1045	2.2281	2.3468	2.3508	2.3295
E_{X-M}	1.6158	1.7507	1.829	1.9048	1.9524	1.9909
E_{X-R}	2.1359	2.3275	2.3262	2.5425	2.6114	2.6843
E_{M-R}	2.6468	2.9185	3.0533	3.1953	3.3058	3.4112

In Table 3, the effect of high pressure (40 and 50 GPa) can be seen.

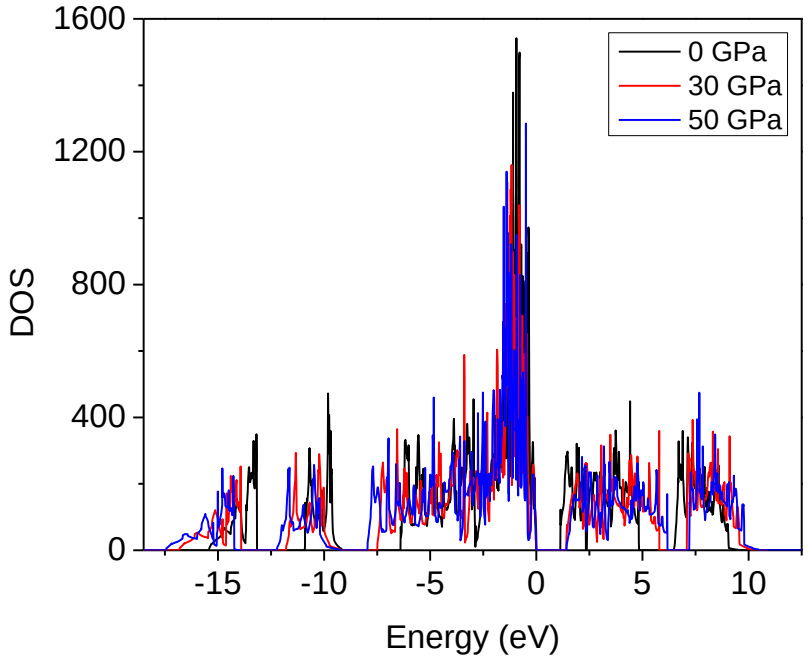

Figure 3. Density of states according to various pressure values.

The density of states graphs for different pressures were given in one plot as seen in Figure 3. This investigation was also done for all pressure values mentioned before, but in the graph only the P=0, 30 and 50 GPa values were given in order to avoid confusion in the figure. As the pressure increased, the frequency values of the valence bands decreased and the frequency of the conduction bands increased, so that the band gap increased up to 40GPa, and decreased for the 40 and 50 GPa, because of the structural and elastical deformation.

The effect of the pressure on the electronic band structure and density of states are done for the first time in the literature with this study.

3.3. Optical properties

To investigate the optical properties, the complex dielectric function should be calculated. The complex dielectric function has the real (ε_1) and the imaginary (ε_2) parts. After calculating the imaginary part of the complex dielectric function, the real dielectric part can be calculated from imaginary part by using the Kramers-Kronig relations. The real part is mostly related with the physical properties of the material and the imaginary part is mostly related with the energy loss of photons in a material, electron transition between electronic bands and optical response of the material such as absorption, reflection etc. with respect to the phonon energies. The complex dielectric function has three different components along the 100, 010 and 001 crystal axes directions. Since cubic materials are optically isotropic, means that the optical responses of polarized light is same for these three directions, only one independent component is sufficient to investigate.

The real and imaginary parts of the dielectric function for P=0, 10, 20, 30, 40 and 50GPa pressure values are given in Figure 4 (a) and 4 (b), respectively.

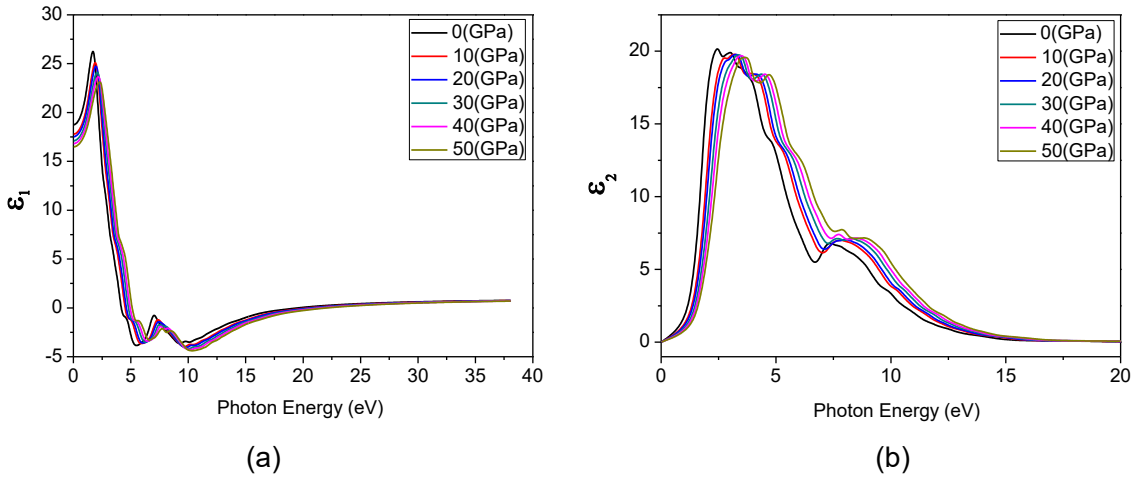

Figure 4. The (a) real and (b) imaginary parts of complex dielectric function under P=0, 10, 20, 30, 40 and 50 GPa pressure values.

The calculated static dielectric constants (ε_0) of cubic CoAsS were 18.75, 17.79, 17.52, 17.11, 16.82 and 16.49 for P=0, 10, 20, 30, 40 and 50GPa, respectively. The negative values of the real dielectric constants were between 4.12-19.83 eV of phonon energies (for P = 0 GPa), that in these intervals the incident electromagnetic waves are totally reflected. This interval was getting enlarged as the pressure increases. Beyond these intervals there was no transition occurs between the states. At the boundary points of these intervals, the zero values of ε_1 corresponds to the plasmon excitations. The parts in which ε_1 increases with the phonon energy is called normal dispersion state, decreasing with the phonon energy is called abnormal dispersion state. From ε_2, for the ground state, between the 0 and 1.06 eV phonon energy interval, there was no absorption but small reflectivity occured because this region showed high transparency. From 1.06 to 2.39 eV there was strong absoption and appreciable reflection. For higher values than 1.06 eV (equal to band gap value, obtained by the electronic band structure graph) the transitions from valence to conduction bands were seen. From 2.39 to 7.39 eV there was high reflectivity. For higher pressure values those energy intervals can be seen from Figure 4 (b).

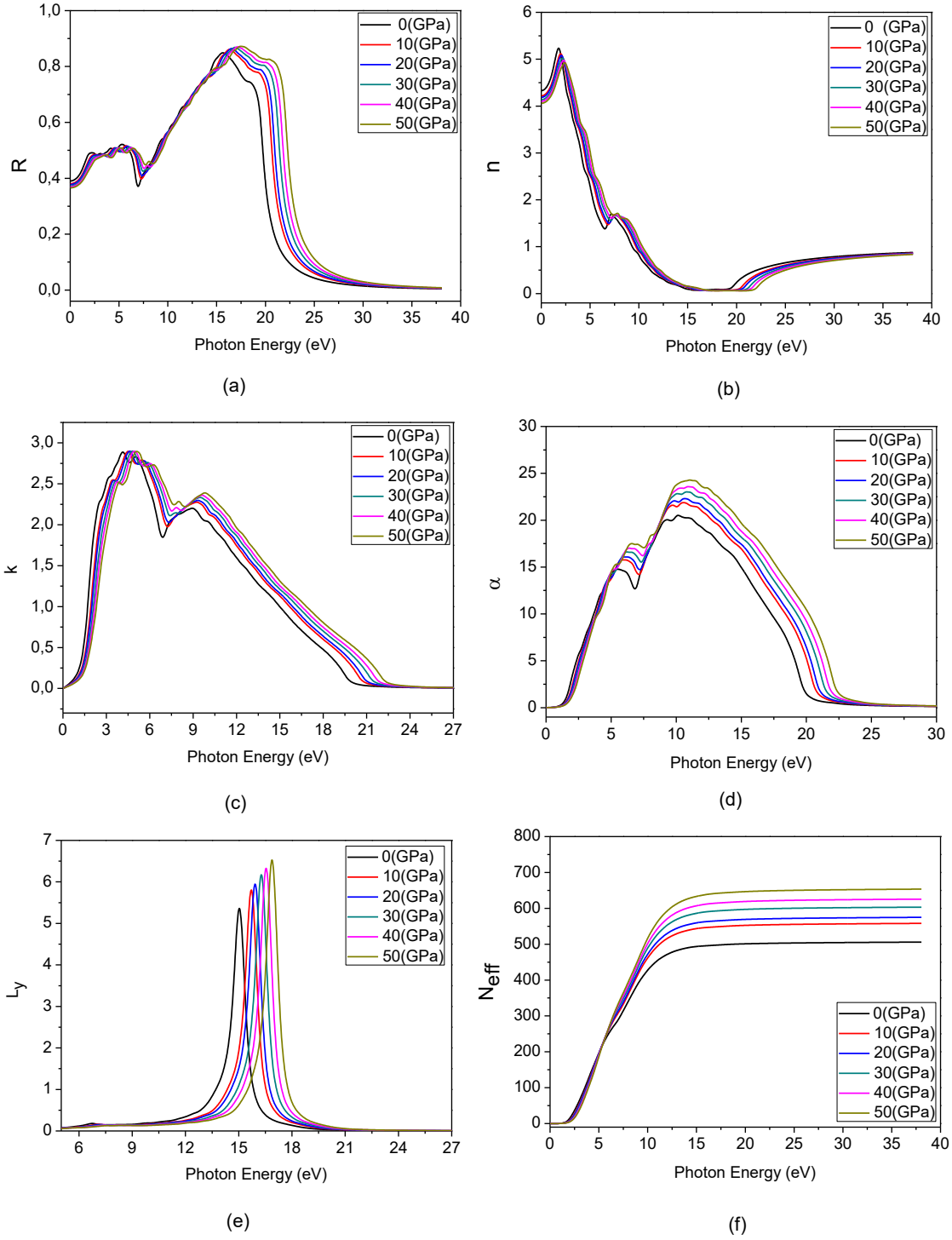

Figure 5. (a) Reflectivity (R), (b) refractive index, (c) extinction coefficient (k), (d) absorption coefficient (α), (e) energy loss function for volume (L_V) , (f) effective number of valence electrons per unit cell (N_{eff}).

Some fundamental optical constants were given in Figure 5. The characteristic of the reflectivity can be seen in Figure 5 (a). The static refractive index of CoAsS was 4.33, 4.22, 4.19, 4.14, 4.10 and 4.06 for P=0, 10, 20, 30, 40 and 50 GPa, respectively. The local minimum part of the extinction coefficient corresponds to the phonon energy interval of the negative parts of the real component of dielectric constant. Loss function refers to the energy loss of a fast electron crossing

over the crystal. The peak of the energy loss function for volume (L_V) is related with the plasma oscillations with ω_p plasma frequency, which also corresponds to the negative values of the ε_1. N_{eff} specifies the contribution which was done to optical functions during the transition between the electronic bands and reaches to the saturation level (504.07) at around 15 eV. After this level there were no any transitions between the electronic bands.

3.4. Elastic properties

In order to analyze the elastic properties such as bulk modulus, shear modulus, Young modulus etc, first of all the elastic constants have to be calculated. Elastic constants are the components of elastic matrix. Elastic matrix has 36 components. Actually, elastic constants are rank four tensors with 81 components (C_{klmn}) but by using a matris notation four indices can be decreased to 2 indices (C_{ij}) and 81 components decrease to 36 components by the help of the symmetry of crystals. Additionally, cubic structures has extra symmetries, therefore, in the cubic structures elastic matrix has just three components, namely, C_{11}, C_{12}, C_{44}.

$$\begin{pmatrix} C_{11} & C_{12} & C_{13} & C_{14} & C_{15} & C_{16} \\ C_{21} & C_{22} & C_{23} & C_{24} & C_{25} & C_{26} \\ C_{31} & C_{32} & C_{33} & C_{34} & C_{35} & C_{36} \\ C_{41} & C_{42} & C_{43} & C_{44} & C_{45} & C_{46} \\ C_{51} & C_{52} & C_{53} & C_{54} & C_{55} & C_{56} \\ C_{61} & C_{62} & C_{63} & C_{64} & C_{65} & C_{66} \end{pmatrix} \rightarrow \begin{pmatrix} C_{11} & C_{12} & C_{12} & 0 & 0 & 0 \\ . & C_{11} & C_{12} & 0 & 0 & 0 \\ . & . & C_{11} & 0 & 0 & 0 \\ 0 & 0 & 0 & C_{44} & 0 & 0 \\ 0 & 0 & 0 & 0 & C_{44} & 0 \\ 0 & 0 & 0 & 0 & 0 & C_{44} \end{pmatrix}$$

The values of these elastic components are given in Table 4 with respect to the applied pressure values.

Table 4. The values of C_{11}, C_{12} and C_{44} according to the pressure values

Pressure (GPa)	C_{11} (GPa)	C_{12} (GPa)	C_{44} (GPa)
0	299.32	41.20	103.29
10	401.49	52.83	122.81
20	470.58	67.21	141.74
30	557.05	78.89	156.33
40	603.11	90.94	169.68
50	595.71	93.23	172.80

If the material is mechanically stable it has to obey to Born Stability Criterias. These criterias changes according to the crystal structure of the material (Mouhat, 2014). For cubic structure this criteria is as follows;

$$C_{11} - C_{12} > 0\,;\, C_{11} + 2C_{12} > 0\,;\, C_{44} > 0 \quad (1)$$

As seen from Table 4, our calculated values for all pressure values satisfied the criteria which confirmed that cubic CoAsS was mechanically stable.

Afterwards, we computed the values of the Bulk modulus (B) and Shear Modulus (G) with three different approximations that are namely Voight, Reuss and Hill. Then we computed Yound module (E), Poisson's coefficients (ν) and Zener anisotropy factor (A) for all pressure values (Table 5). As seen from Table 5, the bulk modulus values with respect to these approximations were calculated as equal to each other.

Table 5. Values of some elastic features with respect to pressure values.

Pressure (GPa)	B_R (=B_V) (=B_{VRH}) (GPa)	G_V (GPa)	G_R (GPa)	G_{VRH} (GPa)	E (GPa)	ν (-)	K (-)	A
0	127.24	113.59	112.25	112.92	261.43	0.15	1.12	0.800
10	169.04	143.41	139.27	141.34	331.60	0.17	1.19	0.705
20	201.66	165.71	160.86	163.29	385.75	0.18	1.23	0.703
30	238.28	189.42	181.45	185.44	441.73	0.19	1.28	0.654
40	261.66	204.24	196.15	200.20	478.55	0.20	1.31	0.663
50	260.72	204.17	197.45	200.81	479.37	0.19	1.30	0.688

The ratio of bulk modulus and shear modulus (K) gives the fragility of that material. The smaller values than the critical value of K e.i. 1.75, are fragile materials. We found this ratio as 1.12 for the ground state and 1.30 for the P=50 GPa, it showed that cubic CoAsS was a fragile material. Also the critic value of Poisson ratio is $0.\overline{3}$. The smaller values indicates that materials have fragile property. Since our calculated values of Poisson ratio's for all pressure values were smaller than $0.\overline{3}$, so this also provided that our material was fragile. The anisotropy factor (A) points that the elastic anisotropy of the materials. Our calculated values were between 0.800 and 0.688 that demonstrates that cubic CoAsS has elastic anisotropy.

3.5. Thermodynamic properties

To investigate the thermodynamic features of cubic CoAsS mineral, the Helmholtz free energy ΔF, the internal energy ΔE, the constant-volume specific heat C_V and the entropy S were calculated as a function of temperature and given in Figure 6.

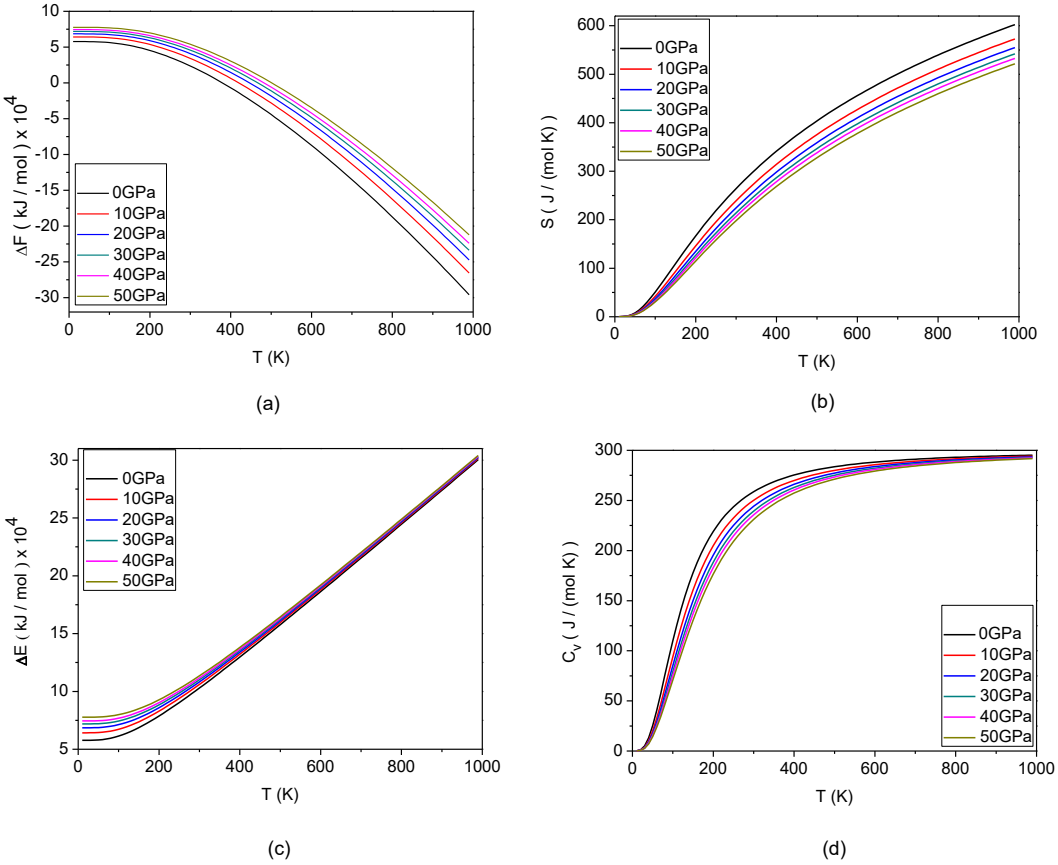

Figure 6. Some thermodynamic properties of cubic CoAsS such as (a) Helmholtz Free energy ΔF, (b) Entropy S, (c) internal energy ΔE and (d) constant- volume specific heat C_V.

As seen from Figure 6, the free and the internal energies were different from zero at zero temperature, so it was clear that at zero point oscillations occured. The value of free energy was 5.789 $x10^4$ k J /mol and the value of internal energy was $5.796x10^4$ k J /mol at zero temperature for the ground state. These values were very close to each other as expected. At the same temperature point the values of both energies were increasing as ingreasing the pressure (Figures 6 (a) and (c)). However as the pressure were increasing the entropy and the constant-volume specific heat decreased. Specific heat approached a limit value 295.11 J/mol K at 914.96 K.

4. Conclusions

The approach of this study was to figure out some physical properties of cubic CoAsS mineral such as structural, electronic, optical, elastic and thermodynamic properties in the ground state and the influence of pressure on those properties. The lattice parameters for all pressure values were calculated and one for the ground state was compared with the literature, which was given a good agreement. Afterwards the electronic band structure and the density of states were computed and plotted, which showed that this material was a semiconductor with an indirect band gap. We found out the optical properties of cubic CoAsS under pressure. It was found that this material was elastically fragile and structurally deformed at around 40GPa and higher pressure values as also noticed in the electronic properties. Last of all the Helmholts free energy, internal energy, entropy and constant volume specific heat were investigated for the ground state and under pressures. These calculations were performed for the first time that is why we could not compared our results with the literature. We believe that this study will be a guide for new further studies on cubic CoAsS mineral.

References

Bayliss, P. (1982). A further crystal structure refinement of cobaltite. *American Mineralogist,* 67, 1048-1057.

Erdinc, B., Secuk, M. N., Aycibin, M., Gulebagan, S. E., Dogan, E. K. & Akkus, H. (2015). Ab-initio calculations of physical properties of alkali chloride XCl (X = K, Rb and Li) under pressure. *Computational Condensed Matter,* 4, 6-12. doi:10.1016/j.cocom.2015.05.001

Ertseva, L. N & Tsymbulov, L. B. (2002). On transformations of iron, nickel, and cobalt arsenides and sulfoarsenides under thermal treatment in various media. *Russian Journal of Applied Chemistry*, 75 (10), 1547-1556.

Fleet, M. E. & Burns, P. C. (1990). Structure and twinning of cobaltite. *Canadian Minerologist,* 28, 719-723.

Fuch, M. & Scheffler, M. (1999). Ab initio pseudopotentials for electronic structure calculations of poly-atomic systems using density-functional theory. *Computer Physics Communications,* 119, 67-98. doi:10.1016/S0010-4655(98)00201-X

Gao, M. R., Zheng, Y. R., Jiang, J. & Yu, S. H. (2017). Pyrite-type nanomaterials for advanced electrocatalysis. *Accounts of Chemical Research,* 50, 2194−2204. doi:10.1021/acs.accounts.7b00187

Gonze, X., Beuken, J. M., Caracas, R., Detraux, F., Fuchs, M., Rignanese, G. M., Sindie, L., Verstrate, M., Zerah, G., Jollet, F., Torrent, M., Roy, A., Mikami, M., Ghosez, P., Raty, J. Y. & Allan, D. C. (2002). First-principles computation of material properties: the ABINIT software Project. *Computational Materials Science,* 25, 478-492. doi:10.1016/s0927-0256(02)00325-7

Jain A., Ong S. P., Hautier, G., Chen, W., Richards, W. D., Dacek, S., Cholia, S., Gunter, D., Skinner, D., Ceder, G. & Persson, K. A. (2013). Commentary: The materials project: A materials genome approach to accelerating materials innovation. *APL Materials,* 1(1), 011002. doi:10.1063/1.4812323

Kaura, P. & Bera, C. (2017). Effect of alloying on thermal conductivity and thermoelectric properties of CoAsS and CoSbS. *Physical Chemistry Chemical Physics*,19, 24928-24933.

Kohn, W. & Sham, L. J. (1965). Self-consistent equations including exchange and correlation effects. *Physical Review,* 140, A1133. doi:10.1103/PhysRev.140.A1133

Liu, L. & Zhuang, H. L. (2019). Single-layer ferromagnetic and piezoelectric CoAsS with pentagonal structure. *APL Materials,* 7, 011101. doi:10.1063/1.5079867

Monkhorst, J. H. & Pack, J. D. (1976). Special points for Brillouin-zone integrations. *Physical Review B,* 13, 5188-5192. doi:10.1103/PhysRevB.13.5188.

Mosselmans, J. F. W., Pattrick, R. A. D., van der Laan, G., Charnock, J. M., Vaughan, D. J., Henderson, C. M. B. & Garner, C. D. (1995). X-ray absorption near-edge spectra of transition metal disulfides FeS2 (pyrite and marcasite) COS2, NiS2 and CuS2, and their isomorphs FeAsS and CoAsS. *Physics and Chemistry of Minerals,* 22, 311-317. doi:10.1007/bf00202771

Mouhat, F. & Coudert, F. X. (2014). Necessary and sufficient elastic stability conditions in various crystal systems. *Physical Review B,* 90, 224104. doi:10.1103/PhysRevB.90.224104

Okoye, C. M. I. (2004). Investigation of the pressure dependence of band gaps for silver halides within a first-principles method. *Solid State Communications*, 129, 69-73. doi:10.1016/j.ssc.2003.09.014

Payne, M. C., Teter, M. P., Allan, D. C., Arias, T. A. & Joannopoulos, J. D. (1992). Iterative minimization techniques for *ab initio* total-energy calculations: molecular dynamics and conjugate gradients. *Review of Modern Physics,* 64, 1045-1097. doi:10.1103/RevModPhys.64.1045

Perdew, J. P., Chevary, J. A., Vosko, S. H., Jackson, K. A., Pederson, M. R., Singh, D. J., & Fiolhais, C. (1992). Atoms, molecules, solids, and surfaces: Applications of the generalized gradient approximation for exchange and correlation. *Physical Review B,* 46, 6671-6687. doi:10.1103/PhysRevB.46.6671

Pielnhofer, F., Schöneich, M., Lorenz, T., Yan, W., Nilges, T., Weihrich, R. & Schmidt, P. (2015). A rational approach to IrPTe – DFT and CalPhaD studies on phase stability, formation, and structure of IrPTe. *Zeitschrift für anorganische Chemie*, 641 (6), 1099–1105. doi:10.1002/zaac.201500149

Troullier, N. & Martins, J. L. (1991). Efficient pseudopotentials for plane-wave calculations. *Physical Review B,* 43, 1993-2006. doi:10.1103/PhysRevB.43.1993

Weihrich, R., Kurowski, D., Stückl, A. C., Matar, S. F. Rau, F. & Bernerta, T. (2004). On the ordering in new low gapsemiconductors: PtSnS, PtSnSe, PtSnTe. Experimental and DFT studies. *Journal of Solid State Chemistry***,** 177, 2591–2599. doi:10.1016/j.jssc.2004.03.031

ÜNİVERSİTESİ

1982

Fen Bilimleri Enstitüsü Dergisi / *Journal of the Institute of Natural & Applied Sciences*